IN VITRO TISSUE ENGINEERING OF LIVER AND PRIMARY LYMPHOID TISSUES WITH INVERTED COLLOIDAL CRYSTAL SCAFFOLDS FOR DRUG TESTING APPLICATION

by

Jung Woo Lee

A dissertation submitted in partial fulfillment
of the requirements for the degree of
Doctor of Philosophy
(Biomedical Engineering)
in The University of Michigan
2009

Doctoral committee:

Professor Nicholas A. Kotov, Chair
Professor Scott J. Hollister
Professor Peter X. Ma
Associate Professor Shuichi Takayama


IN VITRO PERFECTION

To my parents, Ju-ho Lee and Yong-soon Kim
and my wife Jiyoung Jung
for their endless love and support

ACKNOLWEDGEMENTS

There is a Korean saying that every man has three big chances in his life whether he recognizes it or not. To me, having an opportunity to do Ph.D here was certainly one of my three chances. I would like to appreciate many people, who made me realized.

First and foremost, I would like to thank my advisor, Prof. Nicholas Kotov for his continuous supports throughout my time in the University of Michigan. He is a great mentor having profound capacity in science and engineering. His deep thoughts, hardworking, and enthusiasm are an endless inspiration to me. I admire his optimistic and jovial mind that always leads to discover new and unexpected outcomes. He is my role model and I have tried to resemble him. I also would like to thank my committee, Prof. Peter Ma, Scott Hollister and Shuichi Takayama for their continuous guidance and support. In addition I express my sincere thanks to Prof. Jinsang Kim for his constant trust and encouragement.

Zhiyong, Jaebeom, Paul, Bongsup, Sachin and Vladmir have been irreplaceable not only as my friends but also as my advisors in most matters. I thank to Meghan. As a team, we won many entrepreneurship challenges. It was unique experience and great fun. I have to thank Edward, George, Daniel and Chris for their help in my dissertation research. I cannot mention here all the vibrant discussions and willing help received from other group members. But thank you all.

I thank many Korean friends in Ann Arbor. I was lucky to have three classmates, Chanho, Yoonjung and Yoonseok, as well as many other BME friends. I also express gratitude to Kyungho, Dongwoo, Yungsoek, and Jihoon who spent most of their time with me in the G.G. Brown laboratories.

Lastly I would like to thank my parents, my wife and my brother Youngjun for their endless support and love.

TABLE OF CONTENTS

LIST OF FIGURES

LIST OF TABLES

LIST OF ABBREBATIONS

ICC	Inverted colloidal crystal
AFM	Atomic force microscopy
BD	Brownian dynamics
CFDA-SE	Carboxyfluorescein diacetate succinimidyl ester
CTAB	Cetyltrumethylammonium bromide
CMRA	Chloromethyl derivatives fluorescent dye
CC	Colloidal crystal
CYP450	Cytochrome P450
DL-1	Delta-like 1
ELISA	Enzyme-linked immunosorbent assay
EROD	Ethoxyresorufin-O-deethlylase
FTOC	Fetal thymus organ culture
FITC	Fluorescein isothiocyanate
HSC	Hematopoietic stem cell
H&E	Hematoxylin and eosin
HCA	High content analysis
HTS	High throughput-screening
HF	Hydrogen fluoride
IND	Investigational of new drug
LDH	Lactate dehydrogenase
LBL	Layer-by-layer
LPS	Lipopolysaccharide
MACS	Magnetic activated cell sorting kits
MSC	Mesenchymal stem cell
MC	Monte carlo
NP	Nanoparticle
NDA	New drug application
PDDA	Poly diallyldimethylammonium –chloride
PLGA	Poly(lactic-co-glycolic acid)
PCL	Poly(caprolactone)
SEM	Scanning electron microscope
SFF	Solid free-form
TCR	T-cell receptor
THF	Tetrahydrofuran
ROI	Region of interest
µ-CT	Micro-computed tomography

ABSTRACT

Effective early stage drug toxicity testing is imperative to minimize failures in the late clinical stages of the drug development process. Two-dimensional (2D) cell cultures have been dominantly used in the preclinical phase drug screening; however, it is becoming apparent that they cannot adequately estimate actual toxic effects of drug molecules due to the limited capability in restoring original cellular behaviors in three-dimensional (3D) tissues. As a potential solution to improve the predictive power of *in vitro* screening procedures, this dissertation explored a new opportunity of *in vitro* tissue engineering as a part of the drug development process.

Besides the biological significance in functional tissue formation, here scaffolds should be transparent and support standardized tissue growth. Inverted colloidal crystal (ICC) hydrogel scaffolds having standardized 3D structure and materials as well as retaining a high analytical capability were developed for this purpose. Uniform size spherical pore arrays prepared with cell repulsive polyacrylamide promoted homogenous HepG2 liver tissue spheroid formation, while the transparent hydrogel matrix allowed convenient characterization of cellular processes. The standardized spheroid culture model was successfully applied to the *in vitro* toxicity testing of CdTe and Au nanoparticles. Significantly reduced toxic effects were observed compared to the conventional 2D culture attributed by tissue-like morphology and cell phenotypic change in the spheroid culture.

In addition, ICC scaffolds combined with a layer-by-layer (LBL) surface modification technique served as a platform for engineering primary lymphoid tissue, i.e. bone marrow and thymus. Under dynamic culture condition, floating hematopoietic stem cells (HSCs) could travel deep into the scaffold via interconnecting channels, while they were temporarily entrapped due to limited channel size and number. As a result, HSCs extensively interacted with stromal cells growing along the LBL coated pore surface. Such intimate cell-cell and cell-matrix interaction is the key process in HSCs survival and differentiation that was substantiated by *ex vivo* expansion and B-/T-cell differentiation of HSCs.

Overall this thesis introduces a promising application of *in vitro* tissue engineering as a practical and valuable early stage toxicity testing tool. ICC scaffolds exhibited unique advantage in preparation of spheroid culture model and lymphoid tissue engineering. Standardized *in vitro* tissue models established in ICC scaffolds substantiate the capability to extend current cellular level cytotoxicity to the tissue level.

CHAPTER I

INTRODUCTION

1.1. Engineered tissue based *in vitro* drug testing

The drug development is a prolonged, expensive and complicate process that involves multiple-stage screening: (i) Identification and isolation of promising target compounds, (ii) Preclinical stage toxicity and efficacy testing of drug candidate molecules based on in vitro cellular assays and animal models, (iii) Clinical trials in human subjects, (iv) FDA approval and marketing. Average time and cost for launching a single drug is usually 10-12 years and $800 million, respectively.[1] (Figure 1.1A)

To improve such a long and expensive development process, the pharmaceutical industry has prodigiously invested in the development of novel technologies such as high throughput-screening (HTS)[2], high content analysis (HCA)[3], systems biology[4] etc. However, the low productivity issue remains same. For instance, the pharma industry heavily invested in HTS technology which is expected to bring 20-fold improvements in throughput, but it has yielded few products[5]. Figure 1.1B also shows that over the last several years global R&D expenditure increased almost 4 times, but total number of Investigational New Drug (IND) application and their acceptance ratio did not change.[6]

Vice versa R&D productivity has actually decreased which in turn sharply increases the average costs for a new drug development[7].

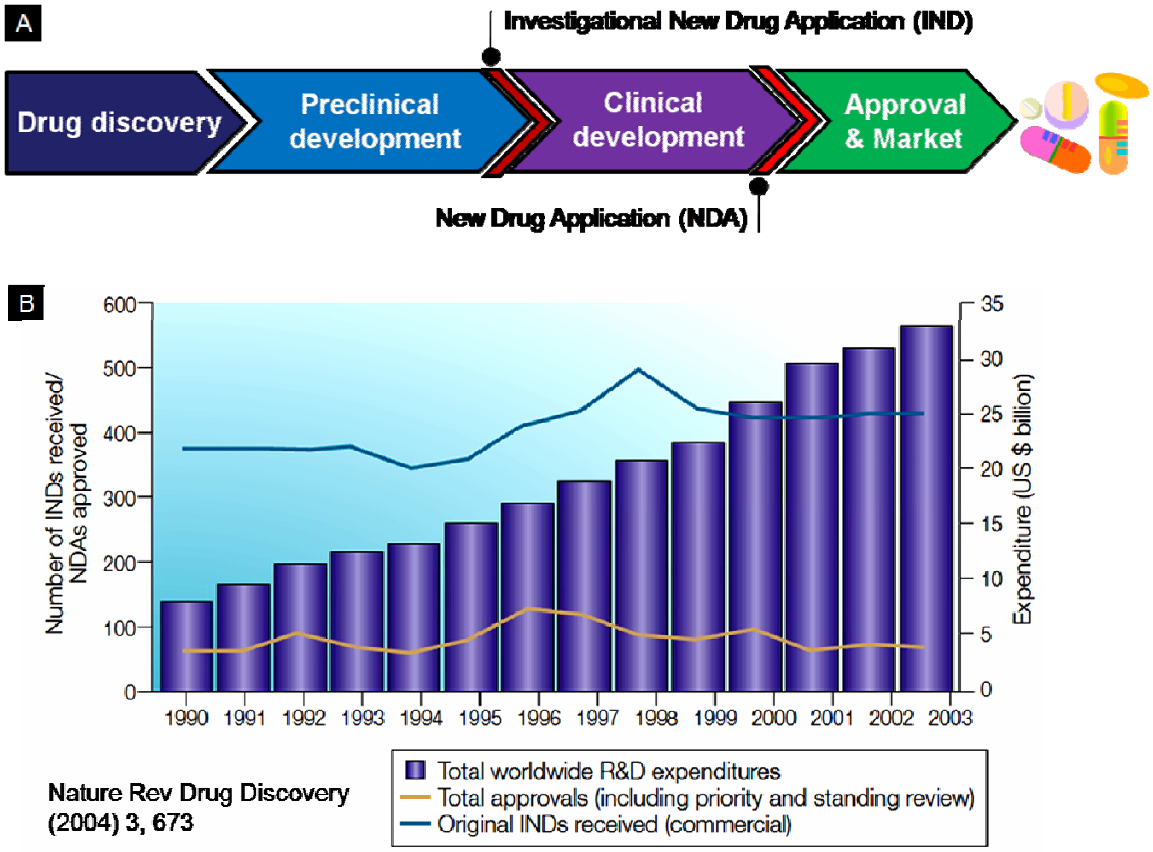

Figure 1.1 Current drug development process and low productivity issue. (A) Typical drug development process **(B)** Increased gap between R&D expenditure and IND application over the last few years[6].

One obvious reason of the low efficiency is the lack of effective early stage drug testing tools that are indicative of drug's interactions in a human body. Currently pharmaceutical industry exclusively relies on *in vitro* cell-based assays and animal studies in the preclinical stage drug testing. However, they are far limited to predict a drug's behavior and toxicity in the body. For example, although animal models have made a significant contribution to drug-target validation, essentially they are different species from human. Therefore, they often have markedly different pharmacokinetics.

The result of this is that time and money are invested in many potential drugs that eventually fail late in the testing process. In fact it is quite common that drug candidates can fail as late as clinical trials, after spending huge amount of time and money.[8]

In addition, *in vitro* cell-based assays have been performed mostly on 2D culture substrates such as micro-well plates, tissue culture flasks, and Petri dishes because of the convenience, and high cell viability of 2D culture. These conventional 2D cell culture systems notably improved the understanding of basic cell biology, but disadvantages lie in the using a 2D substrate. In the body, nearly all tissue cells reside in an extracellular matrix (ECM) consisting of a complex 3D fibrous meshwork with a wide distribution of fibers and gaps that provide complex biochemical and biophysical signals.[9] Additionally, each type of cells is embedded in a considerably different 3D microenvironment. For example, osteoblasts are located on the surface of bone in a sheet-like arrangement of cuboidal cells, hepatocytes are closely packed together in the liver in hexagonal shaped lobules, and lymphocytes are individually suspended in circulating blood or lymphatic vessels.[10] (Figure 1.3A, D & G) The differential niches of stem cells are inherently 3D, and their biochemistry and topology strongly affect the differentiation process.[11] Two-dimensional substrates are considerably limited in emulating those complex 3D microenvironments due to not only the lack of structural architecture but also finite material selections. Furthermore, the adaptation of cells to a 2D rigid substrate requires a dramatic adjustment by the surviving cells because of the lack of the unique ECM environment of each cell type. These drawbacks can alter cell metabolism and reduce functionality.[12-14] For that reason, 2D culture substrates not only fall short of reproducing the complex and dynamic environments of the body, but

also are likely to misrepresent findings by forcing cells to adjust to an artificial flat and rigid surface.

The ideal preclinical drug testing tool would be a 3D human cellular assay that allow the drug to be tested on human cells organized in a tissue where cells can interact as they would in the body. Recent advances in tissue engineering and stem cell research suggest potential to realize this idea. Although conventional tissue engineering aims to create functional human tissues for the clinical implantation, faithfully prepared human tissues also can be directly used for *in vitro* drug testing. Small pieces of engineered human tissues having intermediate stage physiological or pathphysiological complexity can significantly improve the predictive power of preclinical stage drug screening as bridging *in vitro* 2D cell culture and *in vivo* 3D human tissue. (Figure 1.2) Accompanied with significant progress in *ex vivo* manipulation of human stem cells, e.g. expansion and directed differentiation, this approach is becoming more feasible.[15, 16]

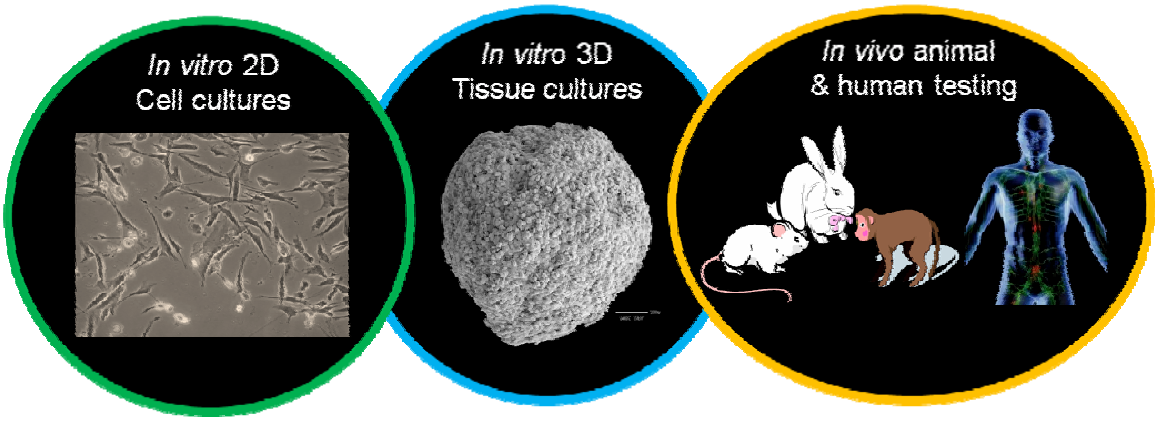

Figure 1.2 Engineered 3D human tissue based drug testing can fill the gap between *in vitro* 2D cell culture and *in vivo* animal & human testing.

1.2. Three-dimensional cell culture matrices

3D cell culture matrices have been introduced to overcome 2D culture limitations. Basically they are porous substrates supporting cell growth, organization, and differentiation on or within their structure. There is much more architectural and material diversity among 3D matrices than among 2D substrates. In part, such a variety of biomatrices is due to the large range of tissues and the need to produce cellular supports with different physical appearance, porosity, permeability, mechanical characteristics, and nano-scale surface morphology. (Figure 1.3) A variety of fabrication processes and biomaterials have been developed or adapted to meet this array of properties. The chosen fabrication process specifically affects the resulting matrix architecture. For example, electro-spinning[17] and particulate-leaching[18] methods create fibrous-mesh and sponge like structures, respectively. Solid free-form (SFF) fabrication techniques[19] can manufacture matrices with specific architectures and properties. In addition to fabrication processes, biomaterials have expanded the diversity of 3D cell culture matrices.[20, 21] The selection of biomaterial is determined by the selected fabrication technique and by the particular application of the 3D matrix. For instance, only a few biodegradable polymers are available for the purpose of making implantable 3D matrices.[22] In addition, engineering materials and fabrication processes can endow 3D cell culture matrices with complex functionalities, such as releasing growth factors that induce cellular differentiation.[23-25] New material-processing technologies are being investigated actively to meet multiple requirements in various applications.

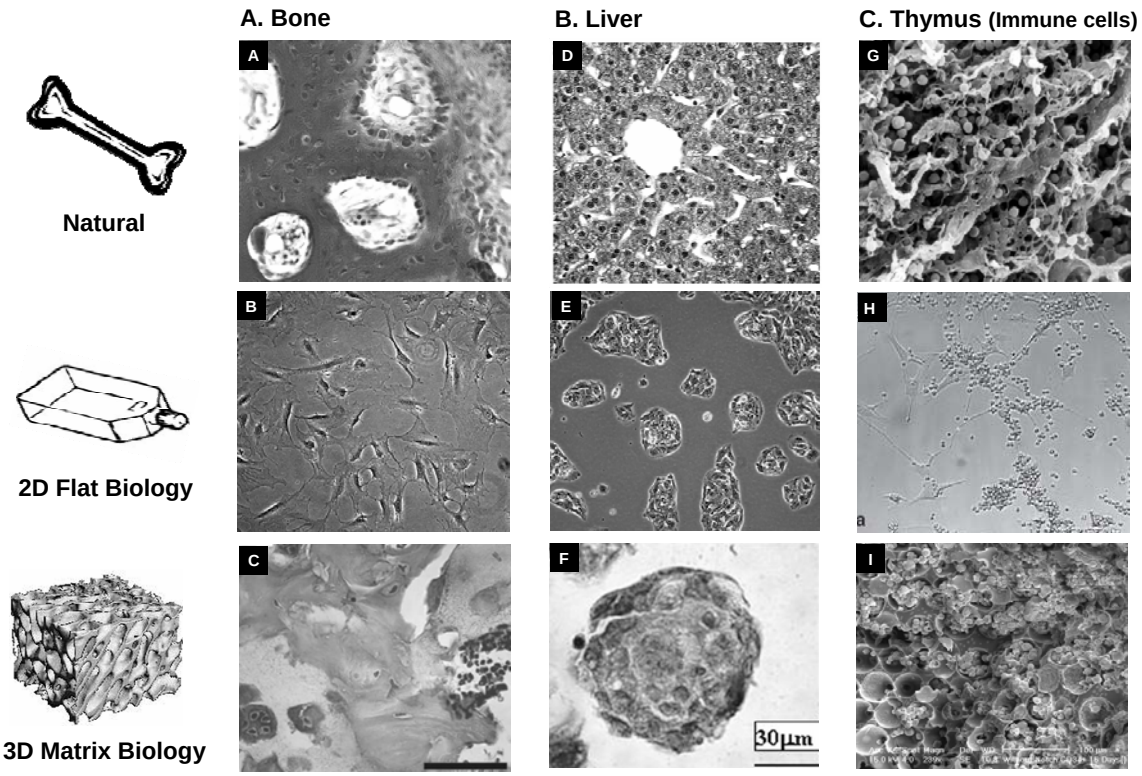

Figure 1.3 Comparison of natural cell/tissue morphology cultured on 2D and 3D substrates. Natural tissues and cells have distinct 3D organized morphological features; histological images of **(A)** bone and **(B)** liver[10], and **(C)** SEM image of thymus[26]. When tissue cells are cultured on 2D substrate, they show a similar morphological pattern i.e. stretched; optical microscope images of **(D)** osteoblasts, **(E)** hepatocytes, and **(F)** co-culture of lymphocyte-stromal cells[26]. Cell morphologies are closer to natural tissue when cultured on 3D matrices; different appearance of **(G)** osteoblasts[27], **(H)** hepatocytes[28], and **(I)** mononuclear cells in growing 3D formation.

The eventual goal of artificial 3D cell culture matrix design is to mimic natural ECM features sufficiently enough that cells function in the simulated environment as they would *in vivo*. Natural ECM is an intricate interwoven fiber meshwork of collagen and elastic fibers, embedded in a highly hydrated gel-like material of glycosaminoglycans, proteoglycans, and glycoproteins.[9] The unique compositional and structural combination provides appropriate biophysical and biochemical functions, such as facilitating the transport of soluble signaling molecules, nutrients, and metabolic wastes, and providing mechanical integrity of tissues by absorbing compressive and tensile

stresses.[10] The interaction between cells and ECM is dynamic. For example, ECM structure can guide morphological changes and cellular organization[29], and specific signaling molecules on ECM can direct cell differentiation into a particular lineage.[30] Cells also can respond to their local environment, remodeling local ECM by degrading and/or synthesizing new ECM elements.[31] As every tissue has a unique ECM environment, 3D cell culture matrix design should imitate certain features of ECM specific to each application. Nevertheless, there are also common characteristics to be considered, such as high porosity and biocompatibility.[32] In the following section, these common features in structural and material aspects will be reviewed focusing on structural properties that need to be considered at multiple length scale and essential material properties and some functional modification strategies.

1.2.1. Structures

A multi-scale approach to 3D matrix structure is especially important in mimicking living systems, as nature often derives properties from multi-scale or hierarchical structures that previously have been difficult to mimic. For example, bone has multiple organizational scales that yield superior mechanical properties, from interacting nano-scale collagen and hydroxyapatite crystals to micro-scale lamella and osteons.[10] With a growing variety of techniques to manipulate natural and synthetic materials, matrix design has become increasingly precise from the macro- to nano-scale. Multiple levels of structural control allow for the engineering of unique properties including matrix size and shape, pore size and geometry, porosity, pore interconnectivity, and surface topology. Here, the multiple scales accessible to 3D matrix design are

defined in three categories: macro-scale (10^{-1} ~ 10^{-3} m), micro-scale (10^{-3} ~ 10^{-6} m) and nano-scale (10^{-6} ~ 10^{-9} m).

Macro-scale design

The macro-scale structure (10^{-1} ~ 10^{-3} m) determines such properties of a 3D matrix as size and shape. (Figure 1.4A-B) For *in-vitro* 3D cell culture applications, the size and shape of a matrix can be controlled for convenience and functionality, i.e. fitting to a well-plate or bioreactor. In tissue engineering, it is important to match matrix size and shape to the anatomical defect. For example, a scaffold for bone tissue engineering should have a properly designed macro-scale structure to allow for integration with proper adjacent tissues, as well as for generation of properly sized tissue.[33] Appropriate design of anatomic shape also is important for cosmetic purposes. A major challenge of macro-scale control over implantable scaffolds is that the relevant properties (i.e. defect site size and shape) vary from patient-to-patient. One approach to achieve this level of design control is to utilize computer-based medical imaging tools such as computed tomography (CT), magnetic resonance imaging (MRI) and design strategies such as computer-aided design (CAD), become useful in customizing a 3D architecture to match a wound site.[19] This design can be manufactured utilizing SFF fabrication. The importance of macroscopic structural design of 3D matrices, along with their fast and individualized production, will become more important with increase the potential utilization of 3D cell culture matrices in clinical applications.[34-36]

Micro-scale design

Controllability on the micro-scale (10^{-3} ~ 10^{-6} m) is valuable to mimic microscopic tissue structure, such as the multi-cellular spatial organization within ECM proteins. Tissue architecture and function are closely interrelated. For example, blood vessels consist of the three distinct layers of endothelium, smooth muscle, and connective tissue. A circularly oriented smooth muscle layer surrounded by longitudinally oriented inner endothelium and outer connective tissue layers regulates blood flow.[10] Although micro-scale 3D matrix design should be specific for each application, there are also general but essential design parameters such as porosity, pore interconnectivity, pore geometry, pore size distribution, and some surface topography.

In addition to the diffusion of nutrients, metabolic wastes, and soluble molecules, one of the critical issues in microscale design is the facilitation of mass transport within 3D matrices to control the efficiency of cell seeding.[32] The inclusion of sufficiently sized open pores and a well-interconnected geometry improves diffusion throughout the scaffold interior. Pore geometry and pore size distribution are other critical factors. Three-dimensional matrices with similar porosity but dramatically different pore geometry, such as fibrous versus spherical pores, can yield different mass transport profiles. (Figure 1.4C-D) A large pore size distribution can lead to areas with poorer accessibility, potentially limiting cell seeding and migration efficiency.

Individual cells recognize structures which have comparable dimension to cellular size (10~100 mm).[37] Therefore, micro-scale surface morphological texture needs to be considered among design criteria. Micro-scale surface features can activate certain genes and modulate cellular behavior in differentiation or proliferation. For example,

microscopic surface patterns and grooves on 2D surfaces guide neuronal cell polarization[38] and myoblast alignment.[39] Beyond that, there is a poor understanding of how the topology of 3D scaffolds affects cell development. For instance, it is difficult to answer how the change of fibrous substrate to a support with leached pore morphology affects the differentiation of stem cells.

Micro-scale structural design also affects the mechanical properties of the bulk scaffold. Sufficient mechanical properties are important in tissue engineering, in which the scaffold may be required to withstand forces generated by the body, and in 3D cell culture, in which the matrix must withstand cell attachment forces, handling by scientists, and media convection in bioreactors. Oftentimes, a stochastic micro-structural architecture, such as those resulting from particulate leaching fabrication techniques, requires high porosity to ensure complete interconnectivity. The high porosity sacrifices mechanical properties by reducing the amount of material present in the matrix. Precise design of matrices, where architecture is optimized to provide complete interconnectivity at higher porosities, can improve mechanical strength while preserving effective diffusion.

Overall, some of the most fundamental matrix design criteria require control on the micro-scale. With improving technologies, it is becoming increasingly obvious that precise micro-scale design is necessary to maximize these microscale properties. Although there are numerous fabrication methods to make 3D matrices with micro-scale resolution, only few techniques, such as SFF fabrication[40] provide precise controllability over 3D matrix architecture at this scale.

Nano-scale design

Cells interact with ECM via nanoscale proteins, responding to their environment by modulating various cellular activities. Therefore, specific attention to matrix design on the nano-scale ($10^{-6} \sim 10^{-9}$ m) is logical, because most individual ECM components are in nano-meter scale. For example, collagen fibrils have a diameter range of 50 to 200 nm, and fibronectin are 60 to 70 nm long and 2 to 3 nm thick.[9]

Aside from the inhibition of nutrient supply by microscale geometry, nano-scale structural features provide the most significant influence on cell functions as a part of surface topography. This is not surprising because many cell-signaling mechanisms involve nano-scale molecules. Nano-scale surface topography has been demonstrated to regulate cell adhesion, organization, morphology, and differentiation.[41] Still, compared with surface chemistry, limited 3D nano-scale fabrication techniques leave the effects of surface topology insufficiently investigated. Currently, nano-sized 3D surface structural features can be achieved in four ways. The first method involves using nano-materials such as 3D peptide hydrogels directly, entrapping cells in a 3D nano-scale fibrous structure.[42, 43] (Figure 1.4E) The second method incorporates nano-sized materials into bulk materials before matrix manufacture.[44] (Figure 1.4F) A great deal of research in bone tissue engineering has focused on integrating nano-sized features into scaffolds to improve osteoblasts adhesion, proliferation, and calcium deposition. For example, hydroxyapatite nano-particles incorporated into the matrix of poly-L-lactic acid (PLLA) scaffolds yielded nano-scale topology that significantly increased protein adsorption.[45] The third method controls processing conditions during fabrication. (Figure 1.4G) A nano-scale fibrous structure can be produced on the surface of a 3D

matrix through thermally induced phase separation of PLLA solution in organic solvent, followed by a crystallization process during freeze drying. Electrospinning techniques can also reduce fiber diameter to the nano-scale.[46] The last approach is post fabrication surface treatment or surface coating. (Figure 1.4H) For example, brief exposure of 3D polyester scaffolds to sodium hydroxide created nano-scale surface roughness, which improved the adhesion of osteoblasts and chondrocytes.[47] Although the above techniques are successful at generating nano-scale surface structures, feature controllability on 3D structures presents a major challenge.

Proper design of 3D cell culture matrix structure on multiple scales can provide distinct features to the matrix, such as macro-scale shape, micro-scale internal architecture, and nano-scale surface topology. Therefore, 3D biomatrix design should incorporate all scales to mimic the hierarchical structure of natural tissue that is correlated with cellular organization and functionality. However, controllability is highly dependent on material properties and selected fabrication processing, as will be discussed in later sections. Development of processing approaches that will allow freedom in choice of macro-, micro-, and nano-scale is one of the most difficult challenges in 3D scaffolds that the materials science and nano-technologist communities need to be addressed.

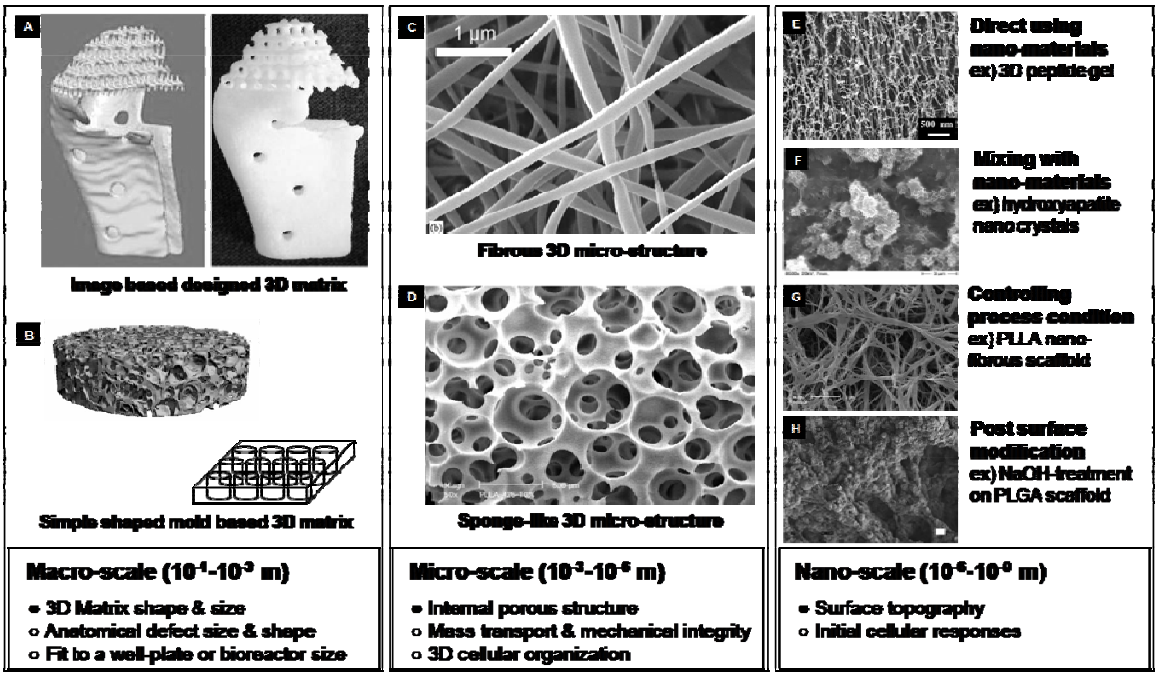

Figure 1.4 Overview of multi-scale 3D cell culture matrix structure design criteria (A[19]. B[48]. C[49]. D[50]. E[43]. F[44]. G[50]. H[51])

1.2.2. Biomaterials

As researchers are diverging from traditional 2D glass and tissue culture polystyrene, cellular responses to the materials are becoming increasingly apparent. Many new biomaterials have been developed to mimic the unique characteristics of natural ECM. In general, these biomaterials can be divided into four groups: metals, ceramics, polymers, and composites.[52] Among them, polymeric materials receive substantial attention because of the great flexibility in designing the composition and structure for specific needs. Polymeric materials can be divided into natural and synthetic polymers. (Table 1.1) Innate properties of these natural and synthetic polymers have been reviewed extensively elsewhere [22, 52-54], whereas commonly required features to design 3D matrices have not been comprehensively examined before. Beyond the increased controllability in chemical and physical properties of those synthetic polymers, the development of various materials engineering and hybridization techniques emulates ECM functions in an artificial environment. Here the key parameters are addressed in selecting and engineering polymeric 3D matrix materials from the viewpoint of bulk and surface properties. (Figure 1.5)

Table 1.1 Materials for 3D matrix building

Synthetic polymers	***Natural polymers***
Poly (glycolic acid) (PGA), Poly (lactic acid) (PLA) Poly (ε-carpolactone) (PCL), Poly (ethylene glycol) (PEG), Poly (vinylalchol) (PVA), Poly (propylene fumarate) (PPF), Poly(acrylic acid) (PAA), and various copolymers e.g. Poly (lactic-co-glycolic acid) (PLGA) *Peptide, DNA	Collagen, Gelatin, Hyaluronate Glycosaminoglycan, Chitosan Alginate, Silk, Fibrin, Matrigel

Bulk properties

Bulk material selection is the first consideration of 3D matrix design because it dictates various fundamental properties of the matrix from biological effects to processability. Here, several key parameters of bulk materials for matrix design are discussed including biocompatibility, wettability, transparency, biodegradability, and mechanical properties, as well as examples of bulk material modifications that are used to emulate natural ECM.

Biocompatibility of the bulk material is a critical parameter, because it determines the ability of materials to perform their desired functions with appropriate cellular or host responses. Biocompatibility can be understood as a graded characteristic, for which the requirements change depending on the specific application. The degree of biocompatibility can vary from the lack of toxicity with respect to transformed cell cultures to the lack of long-term immunological systemic response of the human body. The strictest requirements are applied to implantable scaffolds to avoid undesired responses, such as a strong immune reaction or fibrous encapsulation. Ideally, the body should be able to metabolize degraded substances. Natural materials tend to show better biocompatibility than synthetic materials, but their animal sources raise concerns about disease transfection. The more relaxed definition of biocompatibility is applied to 3D scaffolds to be used *ex vivo*, but the more complex the cellular system is, the more stringent the compatibility requirements are. Fabrication processes that use harsh chemicals decrease biocompatibility and sometimes cause matrix toxicity even if the bulk materials are biocompatible.

Because natural ECM is a fully hydrated gel, wettability is a key consideration.[55] Bulk materials with more hydrophilic chemistry are better at mimicking the aqueous in vivo environment. For this reason, hydrogels, networks of hydrophilic polymer chains, have been used extensively as 3D matrix materials.[53, 56] The hydrogel structure also creates a gradient of soluble signaling molecules within a 3D matrix and absorbs mechanical tensions. Nevertheless, poor cell adhesion due to the hydrophilicity of hydrogels and the lack of cell binding motifs is a common drawback.[53] These limitations can be overcome by conjugating cell-binding motifs such as arginine-glycine-aspartate (RGD) on polymer chains[23] or by coating surfaces with bioactive materials post-fabrication.[57]

Transparency of bulk materials is an important parameter for 3D in vitro modeling applications in which cellular behaviors within the 3D matrix require microscopic detection. Many sensing and quantification techniques, such as immunostaining and enzyme-linked immunosorbent assay, also use optical-based instrumentation, including confocal microscopes and micro-plate readers. Thus, transparent materials are advantageous to collect optical signals passing through the bulk structure without dissipating light beam. One may also consider a broader definition of transparency beyond the traditional ultraviolet-visible spectroscopy ultraviolet-visible spectroscopy (UV-vis) range of electromagnetic waves between 300 and 800 nm. Transparency in the X-ray region is reasonably high for most materials, which will be important to use for analysis of cell behavior in 3D scaffolds. X-rays can penetrate to depths that are not possible for confocal microscopy images even in the most transparent media. However, X-ray contrast of live cells in most 3D matrices is poor. The

development of appropriate contrast agents for cells for 3D X-ray tomography using nano-particles is a burgeoning research area with much promise.[58-61] Much contribution can be made in this field by further improving image contrast and resolution particle delivery to the cells and introducing X-ray ‘‘color’’ with different nano-particles, which will greatly improve the research process in 3D scaffolds.

Controlled biodegradability is an essential requirement for implantable 3D scaffolds, because these scaffolds are generally designed to degrade at the rate that in-growing tissue replaces them. Generally, synthetic materials degrade hydrolytically[62] and natural materials undergo an enzymatic degradation process.[63] Hydrolytic degradation is more predictable and adjustable than enzymatic degradation. For example, the degradation profile of poly(lactic-co-glycolic acid) (PLGA) scaffolds can be manipulated by adjusting the composition and molecular weight of poly(lactic acid) (PLA) and poly(glycolic acid) (PGA) polymers.[64] On the other hand, enzymatic degradation of natural materials is more dependent on local enzyme concentration secreted from cells.[65] Thus, the degradation profile and mechanism under physiological conditions for scaffold materials, as well as the implantation site and desired scaffold function, need to be carefully considered when designing an implantable scaffold.

Mechanical properties of bulk materials represent an important set of characteristics to consider in 3D matrix design. First, bulk materials are fundamental contributors to the mechanical integrity of 3D matrix structure. This is especially so in tissue engineering for structural tissues. For instance, bone regeneration scaffolds may endure substantial mechanical stresses immediately after implantation.[66] If the

scaffold cannot bear sufficient loads, it might fracture before the bone healing process is complete; however, excessively strong mechanical properties can damage adjacent bone or retard new bone regeneration via stress shielding. This becomes even more complicated when bulk materials start to degrade, because the mechanical properties of the scaffold should retain integrity and gradually transfer loads to ingrowing bone. Therefore, the scaffolds should have mechanical properties resembling those of healthy tissue over the period of tissue regeneration.

Second, the bulk mechanical properties directly shape surface mechanical properties, such as surface stiffness or elasticity, which elicit clear cellular responses. For example, cells on 2D cultures initially recognize adhesive proteins on the substrate through transmembrane integrin receptors receiving mechanical signals, which activate actin-filament polymerization and promote focal adhesion formation. Later, cells apply traction forces to pull the ligands from a substrate and sense the surface stiffness.[67] Recently, a modified fluorescence resonance energy transfer technique was used to measure cell tracking forces quantitatively on 2D substrates with different degrees of stiffness. It demonstrated that stiffer substrates support preosteoblast proliferation and that softer substrates promote differentiation.[68] In another seminal work, the response of human mesenchymal stem cells (hMSCs) on a 2D hydrogel matrix with different grades of elasticity was studied. hMSCs displayed a phenotype of neurogenic lineage on the softest substrates, a myogenic phenotype on moderately stiff matrices, and an osteogenic phenotype on the stiffest substrates.[16] Even though these results were derived from a 2D model system, they provide valuable information for 3D matrix design. For example, the timing of different functions of the scaffolds, such as early proliferation

and late differentiation, can be developed as a strategy for many tissue regeneration applications. A gradual switch from cell proliferation to cell differentiation can be obtained by progressive softening of the scaffolds during the biodegradation process.

Bulk properties are frequently modified to replicate the multi-functional tasks of natural ECM on an artificial 3D matrix. There are numerous materials engineering and hybridization techniques, but here three distinct strategies are discussed. The first approach involves hybridizing natural and synthetic materials to improve the biological and physical properties of a 3D matrix. For example, limited bioactivity of synthetic materials can be improved by covalently incorporating multifunctional ligands from natural materials (e.g., fibronectin, vitronectin, and laminin) onto synthetic polymers. [69-71] Depending on the application the ligand type and concentration can be adjusted. Weak mechanical properties of natural materials can be improved by incorporating synthetic polymers. Photopolymerizable hyaluronan and collagen conjugated with synthetic cross-linkers can be copolymerized with synthetic polymers.[72, 73] This significantly enhances the physical stability of the 3D structure in a controlled manner while preserving the inherent biological properties of natural materials. Currently, critical concerns are control over the spatial distribution of ligands and their configuration change after immobilization in a 3D matrix.

The second approach is the incorporation of soluble signaling molecules within a 3D matrix. In nature, the temporal release of soluble signaling molecules from ECM in a spatial gradient significantly influences various cellular behaviors. In 2D culture, the delivery of soluble signaling molecules is rapid and uniform but lacks a spatial gradient. It can be advantageous to create gradient signaling profiles in 3D culture, although

diffusion may be considerably impeded. For this purpose, soluble bioactive molecules, such as growth factors and deoxyribonucleic acid (DNA) encoded for the desired protein synthesis, are mixed in 3D matrix materials.[25, 74] Often these molecules are pre-encapsulated within biodegradable polymeric carriers, such as PLGA, for longer periods of release with a controlled profile. Encapsulation can also minimize the deformation of the 3D configuration of protein during the fabrication process. Moreover, multiple components can be secreted at different time points by taking advantage of different release kinetics. For example, Richardson et al. developed a dual growth factor–delivery system with different release kinetics in PLGA scaffolds: rapid release of vascular endothelial growth factor (VEGF) without a carrier and slow release of pre-encapsulated platelet-derived growth factor (PDGF).[75] VEGF first stimulated endothelial cell proliferation and channel formation, and PDGF recruited smooth muscle cells around the channels, which remodeled and matured the nascent vascular networks. As a result, the diameter and density of vessels were significantly greater than those of vessels in single growth factor releasing and blank scaffolds.

The delivery of DNA is also beneficial in maintaining physical integrity and enhancing effectiveness, because DNA is merely a 1D linear base sequence; preservation of configuration is not as much of a concern. Like proteins, DNA delivery is normally combined with viral vectors such as retroviruses and adenoviruses, but non-viral vectors, such as cationic polymers and lipid complexes, are also used to deliver the DNA sequence to cell nuclei.[76] Current challenges include the improvement of controllability in the carrier system and the enhancement of efficacy in delivered signaling molecules.

The third method that can be used to make an analogous ECM is to hybridize biomaterials with various functional nano-materials. For example, bone tissue ECM is composed of organic collagen and inorganic hydroxyapatite.[10] Polymeric materials only represent the organic element of bone tissue ECM; therefore, hydroxyapatite nano-particles are often incorporated, demonstrating greater osteoblastic differentiation than polymeric materials alone.[45] Recently, carbon nanotubes (CNTs) have been used as a hybridization material for 3D matrices because of their unique physical and chemical properties and flexibility of surface functionalization. The excellent mechanical strength of CNTs lends them to be incorporated into scaffolding materials for structural reinforcement.[77] Additionally, the metallic properties of CNTs allow them to be used as a contrast enhancement reagent for non-optical-based imaging tools.[78] Electrically conductive CNT composite films have also been applied for stimulation of neuron cells by electrical pulses.[79, 80] Moreover, CNTs support neuronal cell outgrowth and differentiation because their fibrous or tubular structure is similar to those of neural processes with comparable dimensions.[81] Although great potential exists for using nano-materials, several problems should be clarified, such as dispersion in nano-composite solutions, effective functionalization, biocompatibility, and potential systemic effects of nano-colloids in the body.

Surface properties

Surface properties are crucial in controlling interactions between cells and a substrate. Although surface properties are often derived from the bulk properties of materials, the bulk materials do not entirely define them, because 3D matrices are coated with proteins almost immediately after implantation in the body or immersion in culture media.[82] Surface chemistry and topography determine the identity, quantity, and conformational change of these adsorbed proteins.

Surface properties include stiffness, charge, polarity, and chemistry, among a multitude of others. For example, the surface charge density determines the amount of protein adsorption and resultant cell adhesion.[83] Greater surface charge brings a greater density of protein coating, leading to better cell adhesion.[84] Positively charged surfaces support better osteoblast adhesion than do negatively charged surfaces with similar charge density. It is believed that different protein species adhere to the scaffold depending on surface charge polarity, causing this distinction.[85] Surface chemistry also modulates the bioactivity of coated proteins by causing different configurations of adsorbed proteins. For instance, an equal amount of fibronectin pre-coated on 4 different substrate having OH, NH_2, COOH, and CH_3 functional groups resulted in adherence of different configurations of fibronectin and led to a specific class of integrin activation on osteoblasts. As a result, OH and NH_2 terminated surfaces supported better osteoblastic differentiation, alkaline phosphatase activity, and matrix mineralization than COOH and CH_3 groups.[86]

Surface properties can be modulated through the attachment of specific functional groups or proteins with necessary biological functions to regulate cellular behavior.

Fewer techniques are applicable to 3D substrates than to 2D biological surface modification methods because of limited diffusivity within the porous internal structures. Layer-by-layer (LBL) surface coating is a promising technique to modify 3D matrix surface properties with various materials.[87] LBL is described as the sequential dipping of a substrate into baths of oppositely charged solutions alternating with rinses in water, yielding monolayer control over the surface properties of the substrate.[88] Complex 3D porous structures can be coated using the LBL technique as long as there is no serious mass transport limitation. Various biomolecules can be incorporated in LBL films with minimal loss of bioactivity and can be delivered to cells in a sustained manner by using hydrolytically degradable polyelectrolytes.[89] For example, LBL films containing bone morphological protein-2 (BMP-2) and transforming growth factor-b1 (TGF-b1) mediated the bone tissue formation of embryonic stem cells.[90]

Vapor phase deposition is another technique to modify 3D substrates. Because this surface-coating process operates in the vapor phase, 3D matrices should be dried before processing. In a low-pressure chamber, monomeric compounds diffuse easily into the internal area of a 3D matrix, aided by air flow to reinforce diffusivity.[91] Plasma processing has been applied to coat 3D porous PLA scaffolds with amine groups to improve embryo 3T3 fibroblast adhesion. Amino groups grafted to the surface promoted adsorption of adhesive proteins, approximately doubling the number of cells initially adhering to the scaffold.[48]

Another interesting approach is coating 3D matrix surfaces with natural ECM by culturing stromal cells and removing them from the matrix. Because the natural ECM consists of a complicated mixture of organic and inorganic components originally

produced from cells, scaffolds coated with bone-like ECM secreted by osteoblasts significantly enhanced differentiation of rat mesenchymal stem cells (MSCs) into osteoblasts.[92]

There are a large number of criteria for the design of 3D cell culture matrices. On a structural level, there are multiple scales of features that influence the matrix function on cells, as well as the function of cells residing within the matrix. From a biomaterials point of view, bulk and surface properties have to be considered. Although they are not mutually exclusive, structural and biomaterial features can be chosen and manipulated depending on the desired application of the matrix. As discussed in the next section, 3D matrix design becomes increasingly complex depending on the chosen matrix fabrication technique, because the technique chosen limits the level of structural control and applicable biomaterials.

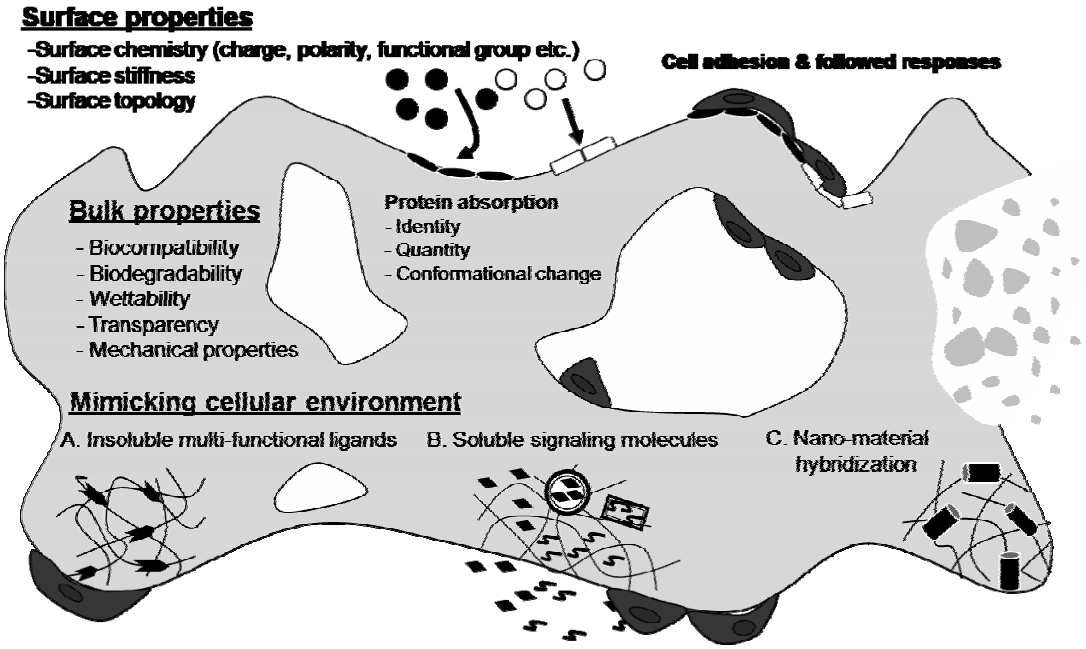

Figure 1.5 Summary of biomaterial considerations

1.3. Current fabrication techniques

Parallel to the development of advanced materials and process engineering, 3D matrix formation and fabrication techniques have evolved considerably to manufacture more elaborate 3D structures with a broad range of biomaterials. The earliest is the encapsulation of cells within a hydrogel matrix. In this culture format, a hydrated nano-scale fibrous structure similar to natural ECM surrounds cells are completely. Typical cellular behaviors, unrecognized on conventional 2D culture, became reproducible in this 3D culture environment.[93] Under the tissue-engineering theme, various micro-scale 3D porous matrix fabrication procedures were introduced. Many types of scaffolds are under investigation to construct pilot model tissues for bone[94], cartilage[95], skin[96], liver[97], blood vessel[98], and muscle[99]. Computer-assisted fabrication systems emerged with the greater necessity for complex and customized 3D matrix structure design and manufacture. Currently, the SFF technique, also called rapid prototyping, is the most broadly used of computer-assisted methods. SFF ultimately allows for control over macroscopic properties, such as scaffold shape, as well as microscopic internal architecture.[19] Conventional microfabrication technologies, such as soft lithography and photo lithography, have excellent control over micro-scale structure.[100, 101] Nevertheless, these manufacturing processes are limited to constructing freestanding 3D matrices. These structures are defined as 2.5D and excluded them from the scope of this review, except for a newly emerging multiphoton absorption polymerization (MAP) that can create an intricate 3D structure with a high aspect ratio.[102]

Although all of the fabrication methods have unique advantages, there is no one standard or superior fabrication process, and new methods are being researched. In this

section, current 3D matrix fabrication techniques are reviewed from the viewpoint of structural and materials design criteria and introduce some valuable modifications. Selected examples in each 3D matrix are also discussed in terms of in vitro models and tissue-engineering applications

1.3.1. 3D Cell entrapment

Technique

The process of 3D cell entrapment is conceptually simple. A hydrogel precursor solution is mixed with a cell suspension and then quickly gelled using random or self-assembling polymerization via changes of physical or chemical conditions.[103] The unique advantage of this technique is that cell culture is performed within a 3D environment that completely surrounds cells, enabling the delivery of intense signals to cells from all directions.

Structure

It is difficult to control the 3D matrix structure because of the rapid cell entrapment and gelling process. Normally, the mold in which they are formed defines macroscale structures. In the case that cell-entrapping precursor solution is dropped into an initiator solution, the structure takes on a spherical shape.[104] There is no distinct microporous structure; thus, mass transport mainly depends on slow diffusion through submicron-size pores. Still, the high water content (95.0–99.5%) enables sufficient exchange of essential biomolecules and metabolic end products to maintain cell viability in a limited thickness.[105] On the nanoscale, the interwoven mesh structure is beneficial

for emulating an in vivo physical environment. For example, fiber diameters of 10 to 150 nm are in a range similar to the size of ECM fibers, providing a similar atmosphere for cell growth Pore sizes of 5 to 400 nm are comparable to those of natural ECM, reproducing the slow diffusion of soluble molecules to create a gradient signaling profile within the 3D matrix.[105] Although the ECM-like environment is an ideal condition for cell culture, weak mechanical properties are a major limitation of the exceptionally hydrophilic nature of the matrix.

Biomaterials

Three-dimensional cell entrapping materials are natural or synthetic hydrogels that can undergo fast yet gentle polymerization around cells. The monomeric components must be nontoxic and biocompatible, because cells are mixed with the precursor solution before gelling. The polymers can be hydrolytically or enzymatically degradable. In addition, 3D hydrogel matrices show excellent wettability, and many demonstrate superior transparency in the UV-vis range. Surface properties of entrapping hydrogel are derived from bulk properties because 3D matrix completely surrounds cells. Stiffness and topography of the matrix can be manipulated by adjusting the concentration of monomer and cross-linker.

Natural hydrogels, like Matrigel, fibrin gel, and alginate gel, are commonly applied as cell-entrapping materials because of their outstanding biocompatibility and mild gelling conditions. However, some of the major drawbacks include poor control of gelation kinetics, uncontrolled material composition, and lack of mechanical integrity. Matrigel is composed of solubilized basement membrane proteins extracted from a rat chondrosarcoma. These soluble proteins undergo self-assembled polymerization when

incubated at 37°C, forming a 3D gel.[106] Although Matrigel is an excellent biomaterial because of its abundance of natural biological molecules, its heterogeneous and unidentified molecular components reduce a degree of experimental control. Additionally, the animal-derived source of the material may be contaminated with viruses, potentially affecting experimental results. For example, mouse-derived Matrigel is sometimes contaminated with a lactate dehydrogenase-elevating virus. Fibrin gel is made by mixing two blood coagulation components: fibrinogen and thrombin. Polymerization initiates when fibrinogen is converted to fibrin upon addition of thrombin. As fibrin polymerizes, interactions between polymers cause gelling into a 3-dimensionally organized clot, commonly seen in classic wound healing.[107] Alginate, a family of linear copolymers composed of 2 monomers (a-Lguluronic acid and b-D-mannuronic acid), is extracted from seaweed. The gelation of alginate occurs by adding ionic cross-linkers or divalent cations such as Ca^{2+}, Ba^{2+}, and Sr^{2+}. The quantity and binding affinity of ionic cross-linkers determine gel properties.[108] (Figure 1.6A-B)

Synthetic hydrogels have been introduced for greater control over physical and chemical properties of 3D culture environments. The homogeneous nature of synthetic hydrogels provides much better matrix uniformity and simpler biochemical assays than natural hydrogels. Additionally, it significantly promotes reproducibility of experimental results. For example, a 3D matrix constructed of simple peptide-based building blocks provides a blank background, minimizing noise in biochemical analysis. Thus, an assay determining the accumulation of cartilage ECM macromolecules (e.g., proteoglycans and glycosaminoglycans) synthesized from differentiated chondrocytes can be performed without concern about initial contamination of those molecules in the matrix.[109]

Synthetic hydrogels normally are not explicitly bioactive, and harsh polymerization conditions (i.e., free radical initiation and limited biocompatibility of monomeric components) frequently prevent the use of synthetic hydrogels as cell-entrapping materials.

Currently, three types of synthetic gels are used: poly(ethylene glycol) (PEG), peptide, and DNA gels. PEG hydrogel has been used because of its high biocompatibility and precise control of reaction kinetics during rapid photopolymerization, providing a spatially well-controlled 3D gel for cell entrapment.[110] (Figure 1.6C-D) Peptide gels are composed of macroscopically self-assembled synthetic peptides. Small quantities of elemental peptides (0.1 ~ 5.0 %) dispersed in water are mixed with a cell suspension, which then undergoes a self-assembling process under the right ionic conditions. Self-assembled peptides generate a stable nano-fibrous structure, entrapping cells. Two types of synthetic peptides currently used in this fashion are amyloid-like fibrils[111] and peptide amphiphiles.[112] (Figure 1.6E-F) Recently, DNA has been used as a building block to construct hydrogels with the invention of an oligonucleotide synthesizer to design a specific sequence of DNA and polymerase chain reaction to amplify the DNA. Elaborately designed DNA molecules, which have a branched structure with a complementary sticky end, can be hybridized to each other via DNA ligase, self-assembling into a 3D DNA hydrogel.[113, 114] (Figure 1.6G-H)

Natural and synthetic polymers are frequently hybridized to compensate for the shortcomings each may possess alone. For example, copolymerization of PEG and PEG conjugated with natural polymers such as hyaluronan[73], collagen[72], and biological

ligands[115] enables better control over the physical and biochemical properties of natural and synthetic cell entrapping materials, respectively.

Modifications

From a structural manufacturing standpoint, the cell-entrapping technique is based on the self-assembly of materials around cells, rather than the shaping of a bulk material to a specific architecture. Therefore, modification techniques are focused more on engineering unit biomolecules for directed assembly or to induce certain functionality than on manufacturing processes. The first example is advanced hybridization of natural and synthetic materials to create a cell-responsive 3D culture environment. Here, PEG macromers are covalently conjugated with cell adhesive and proteolytic cleavage ligands such as matrix metalloproteinase (MMP) degradation sites. [116] Cells cultured within this modified PEG-based hydrogel can grow and migrate deep into the matrix, creating spaces after local matrix degradation using cell-secreted MMPs. Hybridization also allows for a mild polymerization process separate from photopolymerization without generating free radicals, called a Michael-type addition reaction. In this process, gelation initiates after 2 building groups, end- functionalized macromers and bi-functionalized peptides, are mixed as cross-linkers.[117] (Figure 1.6I)

Another method of materials engineering involves the molecular design of unit peptides to have specific functionalities. Versatile alteration of amino acid sequences in the hydrophilic peptide head groups provides specific cell-binding or cell-signaling environments for the systematic investigation of cell differentiation.[118] (Figure 1.6J) The last example is a modification of the cell entrapping process involving a patterned multi-cellular organization instead of a random distribution of cells within 3D PEG

hydrogel. Positive dielectrophoretic forces generated along a micro-patterned dielectric mask direct the 3D spatial organization of cells suspended in a PEG precursor solution because of the negative net charge of the cell membrane. After PEG photopolymerization under UV light, the cells are fixed in a desired pattern.[119] (Figure 1.6K)

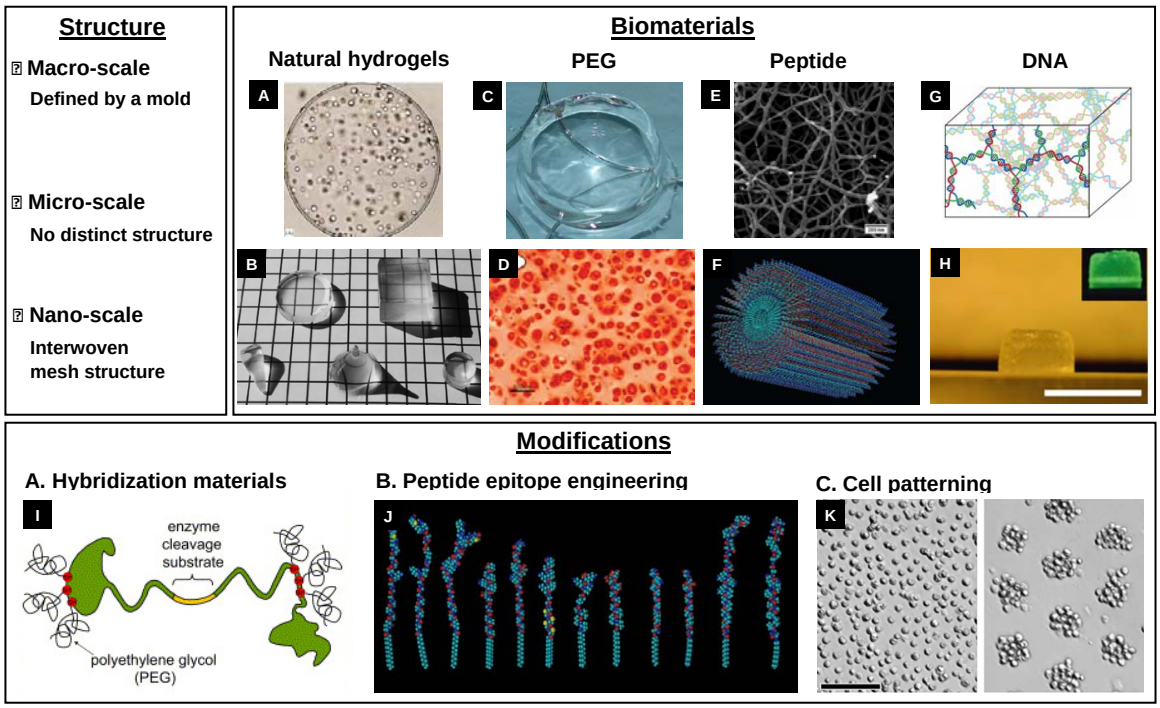

Figure 1.6 Overview of 3D cell entrapment techniques. (A) Fibroblast cells encapsulating alginate micro-spheres[104]. **(B)** Ionically cross-linked alginate hydrogels with defined macroscopic shape transferred from a mold[120]. **(C)** Photo-polymerized PEG hydrogel.[121] **(D)** Safranin-O stained cartilage cells entrapped in PEG hydrogel.[122] **(E)** SEM image of a peptide amphiphile nanofiber network.[123] **(F)** Illustration of self-assembled peptide amphiphiles forming cylindrical nanotubes.[123] **(G)** Schematic of DNA hydrogel structure.[124] **(H)** DNA hydrogel made in a cylindrical mold.[114] **(I)** Scheme for the preparation of MMPs sensitive PEG hydrogel.[125] **(J)** Examples of variation of self-assembling peptide amphiphile units.[123] **(K)** 3D patterned hepatocytes in PEG hydrogel, before (left) and after (right) patterning.[119]

1.3.2. Polymer processing to obtain porous 3D matrices

Techniques

Numerous polymer-processing techniques have been developed to fabricate 3D porous matrices with particular applications in tissue engineering. Specific details of each method are described extensively elsewhere.[54, 126] Here, representative polymer processing techniques that yield 3D matrices with a stochastic architecture are discussed, the structures of which are divide into fibrous and sponge-like. The internal structures of the 3D matrices discussed here are highly dependent on the chosen fabrication process.

Matrices with a fibrous structure are typically fabricated using an electro-spinning process that can continuously generate micro- or nano-scale diameters of fibers with simple set-up, inexpensive handling costs, and versatile material selection. The benefits of a 3D fibrous matrix include a high surface-to-volume ratio and a structure similar to the 3D fiber network of collagen and elastin in natural ECM. A major hindrance to cell culture is that small pores among fibers considerably hamper cell migration.

All other types of matrices displaying stochastic architecture can be described as having a sponge-like structure. Sponge-like 3D substrates have a porosity and surface-to-volume ratio that is similar to or lower than those of fibrous matrices but larger pores that can significantly improve cell seeding and migration. Sponge-like fabrication techniques can be divided into 2 groups based on whether a porogen is employed. Freeze-drying and gas foaming are widely accepted methods that do not use a porogen. The freeze-drying process includes blending a solvent–polymer mixture and an appropriate volume of water to form an emulsion. The emulsion is quickly frozen in liquid nitrogen and freeze-dried, leaving behind a porous structure where water has been evaporated.[127] The use of

organic solvents to dissolve polymer has been recognized as a major hindrance that can be avoided with gas foaming. The gas-foaming process involves high-temperature compression molding of the polymer to form a solid disk-like structure. The structure is then exposed to a high pressure CO_2 chamber for several days, during which the gas infiltrates the polymer. As the pressure is decreased, the gas escapes the polymer, leaving a porous, sponge-like structure.[128] The gas-foaming process is favorable for incorporating biological molecules because no organic solvent is used.[75]

Solvent casting and particulate leaching are representative methods of achieving a sponge-like porous matrix with a porogen. The concept behind particulate leaching is to mix polymer and solvent with particulates that can be dissolved with a separate solvent. Generally, synthetic polymers are dissolved in an organic solvent and mixed with porogen particles. Typical porogens include salt or sugar particles, because they are insoluble in organic solvents and can be removed by exposure to liquid water. The polymer–solvent–particulate mixture is then cast into a mold, and the solvent is evaporated, leaving a solid polymer–particulate construct. After exposing the construct to the particulate solvent, the remaining polymer will have a porous structure with empty cavities where the crystals resided.[18] Again, using an organic solvent is a major disadvantage. An important consideration of sponge-like structures is pore interconnectivity. In porogen-based techniques, particles in a porogen are frequently fused together, by exposure to greater humidity for salt particles or by heat treatment of paraffin spheres, to improve pore interconnectivity.[129, 130] Gas-foaming and freeze-drying processes can incorporate salts or sugar porogens in polymer solution to enhance pore interconnectivity as well as to control overall porosity.[131, 132]

Structure

The shape and size of the mold in which it is created or cutting or punching out a structure from a larger matrix piece normally determines the macro-scale structure of 3D matrices. (Figure 1.7A-B) Scaffolds often have a simple cylindrical or rectangular shape. In clinical applications, a patient-specific macro-scale scaffold structure is typically achieved by using 3D molds fabricated using computer-assisted fabrication methods; more detail will be discussed in the next section.

Characteristics of the micro-scale structure of fibrous 3D matrices include fiber diameter, fiber alignment, and pore size among fibers. (Figure 1.7C-E) Fiber diameter is sensitively affected by physical and electrical properties of polymer solution such as viscosity and conductivity.[17] Fiber alignment can be achieved by modifying the design of the collector (i.e., a high-speed rotating frame)[133] or by using 2 conductive electrodes separated by an insulating gap.[134] Pore size can be controlled by co-spinning of polymer solutions with different degradation kinetics, such as polycaprolactone (PCL) and gelatin[135], or by using multi-layer spinning to create 3D matrices having micro-fiber (~5-mmdiameter) and nano-fiber (~600-nm diameter) layers.[136] Here, by reducing fiber diameter to the nano- scale, nano-scale structural features can be achieved. (Figure 1.7I)

The micro-scale structural characteristics of sponge-like 3D matrices include porosity, pore interconnectivity, pore size and geometry, and pore-size distribution. (Figure 1.7F–H) The internal architecture of 3D sponge-like matrices manufactured without a porogen is entirely dependent on the fabrication process. Although relatively thick matrices are achievable, these matrices frequently have uncontrolled architectures

and isolated pores that limit cell–cell interactions and full tissue infiltration. A porogen-based technique can yield a more controllable and interconnected 3D microstructure, but the thickness is limited to less than 2 mm.[137] A moderate level of nano-scale structure can be controlled using post-fabrication surface treatments.[51] (Figure 1.7J)

The overall stochastic structure of this type of scaffold contributes to the simplicity of its preparation but may not be beneficial in terms of its mechanical and mass transport properties. Difficulties also exist with *in silico* modeling of biological processes in it and computer-assisted analysis of the 3D images.

Biomaterials

The electrospinning process employs a diverse set of synthetic polymers. Combinations of synthetic and natural materials (e.g., collagen, alginate, chitin, and silk) and functional nano-materials (e.g., CNTs, DNA, hydroxyapatites, and proteins) are also used as jetting materials. Concurrent spinning of different materials on the same collector can create scaffolds of multiple materials.[49, 135] Because of the absence of organic solvent, many biologically active molecules (e.g., growth factors[75] and DNA[138]) can be incorporated into PLGA-based bulk materials for scaffolds fabricated using gas foaming. In the solvent casting particulate leaching technique, salt crystals, sugar spheres, and paraffin spheres are commonly used as porogen particles. Virtually any material that undergoes liquid to solid transition can be used as a bulk material, but synthetic polymers, particularly PLA, PGA, and their copolymers, are commonly used. Many functional nano-materials and biological molecules can be incorporated with bulk materials and combined with carrier systems to protect biological molecules from organic solvents.

Still, considering these methods of scaffold preparation, there is an important problem that needs to be solved in the preparation of similar matrices with a high content of biodegradable inorganic material such as hydroxyapatite. This is important for bone implants and manufacturing materials with the stiffness necessary for bone engineering. Hybrid organic–inorganic materials with a high content of inorganic material in the composite similar to that observed in bone are difficult to make starting from polymer solutions.

Modification

The flexibility of polymer processing techniques enables the construction of 3D structures for specific applications. Teng et al. developed a PLGA-based 3D matrix with 2 distinct structures to treat spinal cord injuries.[139] The inner and outer regions of the 3D matrix were fabricated separately and then combined. The inner region, fabricated using a salt-leaching process (250- to 500 mm diameter) and consisting of larger pores, was seeded with neural stem cells (NSCs). The outer region, with smaller (<50 mm diameter) and axially oriented pores, was prepared using a solid–liquid phase-separation technique. Axially oriented smaller pores were designed to guide axonal extension and to allow proper fluid transport while inhibiting ingrowth of scar tissue. The NSC-seeded multi-component scaffolds were implanted into a rat for one year. Rats implanted with the scaffolds with NSCs showed significantly better functional recovery than lesion and cell-only control groups.[139] (Figure 1.7K)

Combining polymer processing techniques makes it possible to build 3D matrices with multi-scale structural properties. Ma et al. created nano-fibrous scaffolds with nanoscale (50–500 nm) fibrous surface textures on a micro-scale pore surface by

combining the particulate leaching technique and the phase-separation process.[140] A homogeneous mixture of PLLA and an organic solvent infiltrated into paraffin- or sugar-based porogen undergoes a polymer-rich and polymer-lean phase separation process below a critical temperature (-70°C). When freeze-dried, the polymer-lean phase ends, and the polymer-rich phase undergoes a crystallization process, generating a randomly organized nano-scale fibrous structure. The nano-scale fibrous surface morphology was an analogue of type I collagen fibrils on natural ECM, and the micro-scale open porous structure overcame the cell-seeding and cell-migration limitation of the electrospun matrix.[141] Combined with a modified SFF process, which will be discussed in the next section, the final scaffolds could have controlled macro- and micro-scale 3D structures, as well as random nano-scale structures, on the walls of the matrix. (Figure 1.7L)

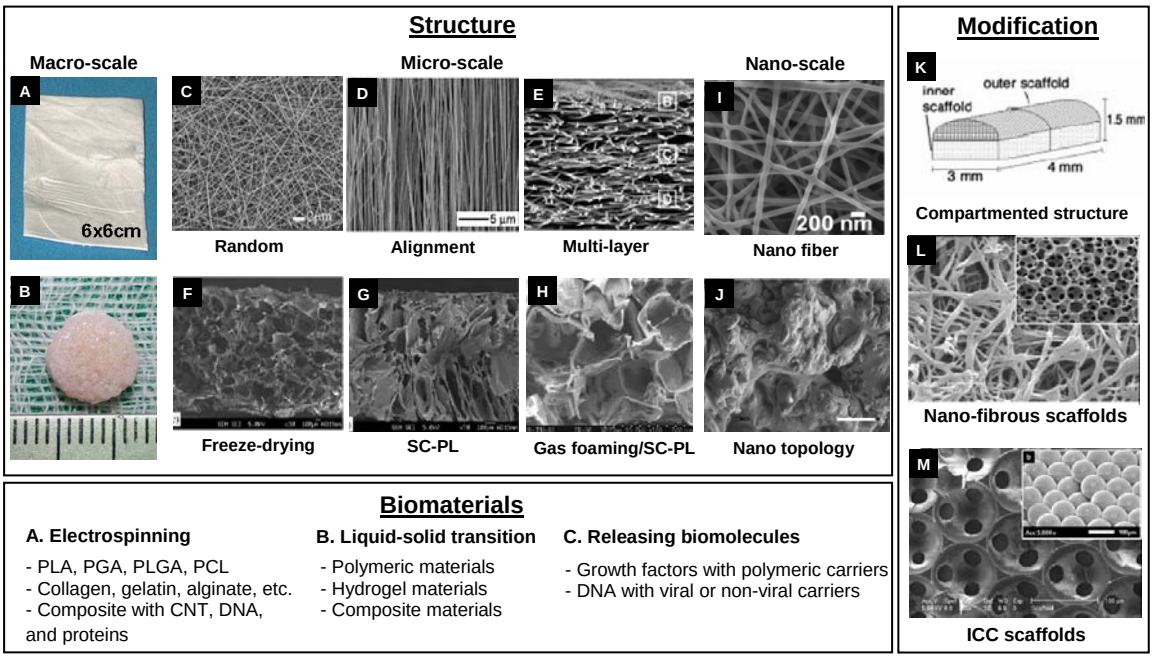

Figure 1.7 Overview of polymer processing techniques for obtaining porous structures. Macro-scale structure of **(A)** electrospun fibrous mesh sheet and **(B)** PLGA scaffolds.[142] Micro-scale fibrous structures (**C**[143], **D**[144], **E**[136]) and micro-scale sponge-like structure (**F-G[145]**, **H**[131]). Nano-scale **(I)** alginate based nanofibers[146] and **(J)** nano-scale topology after surface treatment[147]. Modification of polymer processing techniques: **(K)** compartmented scaffold structures[139], **(L)** nano-fibrous scaffolds[50], and **(M)** inverted colloidal crystal scaffolds.

1.3.3. Computer assisted fabrication

Technique

Computer-assisted fabrication has several advantages over non-computer-assisted fabrication techniques. Primarily, scaffolds can be manufactured as customized multi-scale 3D structures, which are essential for clinical applicability. Additionally, manufacturing is time effective and economical. Efficient manufacture is essential in clinical applications, in which the window for implantation is often critical. Currently, SFF fabrication is the most popular and powerful technique to construct 3D matrices with this level of design and efficiency.[148] The overall procedure of SFF fabrication consists of up to 3 steps: acquiring 2D image slices of a target specimen from CT, MRI, quantitative ultrasound, or other nondestructive imaging methods; designing micro-scale internal architecture and reconstructing the macro-scale 3D matrix shape using CAD or other software; and fabrication of the 3D matrix using automated layer-by-layer construction with SFF processes.[19] (Figure 1.8A–C) The 3 main types of SFF processing techniques are laser-based, nozzle-based, and printer-based systems. (Figure 1.8D) Laser-based techniques include photopolymerization and selective laser sintering (SLS). photopolymerization requires the exposure of liquid monomer solution to a UV beam, which polymerizes the exposed layer. The specimen, which is sitting on an elevator, is then lowered into a vat of monomer to coat the polymerized layer; this new monomer layer is then exposed to the UV laser to build the next layer.[149] SLS uses a laser beam to scan a powder bed, raising the temperature of the exposed area and sintering the powder into a fused solid.[150] Fused deposition modeling (FDM), a

nozzle-based technique, extrudes molten scaffold material through a nozzle as it moves in the x-y plane, directly building a layer of the scaffold with each sweep across its cross-section.[151] Another emerging extrusion technique is robocasting, which deposits a slurry of ceramic powder, a volatile solvent, and chemical modifiers through a syringe.[152] After a layer is deposited, it solidifies as the solvent evaporates, allowing for deposition of the next layer. After all layers are deposited, the structure is sintered. Three-dimensional printing is a process that deposits a liquid binder solution onto a powder bed using an ink jet printer. The binder solution causes powder particles to join and harden, forming the 3D matrix in layers.[153]

Recently, MAP, an advanced form of micro-fabrication technique, has been used in 3D matrix fabrication because of its significantly enhanced structural resolution and flexibility of architecture design. Here, an ultra-fast multiphoton generating laser beam is focused on a microscope objective. It creates local excitation within the focal volume of the beam, providing precise polymerization in the confined space.[102] By scanning the focal point in a pre-designed pattern, a complex 3D matrix can be constructed. [154-156]

Structure

3D matrix structural design for computer-assisted fabrication can be based on homogenization theory or CAD to design unit cells with various materials, porosities, and internal architectures. These unit cells are then combined for a desired overall architecture. This determined architecture is then used as instructions for the 3D printing of a matrix. These methods are discussed further below in the context of using SFF matrices as modeling tools.

An important potential for computer-assisted manufacturing that sets it apart from other manufacturing techniques is the ability to construct matrices with specific macro-scale architecture (shaped for a wound site). Still, the ability to build a matrix layer by layer in any 3D configuration is limited in many manufacturing techniques. For example, photopolymerization does not use a support material, which limits the possible shapes in which the matrices can be constructed.[148] FDM uses a support material, which allows for building in any direction and fabricating almost any shape matrix. For many materials, control over macroscale structures is limited.

Micro-scale features can be moderately controlled in that many geometries can be constructed, allowing for the design of numerous internal architectures. (Figure 1.8E-G) Still, the lack of support material also hinders the fabrication of certain cavity shapes, such as spherical or other rounded surfaces. Additionally, control of internal structure on the scale of a few hundred microns and smaller is limited because of inherent constraints of manufacturing parts (e.g., laser spot size, nozzle diameter, degree of position controller handing), as well as material constraints (e.g., particle size of powders). Currently, the minimum feature size is restricted to approximately 100 to 500 mm, depending on the fabrication process selected.[148, 157]

Matrices manufactured using SFF do not possess distinct nano-scale features, because the minimum resolution of most fabrication techniques is larger than 100 μm.[19] Most methods of introducing nano-scale features to SFF matrices are post-fabrication processes. Limited nano-porosity can be introduced into hydroxyapatite scaffolds by varying the sintering temperature. Russias et al. demonstrated the

precipitation of hydroxyapatite nanoparticles onto the surface of robocast printed PLLA/bioglass scaffolds.[158]

MAP provides an excellent alternative to overcome the limitations of the aforementioned methods of computer-assisted fabrication. 3D structures constructed using MAP provide excellent control over micro- and nanoscale, although the 3D matrix is dependent on a 2D mold.[154] With current techniques, the minimum resolution of one volume element exposed using multi-photon absorption (i.e. a voxel) is 100 nm.[102] Although MAP has been less investigated than SFF as a 3D cell culture substrate, its excellent controllability of structure holds great potential, particularly for the application of in vitro 3D model tissue construction. (Figure 1.8H)

Biomaterials

Customized hard tissue engineering has traditionally been the most promising application of SFF 3D matrices; therefore, the mechanical properties and biodegradability of bulk materials are stressed in these scaffold designs. Functional materials, such as calcium phosphate particles[159] and hydroxyapatite[160], are often mixed with basic bulk materials to mimic bone ECM composition. These composite materials often improve the mechanical properties of bulk material.[159] Surface properties have been emphasized to a lesser degree because of limited material selection and feature size control. Typically, the selected fabrication process determines the choice of applicable materials. For example, nozzle-based techniques are limited to synthetic polymers because the material is melted before extrusion. Here, PCL is extensively used in a FDM system because of its low glass-transition temperature and high decomposition temperature.[161] Printing-based processes, such as 3D printing, use mainly PLA, PGA,

and PLGA as basic building materials and chloroform as a binding solution.[153] The use of organic solvents is a problem with this method. For photopolymerization, the selection of precursor solution is limited to materials that can undergo UV polymerization (e.g. hydrogels and PPF-based polymeric materials).[162] SLS employs powdered materials such as ultra-high-molecular-weight polyethylene[163] and PCL[40]. MAP uses acrylate polymers that can undergo radical polymerization, such as PEG-diacrylate, and other materials including siloxanes, epoxy resins, and organic–inorganic hybrids.[102]

Modifications

Limited material selection and lack of submicron-scale structural resolution are the major shortcomings of SFF techniques. Indirect SFF was developed to alleviate these restrictions.[164] The original SFF matrix is used as a negative mold to construct a 3D structure with a broader range of materials. Wax is commonly used as a molding material because 2 types of wax, one for support and one for the mold, can be directly printed and easily removed after casting the desired matrix material. Various polymeric materials (e.g., PPF, PLA, and PLGA) and their composites with ceramics have been used as casting materials. Additional processing of secondary materials, such as phase separation of PLLA, can generate sub-micron-level structure.[165] (Figure 1.8I) A negative wax mold was fabricated using 3D printing, and PLLA was cast into the mold before phase separation at 20°C and dissolving the wax mold. This resulted in a nano-fibrous structure on the walls of the matrix that increased proliferation and mineralization of preosteoblastic cells.[165]

Three-dimensional cell printing is an interesting derivation of the SFF process used to construct a 3D cell–matrix hybrid structure. With most scaffolds, the method of

seeding cells onto scaffolds after fabrication can lead to limited 3D cell distribution and depth. A regular ink-jet printer or a SFF robotic platform is remodeled for use in 3D cell printing. A cell suspension is mixed into in situ cross-linkable hydrogels (e.g., gelatin, agarose, alginate gel) in a cartridge and then printed following a programmed 3D pattern. As a result, a 3D cell–matrix hybrid structure is constructed.[166] Cell viability as high as 90% indicates the ink-jet process conditions are not harsh enough to cause severe cytotoxicity.[167, 168] This 3D cell matrix with a spatially well-organized structure can potentially accelerate the organization of cells into a functional tissue. (Figure 1.8J)

Another way to build a 3D cell–matrix hybrid structure is 3D cell patterning. Instead of a typical SFF process, a modified photolithographic technique is used to build a patterned 3D cell–matrix construct. A mixture of cells and PEG–hydrogel precursor solution is deposited on a 2D surface, and a mask is placed on top so that only the unmasked area polymerizes under UV light. Multiple layers of a 3D hydrogel matrix can be layered atop previous layers. This method also significantly improves the homogeneity of cell distribution within a 3D matrix. Tsang et al. demonstrated a 3D hepatic tissue model constructed using this additive photo patterning technique, controlling the matrix architecture and optimizing hydrogel chemistry to attain high cell viability and liver-specific functions.[169] Currently localized cell seeding and spatially organized co-cultures are areas of active research. (Figure 1.8K)

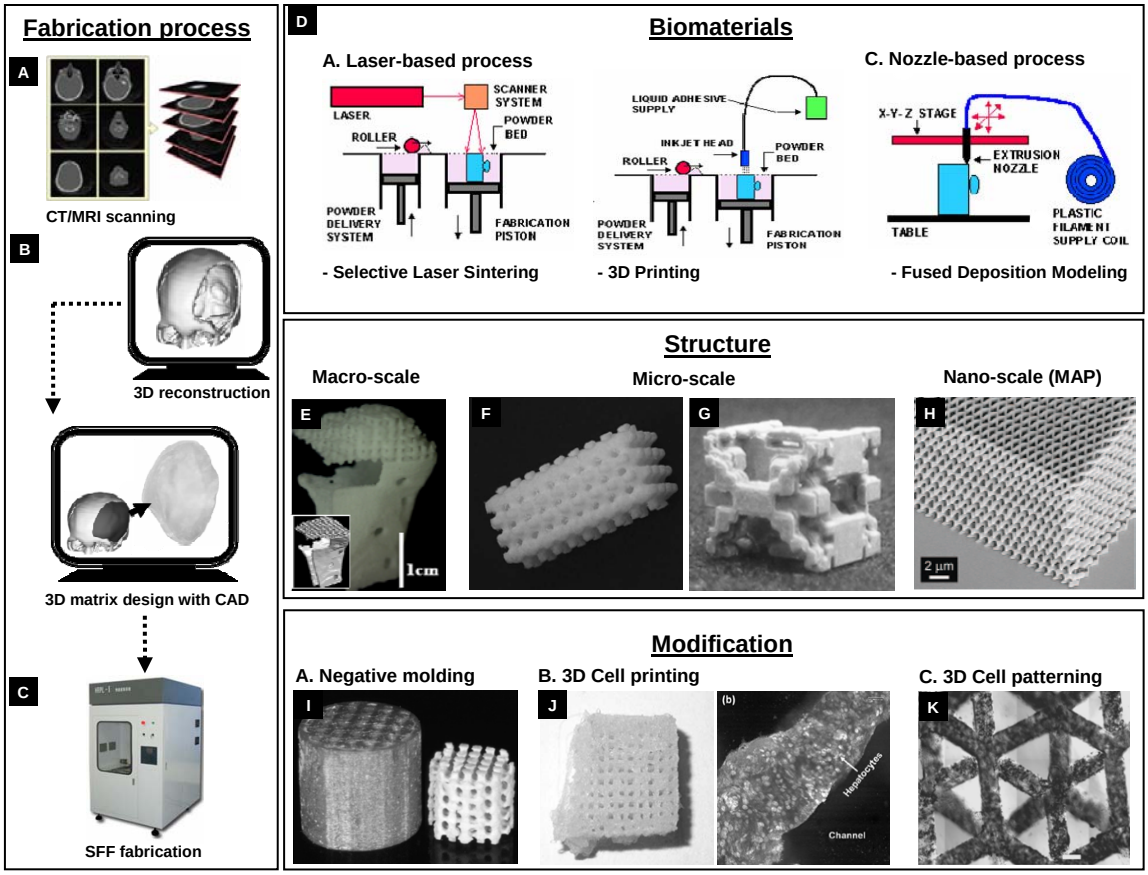

Figure 1.8 Overview of computer assisted 3D matrix fabrication techniques. (A) 2D scanning with μ-CT or MRI, image from (http://www.custard.org/~andrew/visualization/introduction/) **(B)** 3D image reconstruction and 3D matrix design with CAD software. **(C)** 3D matrix fabrication by SFF equipment. **(D)** Representative SFF fabrication processes, image from The Worldwide Guide to Rapid Prototyping (http://hime.att.net/~castleisland/) **(E)** Macro-scale scaffold design and manufactured by selective laser sintering method.[150] Micro-scale structures fabricated by SFF process: **(F)** selective laser sintering,[40] **(G)** 3D printing.[151] **(H)** Nano-scale structure prepared using MAP.[154] **(I)** Indirect fabrication using negative molding: wax mold (left) and cast ceramic mold (right).[164] **(J)** 3D cell printing of hepatocytes with gelatin.[167] **(K)** 3D cell patterning of hepatocytes in PEG hydrogel.[169]

1.4. Dissertation framework

This dissertation explores a new opportunity of *in vitro* tissue engineering as a part of the drug development process. Specifically it aims to create standardized human liver and primary lymphoid tissue models for the development of tissue based toxicity assays. Multiple studies have indicated that 3D scaffold structure and materials actively regulate the growth and differentiation of cells. Various recent efforts have successfully demonstrated *in vitro* tissue models that can recapitulate to some extent tissue level physiological behaviors. Nevertheless, practical applications of these models have been limited mostly due to batch-to-batch variation of experimental outcomes. One of obvious reasons is poorly controlled structure and materials of 3D scaffolds which in turn generate heterogeneous culture environment. Under this motivation, my key hypothesis is that standardized 3D scaffolds in their structure and materials can significantly improve the standardization of engineered tissue model.

The first part of dissertation is engineering 3D scaffolds that have highly regulated 3D structure and material, as well as can mimic both the 3D organization and the differentiated function of tissues in the body. In addition, 3D matrix accessibility through optical or other imaging tools and processability to precisely control matrix properties are other important consideration. Here, the inverted colloidal crystal (ICC) geometry and transparent synthetic hydrogel are the selection of the 3D structure and material.

The second part consists of engineering of *in vitro* 3D tissue models based on ICC hydrogel scaffolds. The specific goal is to replicate human primary lymphoid tissues, i.e. bone marrow and thymus, and liver tissue spheroids. Besides the functional tissue

development, standardization of tissues is equally important for running massively reproducible assays. ICC scaffolds promote homogenous and size controlled liver tissue spheroid formation.

The last part is the development of a tissue based *in vitro* toxicity screening platform. Ideally, the assay platform would be formatted to utilize already present laboratory equipment and assay reagents for easy acceptance from the pharmaceutical industry. In this line, liver tissue spheroid culture model was prepared in a standard 96/48 micro-well plate, the most commonly utilized *in vitro* cell based assay format. For this part, nanoparticle (NP) toxicity testing based on the standardized liver tissue spheroid culture model was demonstrated. (Figure 1.9)

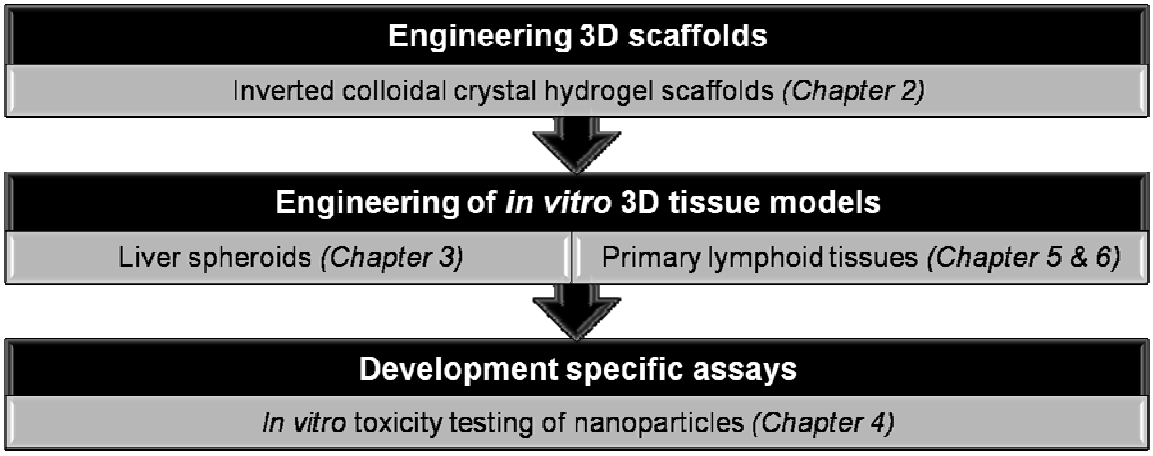

Figure 1.9 Dissertation framework

CHAPTER II

INVERTED COLLOIDAL CRYSTAL HYDROGEL SCAFFOLDS

2.1. Introduction

Scaffolds for *in vitro* drug development application should have three distinct properties: (i) biological significance in creating functional *in vitro* tissue models; (ii) standardized 3D structure and materials for the reproducible and homogenous tissue formation; (iii) easy handling and compatibility with existing hardware. Different from 2D culture substrates providing identical environment to universal cell types, each scaffold design should be optimized for the target tissue development. Simultaneously, engineered tissues must have a similar level of biological performance in order to generate reproducible assay outcomes. Consistent regulation of structural design and material properties of scaffolds should be preceded. Indeed standardization of assays is essential to realize the practical application of *in vitro* tissue engineering to the drug development process. Lastly engineered tissues need to be integrated into the current drug evaluation protocols for easy acceptance in the pharmaceutical industry. For this purpose, scaffolds should be transparent and compatible with micro-well plates.

Traditional scaffolds do not meet these requirements because they are primarily designed for clinical implantation. For example, the scaffold geometry fabricated by

particulate leaching, gas foaming, freeze-drying, and electro-spinning methods highly depends on the process which generates poorly ordered or chaotic structure. Recently, rapid prototyping, 3D deposition techniques[19] and multi-photon fabrication[102] were developed to construct more controlled 3D architecture assisted by computer-aided design and complex robotic equipment. Although these techniques allow researchers to design 3D scaffolds with desired properties including porosity, interconnectivity and pore size, they are heavily equipment-dependent and suffer from limited material section or inadequate resolution.

Colloidal crystals (CC) are hexagonally packed lattices of uniform spherical particles. Inverted colloidal crystal (ICC) is similarly organized structures where the spheres are replaced with cavities, while the interstitial spaces are filled. (Figure 2.1A) ICC represents an exceptionally dynamic area of research capitalizing on the unique spatial organization and diffraction characteristics of sub-micron scale lattices.[170-173] Although these structures are primarily designed for applications in optics[174], sensors[175] and catalysis[176], when the ICC pores exceed the single cell diameters (D > 10~20μm) the same structure can be used as a 3D cell scaffold.

Highly regulated ICC geometry becomes an exceptionally attractive 3D cell culture substrate for *in vitro* tissue engineering. Such unique ICC structure also can be easily and reproducibly prepared without the need for complex computer design programs and facilities, by taking advantage of utilizing CCs as a template. In addition, it enables to control multi-scale structure design. For example, microscale pore and interconnecting channel diameters can be readily regulated by changing bead size and annealing condition, respectively. Macroscopic shape and dimension can be tailored via a

mold design. In terms of biomaterials, any precursor solution capable of undergoing a liquid-to-solid transition while does not dissolve a CC mold can be used. In this thesis, polyacrylamide hydrogel is mainly used for scaffolding material because of its biocompatibility, transparency and good mechanical stability. (Figure 2.1B)

Besides the standardized structure and materials, ICC hydrogels open an interesting opportunity for a rather unexpected, but tremendously important area of science related to cell communication. In particular, the ICC scaffold modulates two distinct types of cellular interactions. First, the ICC geometry prepared with cell repulsive hydrogel matrix provides an ideal micro-environment for intense cell-cell contacts in static culture conditions which in turn promotes multicellular aggregation formation, so called spheroid. The spheroid formation restores original tissue-like morphology and functions corresponding to the increased cellular interactions that basically depend on the size of spheroids.[177]

Second, under dynamic culture conditions, surface modified ICC scaffolds induce intensive cellular interactions between floating and adherent cells. For example, floating cells can travel deep into the scaffold while temporarily entrapped in an ICC chamber due to the restricted channel size and dimension. As a result, they intimately communicate with the adherent cells growing on the surface modified ICC pore surface. Such cellular interaction is particularly important for the creation of hematopoietic stem cell (HSC) niches in the bone marrow and thymus where they undergo self-renewal and differentiation processes[178].

This chapter will focus on the fabrication of ICC hydrogel scaffold and the characterizations of their structural and physical properties. Specific applications will be discussed in following chapters.

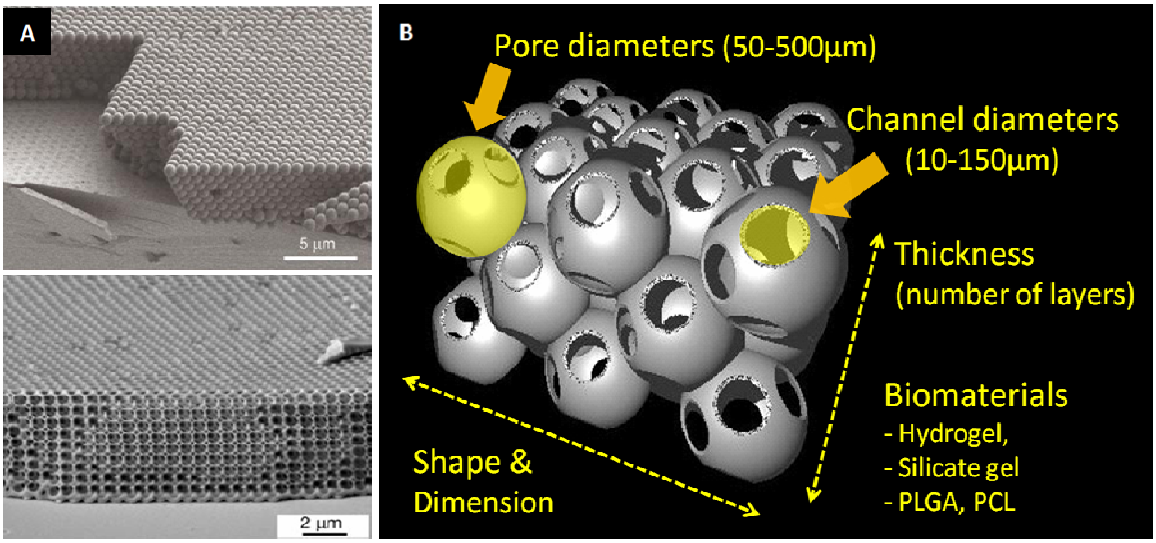

Figure 2.1 Schematic of ICC scaffold design and engineering parameters. (A) CC (top) and ICC (bottom) in photonic crystal research[179]. When the pore size exceeds a single cell dimension, the same structure can be used as a tissue engineering scaffold. **(B)** Schematic of ICC scaffold and engineering parameters.

2.2. Materials and Methods

2.2.1. Colloidal crystal construction

Utilizing uniform size of polystyrene microspheres (D=50-160 μm)

Polystyrene (PS) spheres with a diameter of 50, 100, 120 and 160μm (Duke Scientific, $3x10^4$ particles per milliliter and 1.4~4.8% size distribution) were dispersed in isopropanol solution before use. A 0.5ml plastic centrifugation tube was glued on a plastic dish and the top of centrifuge tube was cut and connected with a long Pasteur glass pipette. The complex unit was attached on the bottom of a glass beaker, and the

glass beaker was placed on the ultra-sonic bath (VWR). Two drops were released through a long Pasteur glass pipette in 15 minute intervals (25 intervals total) under gentle agitation generated by the ultra-sonic bath. To reduce thermal motions of the spheres, the bath temperature was maintained below 20ºC. After finished dropping, isopropanol was evaporated for overnight at 60°C. Prepared colloidal crystals were heat-treated at 120ºC for 4 hours, which caused partial melting of the beads' surface. As a result, PS microspheres fused together and the free standing colloidal crystal was extracted from the mold. Typical dimensions of CCs were 6.4mm in diameter and 0.5~1mm in thickness.

Utilizing uniform size soda lime glass microspheres (D=50-330 μm)

Dried 1g of soda lime glass beads with diameters of 50, 100, 140, 170, 200, 280 and 330μm (DukeScientific, standard deviation ± 2.2~5.7μm) were dispersed in 5ml of ethylene glycol. A borosilicate glass shell vial (D=8mm, H=35mm) (Fisher Scientific) connected with a long Pasture glass pipette was used as a mold for CCs preparation. The complex unit was inserted in a glass tube (D=10mm, H=75mm) (Fisher Scientific) that was halfway immersed in an ultra-sonic water bath, and the inner space of mold was filled with ethylene glycol. A few drops of glass bead suspension were released to the mold in 20-30 min intervals until the thickness reached approximately 0.5-1mm. After complete evaporation of ethylene glycol at 160°C, the CCs were annealed for 4 hours at 667-690°C depending on the size of beads. Annealed CCs were extracted from the mold.

Utilizing less uniform size of soda lime glass beads (D=75-300 μm)

Dried 500 g of soda lime glass beads with three different sizes (≤ 106μm, 150-212μm and 212-300μm) were purchased from Sigma-Aldrich. Using sieves and a sieve

shaker (Fisher scientific) the range of glass beads size was narrowed down in three groups: 75-90μm, 160-180μm, and 250-280μm. There are some other sizes, but most of beads were in these ranges. CC preparation was the same as the uniform size glass beads.

2.2.2. ICC hydrogel scaffold fabrication

ICC preparation with PS CCs

Hydrogel precursor solution composed of 30wt% acrylamid, 5wt% of N,N methylenebisacrylamide (NMBA) cross-linker and 0.5vt% N,N,N',N'-tetramethylethylenediamine (TEMED) was prepared with N_2 purged deionized water. The precursor was infiltrated into the colloidal crystal by centrifugation at 5800rpm for 10~20 minutes. An initiator, 1wt% of potassium peroxide solution was added and polymerization occurred in a glass vial. After completing polymerization, the colloidal crystal containing the hydrogel part was cut out and scratched with a razor blade to remove extra hydrogel covering CCs. Then the hydrogel-CCs were soaked in tetrahydrofuran (THF) for 24 hours to dissolve PS beads. Finally ICC hydrogel scaffolds equilibrated in deionized water.

ICC preparation with glass CCs

The precursor solution preparation, infiltration, polymerization and removal extra hydrogel steps were same as the PS beads case. After that, hydrogel-CCs were immersed in 5% (v/v) hydrogen fluoride (HF) solution for 24 hours to dissolve the glass beads. Later, ICC scaffolds were sequentially washed with pH 2~3 acid solution for 4~6 hours, phosphate buffered saline (PBS) solution for 1 day, and deionized water for 2 days. In each washing step, the solutions were changed at least 3~4 times. ICC scaffolds were

further freeze-dried to completely remove potentially remaining HF and kept in a dried state until used.

2.2.3. Characterizations

Confocal microscopy

Fluorescent ICC hydrogel scaffolds were prepared by adding 0.05wt% of fluorescent monomer (Polyfluor 511, Polyscience Inc.) in the hydrogel precursor solution. Fluorescent ICC hydrogel scaffolds were transferred to a glass bottom culture dish (MatTeck Corporation) and imaged with confocal microscope (Leica SP2) using a 470nm excitation laser utilizing 10X and 20X objective lenses.

Scanning electron microscope (SEM)

ICC hydrogel scaffolds were fixed in 2% cacodylate-buffered glutardaldehyde for 2 hours and then washed three times with 0.1M cacodylate buffer for 30 minutes. The fixed hydrogel scaffolds were dehydrated through a series of ethanol solutions concentrations of 50, 70, 90, 95, and 100% for 10 minutes. Dehydrated samples were further freeze-dried overnight and were coated with gold for 180 seconds using a sputter coater (Desktop 2, Denton Vacuum Inc.). Cross-section images of the internal architecture were obtained after cutting the sample with a razor blade. Samples were observed with a Philips XL30 or FEI Nova Nanolab SEM (The University of Michigan Electron Microbeam Analysis Laboratory)

Micro-computed tomography (μ-CT)

Colloidal crystals were three-dimensionally imaged by μ-CT to visualize their internal packing structure and to calculate porosity. The scan was performed by MS-130 high-resolution μ-CT scanner (GE Medical Systems) at 15m voxel resolution and 75kV.

Porosity calculation

Porosity of ICC hydrogel scaffold was measured combining an effective cellular porosity including only pores larger than single cell size (D=5~15μm) and bulk hydrogel porosity. μ-CT based image analysis was applied to calculate the effective cellular porosity. First, three-dimensionally rendered CC images were created with MicroView (GE Medical Systems). Image threshold levels were automatically adjusted. Then, the region of interest (ROI) set to include entire CCs, and the volume fraction of CC within the ROI was calculated with MicroView.

In order to calculate bulk hydrogel porosity, two assumptions were made: (i) specific density of water is $1 g/cm^3$ and (ii) pore space in a bulk hydrogel is completely filled with water. As comparing the volume and weight of a bulk hydrogel slab in both fully hydrated and dehydrated states, total weight of water and hydrogel polymer were calculated separated. Based on these data, bulk hydrogel porosity was estimated.

Mechanical testing

Compressive moduli of hydrated ICC scaffolds were measured at a constant strain rate (10μm/sec) using a mechanical properties tester and 1.1 lb load cell (TestReciurces Inc., MN).

2.3. Results and Discussion

2.3.1. Preparation of CCs with microspheres

The diameter of the spheres commonly used as CCs is around 100-1000nm for the purpose of matching the optical band-gap in the visible region. Various methods such as electrophoretic deposition[180], solvent evaporation[181], dipping[182], agitation[183, 184] and most recently spin coating[185] have been developed to construct the highly ordered CC structure. In order to utilize the unique geometry of the ICC as a scaffold, the sphere size has to be increased to the 10-1000μm range. However, it is difficult to obtain the same degree of order with micron scale beads using the methods developed for nanoscale spheres, mainly due to their larger volume and heavier mass. Fortunately, microsize beads offer two advantages over nanosize spheres. First, the agitation of beads by shear force works more effectively because of their larger volume.[186] Second, the sedimentation rate is faster due to their greater mass. However, the sedimentation rate was often too fast to self-assemble into a closely-packed ordered array. The opposite problem, *viz.*, how to retard sedimentation rate, was solved by introducing a Pasture glass pipette before beads entered into the mold. The pipette extended sedimentation distance and worked as a thin funnel, which caused a bottleneck effect for precipitating beads. (Figure 2.2A)

Once beads precipitated at the bottom of the mold, gentle agitation generated by an ultrasonic bath, assisted the movement of beads and positioned them at the lowest energy spots. This led to a highly packed and ordered array of spheres. When the bottom area was covered with beads, their rugged surface served as a template for the formation of the second layer. Since structural defects accumulated from the bottom area,

incomplete layers and less ordered arrays were usually observed on the top area. (Figure 2.2B)

The sedimentation rate was controlled further by adjusting the concentration of beads in the solution and the time interval between injections. For example, decreasing the amount of beads and increasing the interval period provided more time for the repositioning of precipitated beads. The use of isopropanol for PS beads guaranteed that the agitation was not too violent to destroy the whole structure, while its buoyancy made it easier for the PS beads to rearrange. Relatively high density of ethylene glycol (ρ=1.11g/cm^3) (c.f. water ρ=1g/cm^3 or isopropanol ρ=0.78g/cm^3) was used to retard the precipitation speed of high density of glass beads (ρ=2.5g/cm^3).

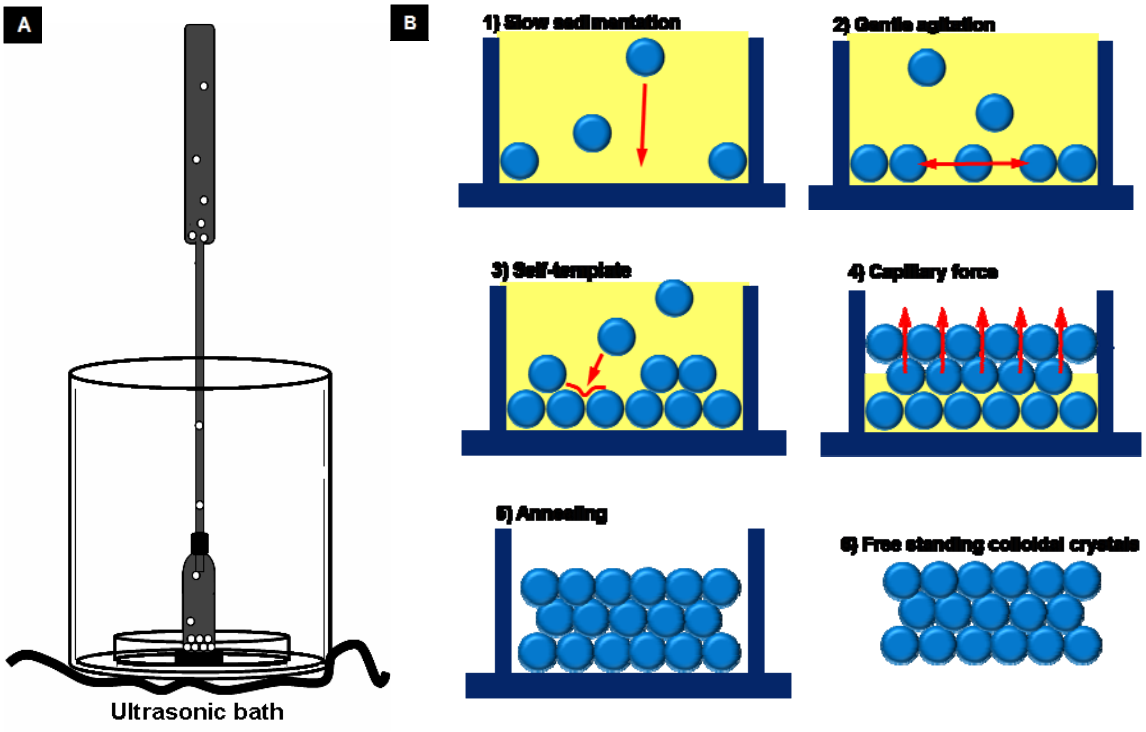

Figure 2.2 Colloidal crystal preparation (A) Experimental set-up: A long glass pipette is connected to a plastic or a glass tube mold immersed in an ultrasonic water bath. **(B)** CC construction procedure and key driving force in each step.

After sedimentation, the solution media were evaporated. During this process, capillary force further improved ordered bead packing. Following evaporation, the CCs were heat treated which resulted in partial melting of the spheres. This step allowed the beads to stick together and on subsequent cooling (re-solidification), junctions were created between the spheres setting the structure in place. The resulting free standing CCs were strong enough to be easily handled and removed from the mold. These junctions later prevented breakage of the crystal lattice during the infiltration of precursor solution and ensured the connectivity between spheres and continuity of the chain of pores in the final scaffold. The channel diameter was determined at this stage, because the size of melted area depended on the annealing temperature. However, too much annealing led to the cracking of the CC and/or incomplete precursor solution infiltration. SEM investigations of free standing CCs revealed highly ordered hexagonally close-packed structure. (Figure 2.3)

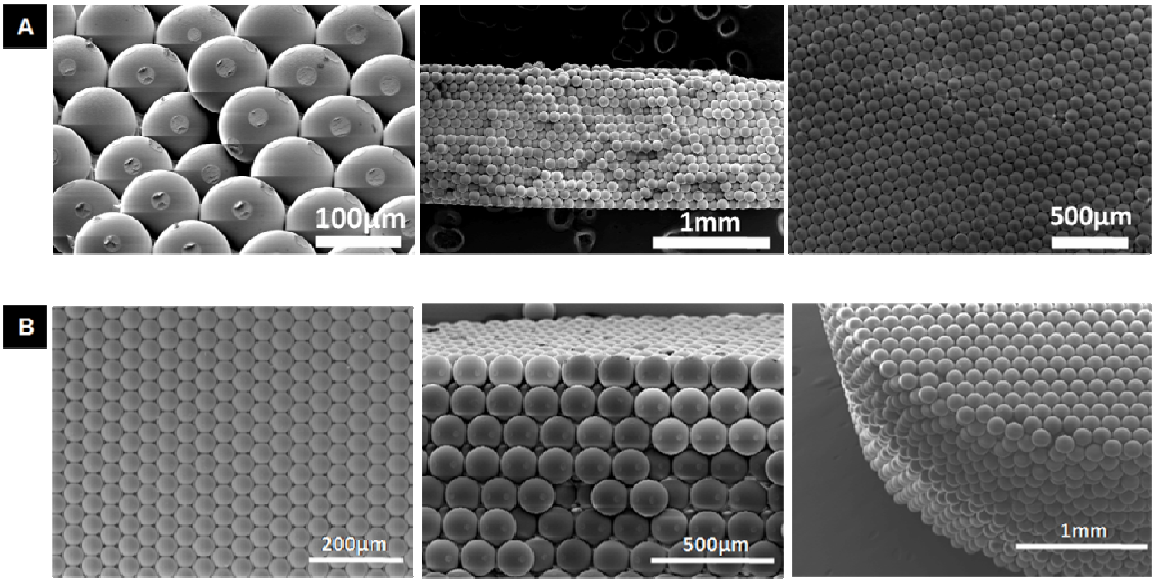

Figure 2.3 SEM images of free standing colloidal crystals. Different locations of CCs prepared with **(A)** PS beads (D=100µm) and **(B)** soda lime glass beads (D=160µm). Regardless of the bead sizes, highly ordered 3D packing structure was easily achieved.

2.3.2. Preparation of ICC hydrogel scaffolds

Polyacrylamide hydrogel was selected as a scaffolding material since the hydrogel is a broadly used in biomedical research fields due to its biocompatibility, mechanical strength, transparency, non-fouling property and cost effectiveness[53, 56, 187]. In addition, relatively low viscosity of the precursor solution compared to other natural hydrogel such as alginate, fibrinogen, and peptides allows easy and completely infiltration into the CCs. Monomer concentration was set low enough to prevent incomplete infiltration due to increased viscosity, and simultaneously to prevent deformation of the geometry during solvent extraction. Normally PS CCs are floating before the precursor solution infiltration due to entrapped air but they precipitate once the interstitial space is filled. In case of glass CCs, infiltration of hydrogel precursor solution is faster owing to their heavy weight.

After completion of radical polymerization, the transparent hydrogel including CCs was cut out and then CCs surface was scratched multiple times with a razor blade to remove excess hydrogel. In fact, the scratching step is critical to ensure open pores in the scaffold. PS and glass CC templates were dissolved by THF and HF solution, respectively. In THF solution, hydrogel-CCs shrank and turned white while in HF solution, hydrogel-CCs remained same. (Figure 2.4)

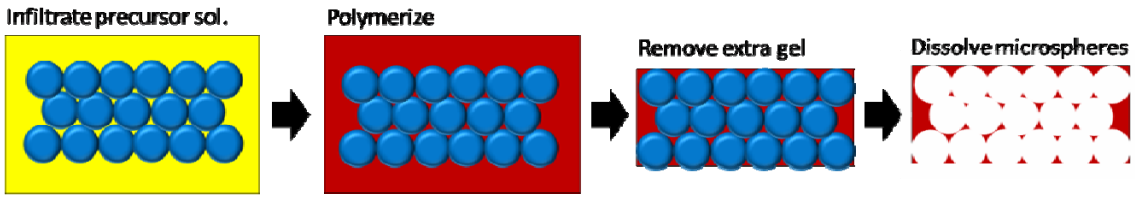

Figure 2.4 ICC hydrogel scaffold fabrication steps

The CC template structure was transferred to the ICC geometry intact. The diameter of the beads is directly proportional to the diameter of the resulting cavities. After stabilization in aqueous solution, the final hydrogel pore size was moderately (~10%) enlarged. This allowed near perfect fitting into a single well of a standard 96 well-plate. (Figure 2.7C) Similarly, the size of channels connecting the cavities can be tuned by the bead diameter, as the degree of contact upon annealing is greater for larger beads, and also by annealing temperature and time. Normally the channel diameters reach around 20-30% of pore size. (Figure 2.5)

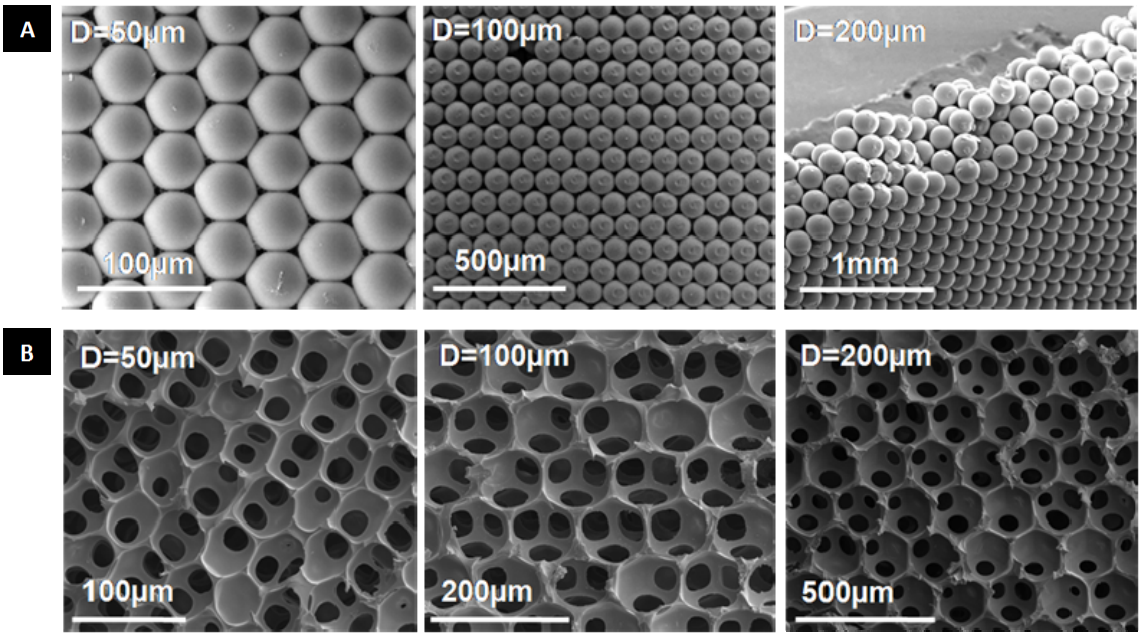

Figure 2.5 SEM images of three different sizes of CCs and ICCs (A) CCs prepared with 50, 100 and 200μm diameters of glass beads, **(B)** Hydrogel ICC scaffolds prepared with the three different bead sizes. Note that pore sizes in ICC hydrogel scaffolds were significantly shrank after dehydration process.

Pore and channel diameters were determined considering the single cell dimensions (D=5~20μm) and manufacturing superiority. For example, in our previous study of pore size effects, ICC scaffolds having 75 μm pore diameter favored bone marrow stromal cells nesting[188]. A 10μm pore diameter was too small for cell seeding,

whereas a 160µm pore diameter was too large for effectively cell entrapment. Also, O'Zinger et al. investigated osteoblast-like cell cultures on well-defined 2D cavities which were analogous to ICC scaffolds, and found that 100µm cavities favored osteoblast attachment and growth[189]. Considering these information, the smallest pore size was determined as 50µm because its channel size (~10µm) is comparable to a single cell dimension. The largest pore diameter was 330µm since the pore size larger than this can be manufactured utilizing other fabrication techniques[19], although producing a multilayer of spherical hydrogel cavities is still superior.

Polyacrylamide hydrogel retained excellent transparency which made it easier to monitor cellular processes deep inside the scaffold using optical and confocal microscope. Normally it was possible to observe the cell growth in ICC scaffolds at a depth greater than 500µm under confocal microscope. Transparency of the 3D matrix also improved its accessibility to optical-based assays (i.e. absorbance, luminescence or fluorescence) which are commonly used in pharmaceutical screenings. In addition, transparency enables easy sterilization of the scaffolds under UV light. (Figure 2.6)

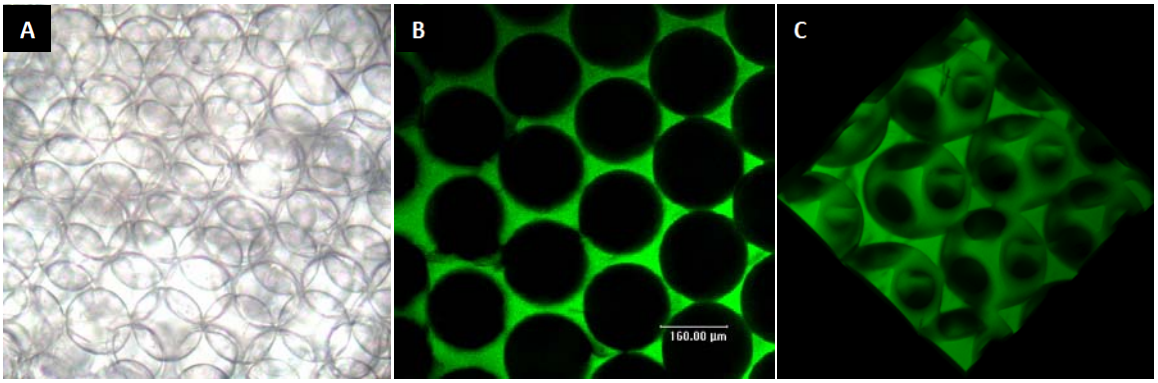

Figure 2.6 Transparent and fluoresent ICC hydrogel scaffolds. (A) Optical image of transparent ICC scaffold (D=100µm), **(B-C)** Confocal images of fluoresent monomer included ICC hydrogel scaffolds (D=170µm): **(B)** 2D section and **(C)** 3D reconstructed image.

Besides the standardization, running HTS assays is equally important to obtain statistically meaningful data. Currently micro well-plates are the standard format for HTS assays in the pharmaceutical industry, biotechnology and other fields. In order to improve the compatibility with HTS hardware, the macroscopic dimension of ICC scaffolds was tailored to fit with a single well of a 96 well-plate. (Figure 2.7)

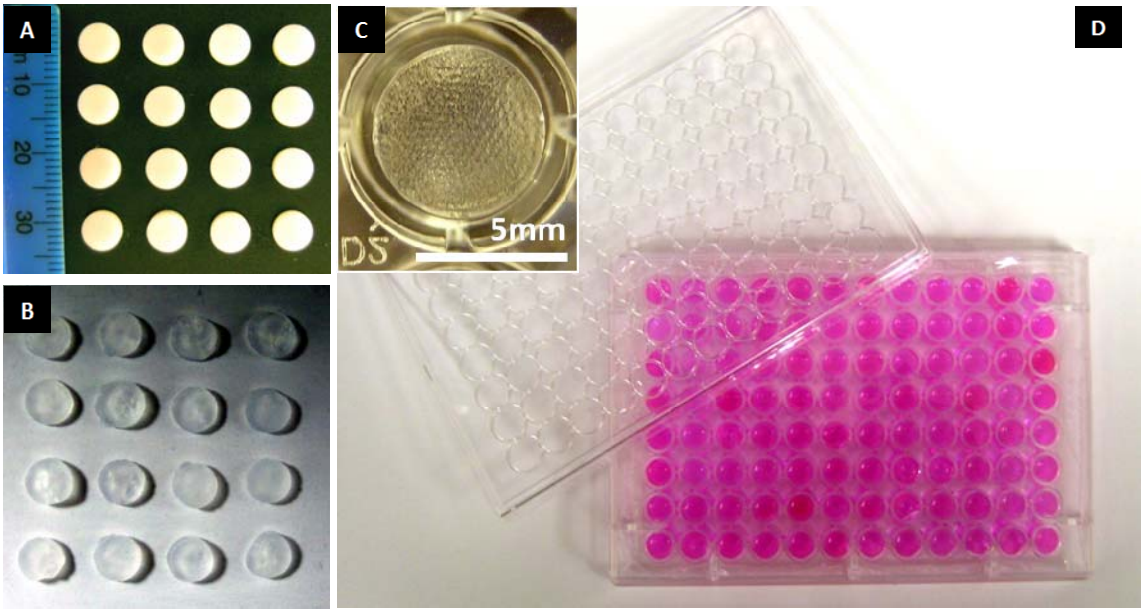

Figure 2.7 Optical images of ICC scaffolds compatible with a 96 well-plate. (A) CCs prepared with PS beads, **(B)** ICC hydrogel scaffolds, **(C)** The scaffold placed in a single well of 96 well-plate, and **(D)** Prototype of a 96 well-plate containing ICC hydrogel scaffolds.

2.3.3 Characterization of ICC hydrogel scaffolds

Porosity

An ICC hydrogel scaffold includes two different scale of pores; macro-scale pores which are larger than cellular dimension (D<10μm) (i.e. effective porosity) and sub-cellular (D<5μm) scale pores (i.e. bulk hydrogel porosity). (Figure 2.8A) The overall porosity of the scaffold should be estimated by combining these two porosities. An effective cellular porosity was measured by μ-CT image analysis that is commonly

utilized for estimating a fraction of bone in a defined volume, i.e. ROI.[190] The high contrast of microspheres, particularly glass beads, with background air produced clear 3D rendered images. In order to obtain an inverse volume fraction (i.e. the space of beads in the ROI), the protocol was slightly modified as subtracting the calculated percentage value from one. The ideal macro-scale porosity is 74%; however, the actual porosity is around 68% probably due to some loosely packed spots. (Figure 2.8B-C)

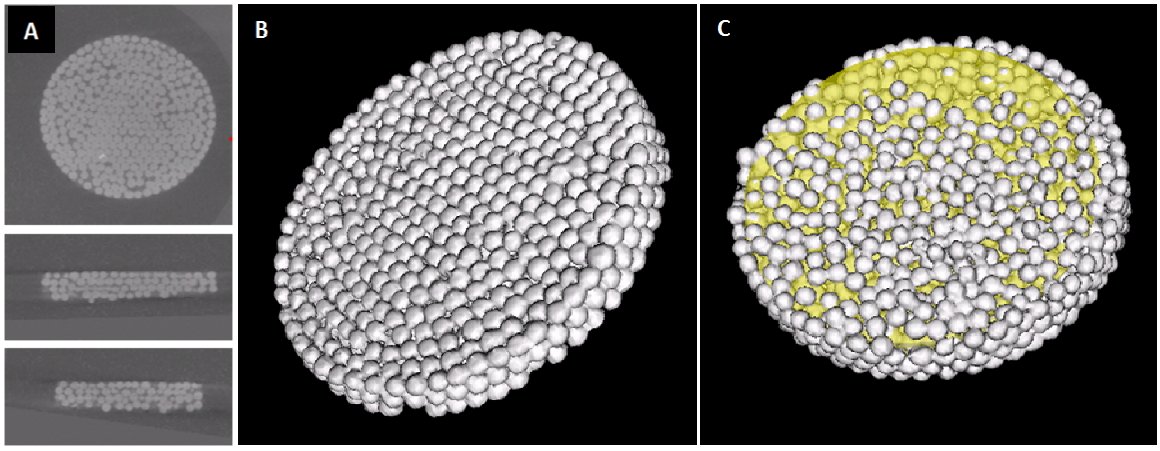

Figure 2.8 Effective cellular porosity calculation via μ-CT image analysis. (A) Row CC images of X, Y and Z section. **(B)** 3D rendered μ-CT image. **(C)** Define the ROI (yellow volume) for porosity calculation. (CCs were prepared with glass beads, D=330μm)

Bulk hydrogel porosity was calculated by measuring the water content in a hydrogel slab. As shown in Figure 2.9A, hydrogel matrix has a highly porous structure, and in aqueous solution, all these sub-cellular dimension pores are filled with water. Therefore, bulk hydrogel porosity can be approximated by calculating the percentage of water volume in a hydrogel slab as measuring the weight and volume of a fully hydrated and dried the bulk hydrogel slab. A volumetric fraction of water in the hydrogel slab was around 97%. (Figure 2.9B)

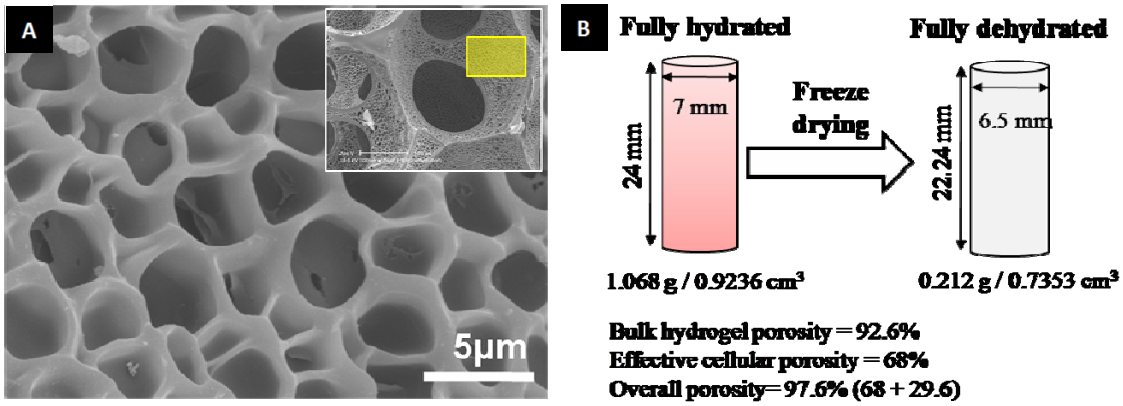

Figure 2.9 Bulk hydrogel porosity calculation via water saturation method (A) SEM image of sub-micron scale pores in a bulk hydrogel matrix. **(B)** Schematic of hydrogel porosity calculation procedure.

Mechanical strength

The compressive modulus of ICC scaffolds was 189.4 ± 5.89 KPa. (Figure 2.10) Compared to the mechanical strength of other porous hydrogel substrates, it showed stronger mechanical stability[191, 192] due to higher contents of polymer and highly ordered pore structure. Indeed the achieved compressive modulus was within the range of normal articular cartilage[193], adequate to construct artificial supports of soft tissues.

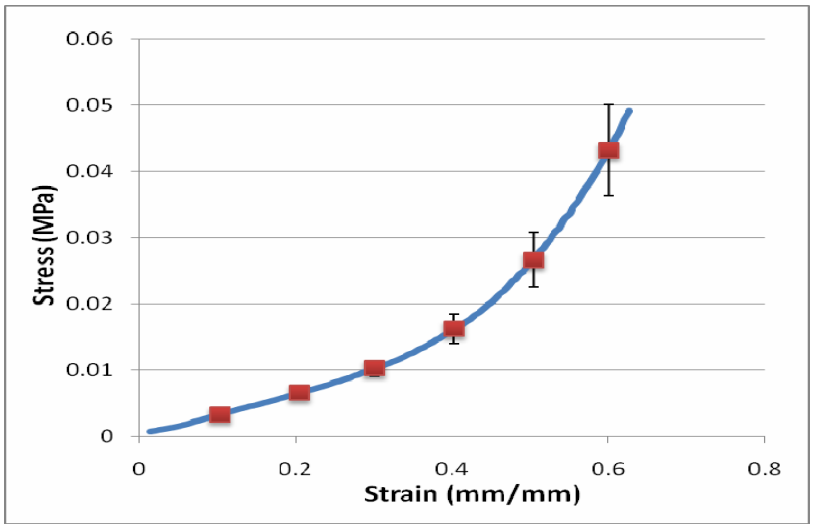

Figure 2.10 Mechanical testing result of ICC hydrogel scaffolds

Biocompatibility

Although the biocompatibility of polyacrylamide hydrogel has been extensively demonstrated, ICC hydrogel scaffolds can be potentially toxic since the fabrication process involves harsh chemicals such as THF and HF. To minimize such chemical induced toxic effect, the scaffolds were extensively washed with deionized-water and further dried to completely evaporate any chemical residue. According to our *in vitro* and *in vivo* experimental data in the following chapters, properly washed ICC hydrogel scaffolds did not induce any toxic effect, even after implanted into a mice.

2.4. Summary

The ICC hydrogel scaffold was developed in order to culture and test cells in a reproducible manner. The ICC matrix consists of empty spherical cavities arranged in a hexagonally array, providing a consistent and fully interconnected structural 3D microenvironment. The chosen scaffolding material provides a nontoxic, transparent and hydrophilic environment for cell culture. In addition, the hierarchical porosity makes possible efficient nutrient transport while providing a large surface area for cell adhesion. The scaffold can be provided as a stand-alone substrate or it can be fit into the wells of several sizes of well plates, which are the current standard format for HTS used in the pharmaceutical industry. Such unique features of ICC scaffolds would significantly improve standardized *in vitro* tissue development. As a result, it will serve as a valuable drug testing tool to link early-stage 2D testing to clinical stage human testing.

CHAPTER III

ENGINEERING HUMAN LIVER TISSUE SPHEROIDS

3.1. Introduction

3D spheroid culture has been used for *in vitro* models of various cell types including tumor, primary, and stem cells due to distinct advantages: (i) the extensive cell-cell interactions analogous to the *in vivo* environment promote the recovery of 3D structure/morphology and partial function of the original tissue physiology[29, 177, 194]; (ii) the culture can be maintained without vascularization since the diameter permits the penetration of oxygen and nutrients up to 200μm inside of the spheroid[195]; (iii) the spherical shape is beneficial in simplifying various tissue modeling problems, such as diffusion studies for drugs or toxic chemical penetration.[196-198]

Multiple techniques have been introduced to achieve spheroids. The general strategy is to prevent cell-substrate interactions while maximizing cell-cell interactions. Typical methods include the hanging drop technique[199], continuous agitation of suspension culture in a rotary cell culture vessel[200] or a spinner flask[201], preparation of cell repulsive substrates[202], and entrapment within biologically inert 3D hydrogel matrices[203, 204]. In these culture conditions, single cells spontaneously self-assemble and form a spheroid aggregate. Spheroid formation can be accelerated and controlled by

providing external forces (e.g. ultrasound trap[205] and micro-fluidic[206]) or confined geometry (e.g. micro-milling[207] and micro-molding[208]). Many of these techniques are fairly complex, offer little control over the spheroid diameter, and do not yield high numbers of the spheroids.[209, 210]

There are multitudes of open questions in cell biology involving cellular functions that may depend on cluster diameter. Spheroids of small diameters may or may not provide proper tissue-level physiological properties due to insufficient numbers of interacting cells, while large spheroids can suffer from hypoxia owing to the depletion of oxygen at the center.[177] Characterization of these cellular processes has been strongly impeded by large deviations in spheroid sizes that create different intensities of cell-cell interactions, thereby causing variation in cellular activity levels. Understanding the fundamental changes in cell biology with cell cluster size is quite important for tissue engineering, basic organ physiology, and drug discovery.[211-213]

This chapter introduces an ICC hydrogel scaffold-based spheroid culture system with conceptual advantages over other 3D matrixes stemming from the CC topology and materials selection of the scaffold. First, these scaffolds offer a high yield of spheroids with tight control over their diameters. Tight control of aggregate diameters is significant when considering assay development since this requires both a high degree of optimization and narrow experimental spread to enable discrimination of similar drugs. Second, the combination of hydrogel material and specific 3D ICC topology provide a unique hierarchical porosity of the cell growth matrix. Third, the described 3D matrixes are completely transparent that allow simple monitoring of cellular processes using traditional optical techniques while avoiding specialized experimental set-ups required

for some other 3D cell cultures. The dimensions of scaffolds were tailored to fit in a standard 96 well-plate. Human hepatocarcinoma cell line, HepG2, was selected as a model culture system for ICC scaffolds because of its well documented physiology, ease of maintenance, and practical usage for drug screening.[214, 215]

3.2. Materials and Methods

3.2.1. Pocket ICC scaffolds

CCs were prepared with uniform size glass beads (D=50, 100, 140, 170 and 200μm, standard deviation ± 2.2-5.7μm). Obtained free-standing CCs were transferred to a glass vial (D=8mm, H=5mm) and infiltrated with hydrogel precursor solution by centrifugation for 10 minutes at 5500rpm. Polymerization occurs after adding a radical initiator (1% (w/w) potassium peroxide) and accelerator (1% (v/w) TEMED). A hydrogel slab including CCs was taken out from the glass vial and only bottom side hydrogel was removed using a razor blade. The other side of hydrogel was cut out remaining only small amount of hydrogel (< 0.5mm). The glass beads were then dissolved with 5% HF solution and thoroughly washed sequentially with acid solution, PBS and deionized water. In this way, ICC hydrogel scaffolds have open pores only on top side while the bottom and edge side pores remain closed. Due to its pocket-like structure, it is named a Pocket ICC scaffold.

3.2.2. Cell culture within ICC scaffolds

Rehydrated ICC scaffolds were sterilized under UV light and then transferred into a 48 or 96 well-plate (Corning, NY). HepG2 human hepatocellular carcinoma cells (HB-

8065) (ATCC, VA) were maintained with Eagle's Minimum Essential Medium (EMEM) supplemented with 10% Fetal Bovine Serum (FBS) and 1% Penicillin-Streptomycin. Cells were cultured in T-75 culture flasks at 37°C with 5% CO_2 until they reached the desired population. Cells were detached from the culture flask using 2.5% Trypsin-EDTA solution. The concentration of the collected cell suspension was adjusted to $25x10^6$ cells/ml and then $5x10^5$ cells in 20 µl was dropped on top of ICC scaffolds. Cell-seeded ICC scaffolds were transferred to 48 and 96 well-plate and total culture volume was maintained at 1ml and 0.25ml, respectively. Half volume of media (0.5ml and 0.125ml) was changed every day. For 2D cell culture, 48 or 96 well-plates were used and $1x10^5$ cells were seeded and the half volume of culture media was changed daily.

3.2.3. Characterization of spheroid formation

Initial cell seeding profile and the diameter of mature spheroids were imaged using an inverted optical microscope with imaging software (QImaging). The number of cells initially seeded was further analyzed using ImageJ (NIH) software.

3D characterization of cell aggregation process was characterized using confocal microscope. For confocal imaging, HepG2 cells were stained with 5µM of fluorescent chloromethyl derivatives dye (CMRA CellTracer, Invitrogen) prior to seeding or after forming mature spheroids. During seven days, spheroid formation process on ICC scaffold was imaged. In addition, cell viability was observed using a Live/Dead Viability Kit (Invitrogen) under the confocal microscope.

Morphological evolution of single spheroid was characterized under SEM. Cell-scaffold samples were collected at different culture points (Day1, Day3, Day5, and Day7) and fixed with 2.5% glutaraldehyde solution. Fixed samples were dehydrated through

immersion into a series of ethanol solutions. After gold sputter coating, these samples were observed under SEM (FEI Nova Nanolab). Some samples were cut into several pieces before the dehydration step using a vibratome or a razor blade to observe the inside structure of spheroids. Histological sectioning and hematoxylin and eosin (H&E) staining were performed by the Tissue Core of the University of Michigan Comprehensive Cancer Center.

3.2.4. Liver specific functional assays

Albumin secretion

Albumin secretion from HepG2 spheroids with different sizes was characterized by a sandwich enzyme-linked immunosorbent assay (ELSIA) using a human albumin ELISA kit (Bethyl Laboratories, Montgomery, TX). 500µl of culture medium was collected every 24 hours and kept until analysis. Sample media was diluted 10 times and the standard curve was prepared using a reference human albumin. The assay result was normalized by total DNA.

Induced Cytochrome P450 (CYP450) activity

The spheroid culture was maintained for 5 days and the 2D culture was reached approximately 80% confluence before introducing an induction reagent, a 1µM of 3-Methlycholanthrene in William E Media for 3 days. The induction media was changed every 24 hours. As control groups, 0.1% Dimethyl sulfoxide (DMSO) and pure William E medium treated samples were also prepared. CYP450 activity was measured by the ethoxyresorufin-O-deethlylase (EROD) assay. The induction media was changed to a 500µl of 8µM 7-ethoxyresorufin and 40µM Dicumarol in William E Media. After 3 hours incubation, the media and cells/spheroid-scaffolds were separately collected. The

cells/spheroid-scaffolds were homogenized using the same way for dsDNA assay sample preparation. EROD activity from both the media and cells/spheroid-scaffolds homogenized solution activity was measured by the microplate reader. Also the DNA content from the homogenized solution was quantitated and used for normalizing the EROD assay results.

DNA quantification

Total DNA content of both 2D and spheroid cultures were measured using a PicoGreen dsDNA assay kit (Invitrogen). A spheroid-scaffold from 3D culture and a trypinzed cell suspension from 2D culture were transferred into a 1.5ml centrifuge tube, and 500µl of 1x cell lyses buffer (Promega) was added. The cells and scaffolds were destroyed under a brief (5-10 seconds) sonication. Sample solutions were centrifuged for 5 minutes at 1,000rpm and 25µl of supernatant solution was collected for DNA quantification. After adding assay reagents, fluorescent intensity at 590nm by the excitation at 540nm was measured by a Synergy2 microplate reader (BioTek, VT).

Statistical analysis

Measurement of pore sizes and spheroid diameters were completed in triplicate with five scaffolds in each group. Comparisons between multiple groups were performed with one-way ANOVA using SPSS software.

3.3. Results and Discussion

3.3.1. Pocket ICC scaffold design

Standardization of spheroid diameters and total cell numbers are critical issues in obtaining reproducible analytical results from the 3D spheroid culture. The biological activity of a spheroid is closely related to the size of its diameter.[216] For instance, spheroids having excessively small diameters would not have the proper tissue level of physiological properties and would instead remain at the cellular level due to the lack of cell-cell interactions. Increasingly large diameters cause cells at the center of the spheroid to suffer from hypoxia and inadequate nutrient transport owing to the limited diffusion of oxygen and nutrients.[177] As a result, a significant portion of cells ultimately undergo necrosis. Therefore, to achieve a homogeneous and meaningful level of biological properties, spheroids should have appropriate diameters with the narrowest size distribution possible. Also, total cell numbers need to be consistently regulated for the convincing quantification of intra- and extra-cellular proteins because these assay results are intrinsically dependent on the number of cells involved.

The ICC topology created with a cell-repulsive hydrogel matrix exhibits excellent physical and chemical properties for spheroid formation with a narrow size distribution while also retaining a high optical analytic capability. However, open porous ICC scaffold design releases a significant amount of cells right after seeding from the bottom or edge side pores, which caused difficulty in controlling the total cell number within the scaffold. Moreover, the released cells grew in a 2D environment on the bottom of the well-plate, hindering the reproducibility of the experiment and reducing the 3D culture effect. (Figure 3.1A&C) To circumvent this issue, the ICC scaffold design was slightly

modified to have open pores only on the top side, which is used for cell seeding, while pores on the bottom and edge planes are enclosed by bulk hydrogel to reduce the chance for cell loss. (Figure 3.1B&D) Although macroscale pores are sealed, sufficient oxygen and nutrient exchange is still maintained in the scaffold due to the presence of submicron scale pores in the bulk hydrogel.

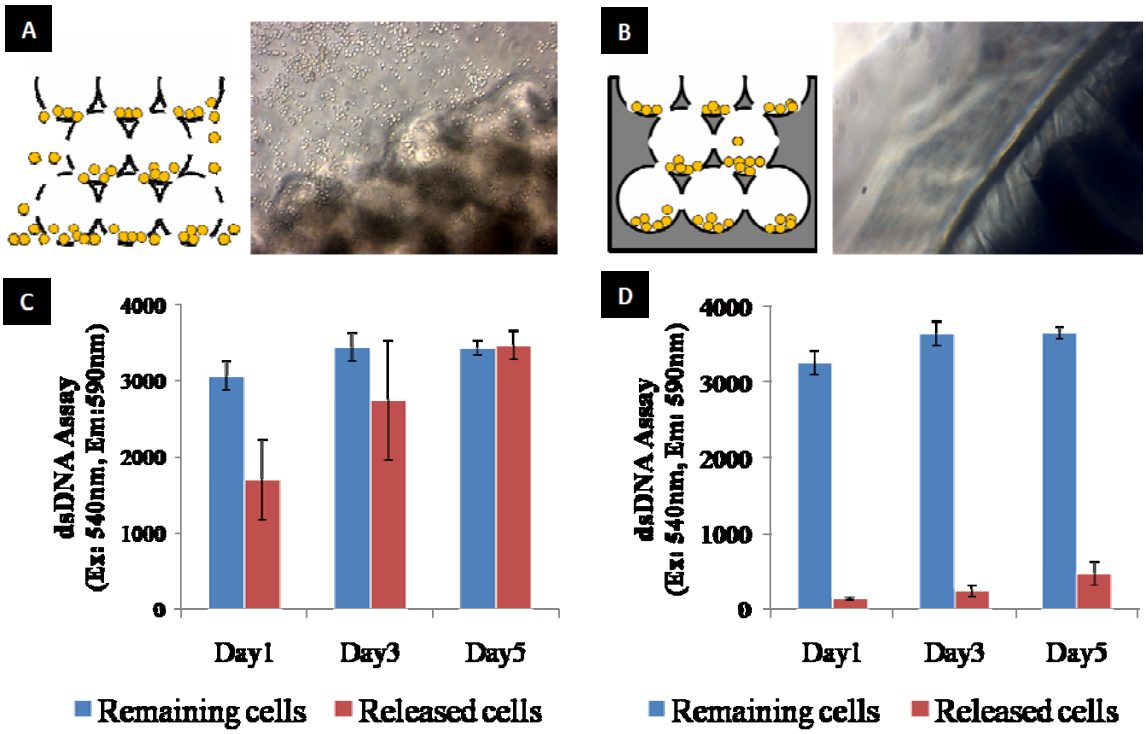

Figure 3.1 Comparison of cell seeding effect between open and pocket ICC scaffolds. (A) Open ICC scaffold loses a significant number of cells right after seeding: (left) schematic and (right) experimental images. **(B)** A pocket ICC scaffold considerably reduces cell loss through its closed bottom and edge plane pores: (left) schematic and (right) experimental images. Quantitative comparison of cell loss issue between **(C)** open and **(D)** pocket ICC scaffolds. Since cell proliferation in ICC scaffolds is considerably retarded compared to the cells on well-plates, after 5 days of culture, the amount of cells growing on a well-plate became similar to the amount of cells growing in open ICC scaffold. (n=5 for each time point)

3.3.2. Liver tissue spheroid formation

The initial cell seeding profile and the subsequent 3D cell aggregation process were characterized. The transparency of hydrogel matrix was beneficial to using confocal microscopy for this task. Homogeneous cell seeding was easily achievable with the inoculation of a dense cell suspension on top of slightly dehydrated scaffolds. The equally-sized spherical cavities promoted the distribution of consistent cell count within each pore. Non-fouling polyacrylamide hydrogel pores facilitate an initial cell aggregation followed by intensive cell-cell interactions while minimizing cell-substrate interaction. As a result, cells gradually self-assemble and form solid 3D spheroids over a period of 5 days. (Figure 3.2A)

Morphological changes during spheroid formation in the scaffolds can be categorized by several phases. (Figure 3.2) In the initial phase, cell aggregates are generally 2D in respect to curved surfaces of the pores and individual cells are easily distinguishable (Day 1). Subsequently, cell sheets begin to coalesce driven by cell-cell interactions (Day 2-3). Afterward, cell aggregates acquire a nearly perfect spherical shape (Day 3-5), but individual cells remain identifiable. In the final phase, past Day 5 of culture, cell aggregates mature and form solid spheroids coated with an ECM protein layer appearing as a smooth surface; individual cells are no longer recognizable. After that, no significant change in cellular morphology or spheroid size was observed.

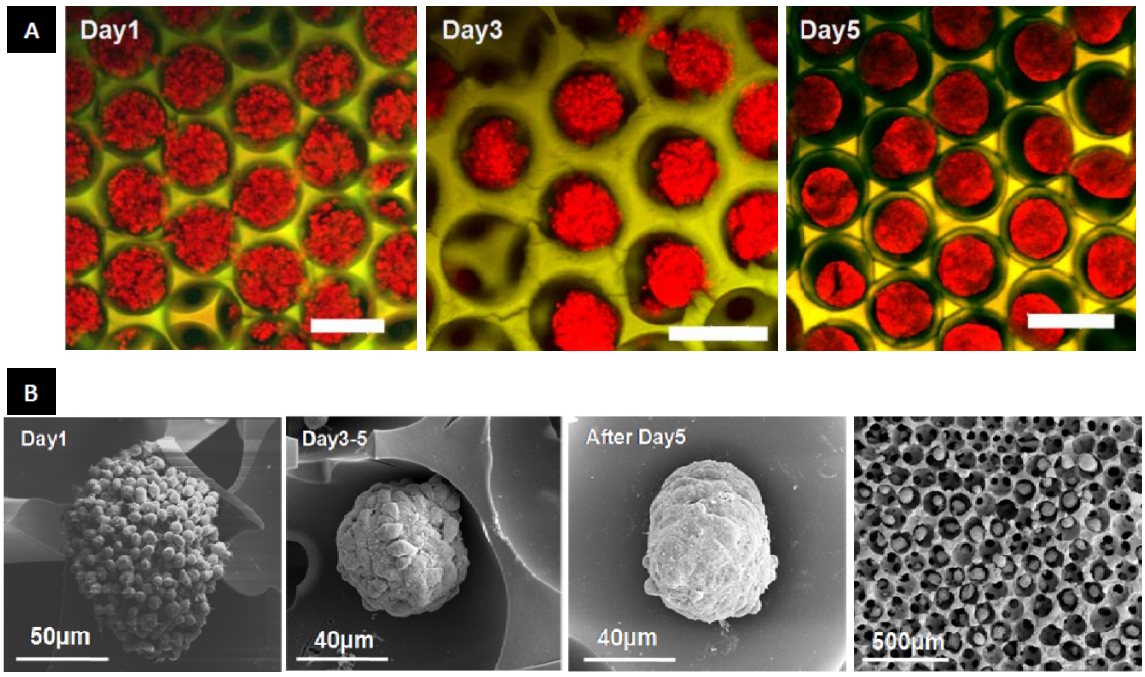

Figure 3.2 Characterization of the spheroid formation process. (A) Three dimensionally reconstructed confocal images of HepG2 spheroid formation in hydrogel ICC scaffolds on Day 1, Day 3 and Day 5 culture (Scale bar is 200µm). **(B)** SEM images of different stages of spheroids and large scale image of mature spheroids in an ICC scaffold. Individual cells aggregate and the surface morphology gradually changes. Once they form solid spheroids, it becomes hard to distinguish individual cells in the spheroid.

Once spheroids develop, all the cells remain within the pore because the diameters of spheroids become larger than the channel size. (Figure. 3.3) Such "ship-in-a-bottle" effect is quite convenient for *in situ* confocal imaging of spheroid because the transparent matrix restricts spheroid mobility and accurately indexes their position, which is quite important for understanding spatio-temporal dynamic processes of intra and inter-cellular interactions during organized spheroid formation. In addition, it can significantly improve the quality of 3D spheroid-based assay results by keeping the total amount of cells constant. At the same time, the proximity of hundreds of such spheroids to each other and their interconnectivity via ICC channels is a significant step toward simulation of actual liver tissue where functional unit of liver tissues i.e. liver lobules are connected

by a network of blood vessels[10]. Greater similarity of responses than those in 2D and some other spheroid cultures to liver tissue should be expected.

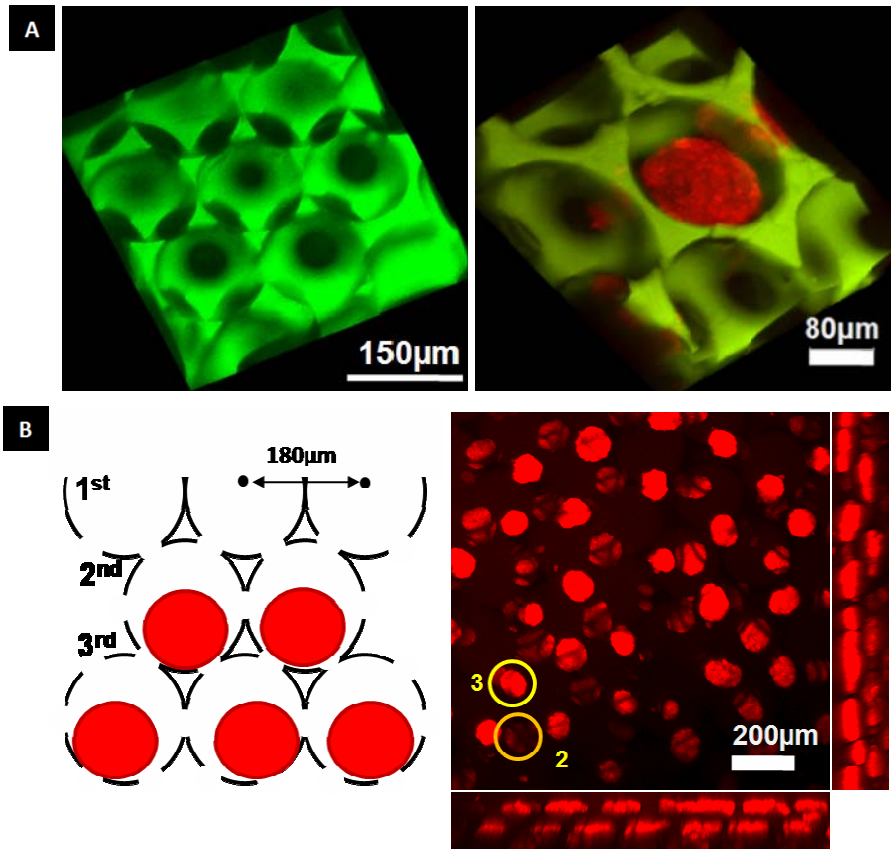

Figure 3.3 HepG2 spheroids entrapped in ICC pores (ship-in-a-bottle effect). (A) 3D reconstructed confocal microscopic images of ICC scaffolds and mature spheroids entrapped in an ICC pore. Fluorescent monomer was used to visualize transparent hydrogel scaffold. **(B)** (Left) Geometrical model of ICC scaffold and entrapped spheroids; spheroids formed on 2nd and 3rd tiers of ICC scaffold can stay in the pore while having sufficient empty space for mass transport. (Right) 3D stacked confocal image of 250μm in depth from top and cross-section views. Numbers 3 and 2 represent spheroids forming in a 3rd and 2nd layer of ICC pore, respectively. HepG2 cells were prestained before seeding.

3.3.3. Spheroid characterization

Cell viability in the exterior and, most importantly, interior parts of mature spheroids were characterized by live-dead staining and observation of cell behavior. Fluorescence confocal microscopy revealed excellent viability of HepG2 cells within the

penetration depth of the stains (22.6±3.4μm); however, no fluorescent signal was detected in the center of spheroids for either the live or dead stains. Since effective diffusion coefficient of dyes in tissue is fairly low ca. 10^{-11} m^2/s[195], there is a limited permeation of reagents inside the cell cluster. Indeed this phenomenon suggested a new challenge in 3D cultures because imaging was restricted though used scaffolding material was transparent. This issue can be temporarily solved by labeling cells before engineering. For example, when scaffolds were seeded with pre-stained cells, it was possible to obtain optical images in the middle of the spheroids through the ICC matrix with excellent homogeneity of fluorescent intensity. (Figure 3.4) Under these conditions, real-time visualization of spheroids at different depths and specific locations[213] would be possible.

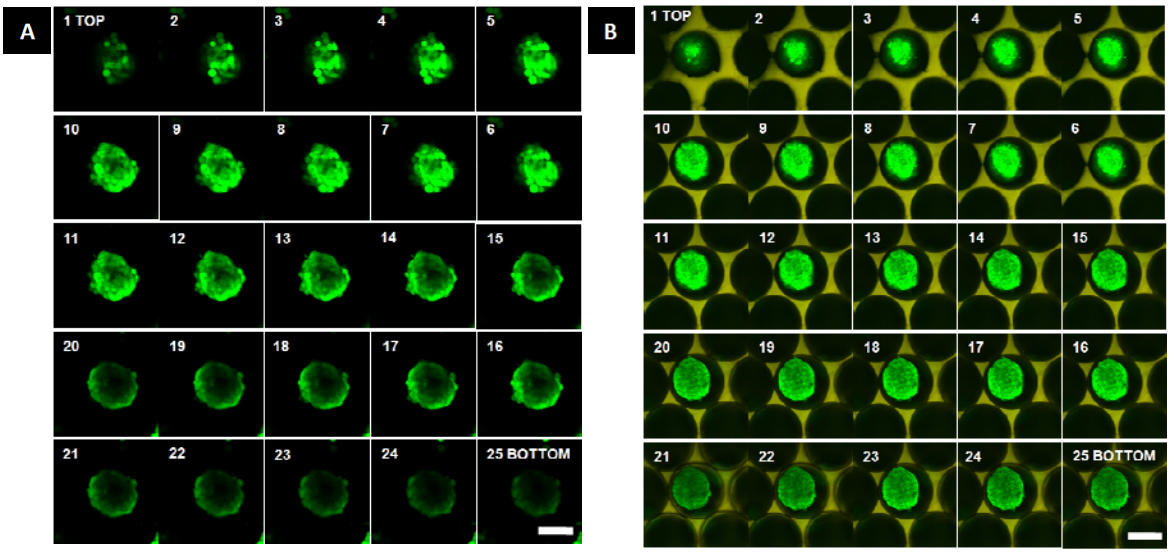

Figure 3.4 Comparison of confocal slicing of single spheroid between post- and pre-staining. **(A)** Cells in a spheroid were stained right before confocal imaging. The center of spheroid appeared as dark due to the diffusion limit of dye molecules. **(B)** Cells were stained before spheroid formation. The cells residing at the center of the spheroid can be imaged and they showed homogeneous fluorescent intensity in the same Z-plane. (Z=75μm and the scale bar is 80μm)

The cell viability at the center of spheroids was also directly confirmed by transferring individual spheroids to a 2D tissue culture plate where they disassembled and fully spread in a few days. (Figure 3.5) The cells residing in the inner part of spheroid are not only alive[217], but also retain capability to migrate and repopulate.

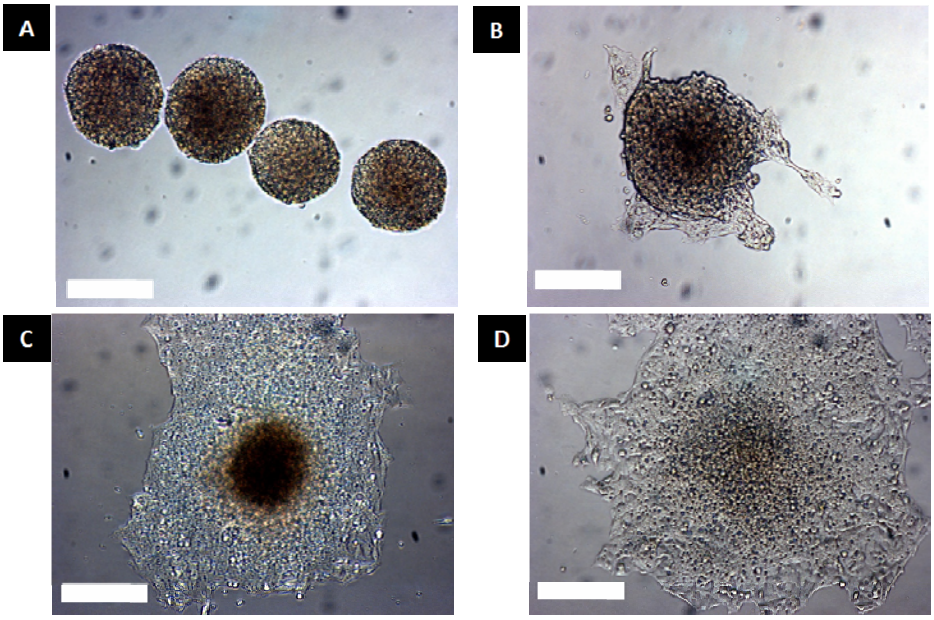

Figure 3.5 Direct confirmation of cell viability in spheroid culture. **(A)** After 7 days of culture, several spheroids formed on the top tier of ICC pores not completely entrapped in ICC pores were released out from the scaffold on purpose. **(B)** Released spheroids started to interact with the surface of a 2D tissue culture plate. **(C)** After 24 hours of culture, the spheroid largely spread and densely packed cells at the center of the spheroid appeared darker compared to the spread cells growing on the 2D culture substrate. **(D)** After 2-3 days of culture, the spheroid was entirely disassembled and the spreading area became larger. (Scale bar is 200μm)

To obtain more detailed information about the internal structure of spheroids, the mature spheroids were histologically sectioned and stained by H&E. One can see that the interior is fully occupied by densely packed cells and a distinct membrane of ECM protein surrounds the outermost region of spheroids. (Figure 3.6A) This ECM layer and tight cell-cell junctions slow down the diffusion of the dye/drug/nutrient molecule into

the spheroid, which is the obvious difference compared to 2D culture and is important for understanding the mechanisms drug delivery, metabolism and hypoxia.[196, 218]

In addition, a continuous and extensive network of channels exists inside the spheroid. Most of these channels open to the outer fluid through pores on the surface of the spheroid which frequently appeared in SEM imaging. (Figure 3.6B) These conduits are homologous to bile canaliculi structures visualized in *in vivo* liver tissues. The diameter of the channels and openings in spheroids prepared in hydrogel ICC scaffolds (2-3µm) coincides very well with reported dimensions of bile canaliculi, 1-3µm diameter.[219] Overall, the diffusion conditions and auxiliary self-organization of cells in spheroids provide a more adequate description of the actual tissue than 2D cultures.

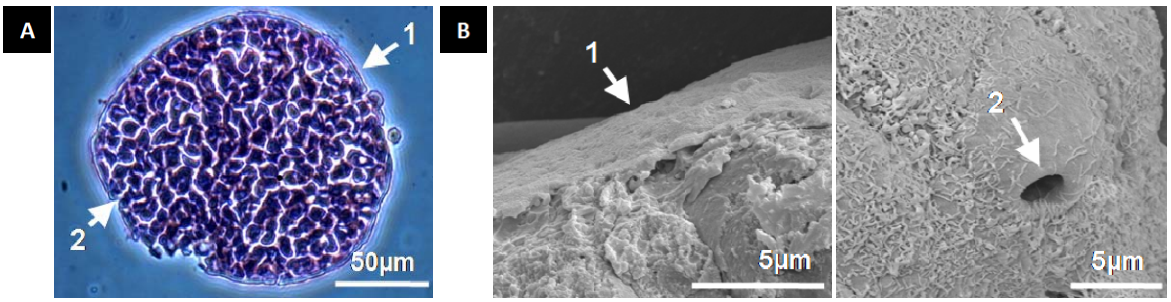

Figure 3.6 Single spheroid characterizations. **(A)** Histologically sectioned and H&E stained spheroid after 7 days of culture. The surface of spheroid is covered by a thin ECM layer (Arrow 1). There is an extensive network of channels inside spheroids. Arrow 2 indicates the opening pores of the channels on the surface of spheroids. **(B)** SEM images confirm ECM layer (left) and the opening of the channel (right) from mature spheroids. To characterize the ECM layer, the spheroid was sliced using a vibratome.

3.3.4. Spheroid size control corresponding to ICC pore diameters

Preparation of uniformly sized spheroids is critical for the consistent evaluation of the relationships between cell cluster diameter and biological activity. Homogeneous spheroid size is also important because diffusion limitations vary with spheroid dimensions that might or might not affect the target assays. In this respect, the

possibilities to control the size of spheroids in ICC scaffolds and investigate these relationships represent an interesting opportunity for fundamental cell biology. To address whether the pore sizes can control spheroid diameter with desirable precision, we prepared five different ICC scaffolds (D=50, 100, 140, 170 and 200μm groups), and seeded the same number of cells. (Figure 3.7)

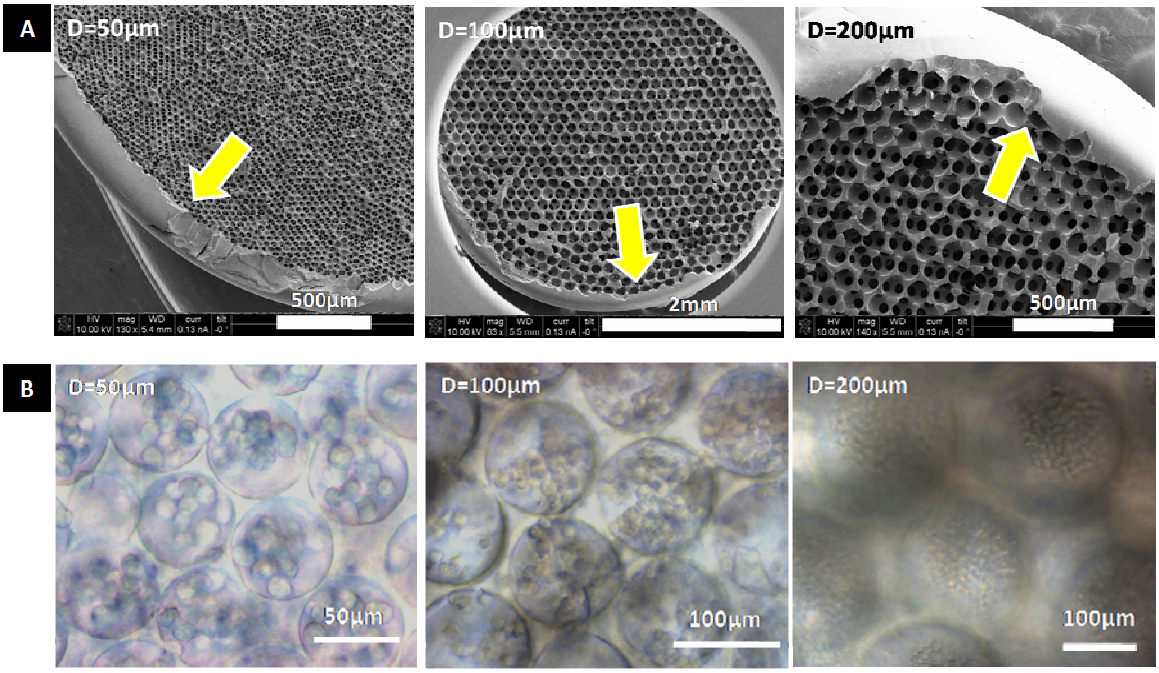

Figure 3.7 Different pore size of pocket ICC scaffolds and initial cell seeding profile (A) 50, 100 and 200μm pore diameters of pocket ICC scaffolds. Arrows indicate pocket wall in each scaffold. **(B)** Initial cell seeding profile of three different pore sizes. Image analysis results revealed that a single cell has a diameter of 10-15μm, and approximately 8 ± 4, 37 ± 6, and 160 ± 15 cells were seeded in each pores of ICC scaffolds having 50, 100, and 200μm pore dimensions, respectively.

At the stage of spheroid maturity (5 days of culture), the dependence of spheroid diameter and their size uniformity on the ICC pore size was evaluated. We observed the formation of 46.5±8.1, 87.8±16.0, 120.9±14.4, 141.8±19.5, and 151.6±20.0 μm spheroids in scaffolds with 59.5±1.9, 108.2±3.9, 154.8±4.0, 183.5±7.2, and 218.6±6.1 μm pores, respectively**.** Indeed, a fine level of control ($P<0.0005$) over the diameter can be exerted.

Typically, the spheroid diameters reached around 77% of pore diameters or 50% of a pore volume. (Figure 3.8) When the ICC pore becomes too large, i.e. above 170µm, other mechanisms, such as nutrient delivery to the interior cells, apparently begin to play a greater role than space restriction and the spheroid diameter becomes less dependent on ICC pore size remaining fairly uniform.

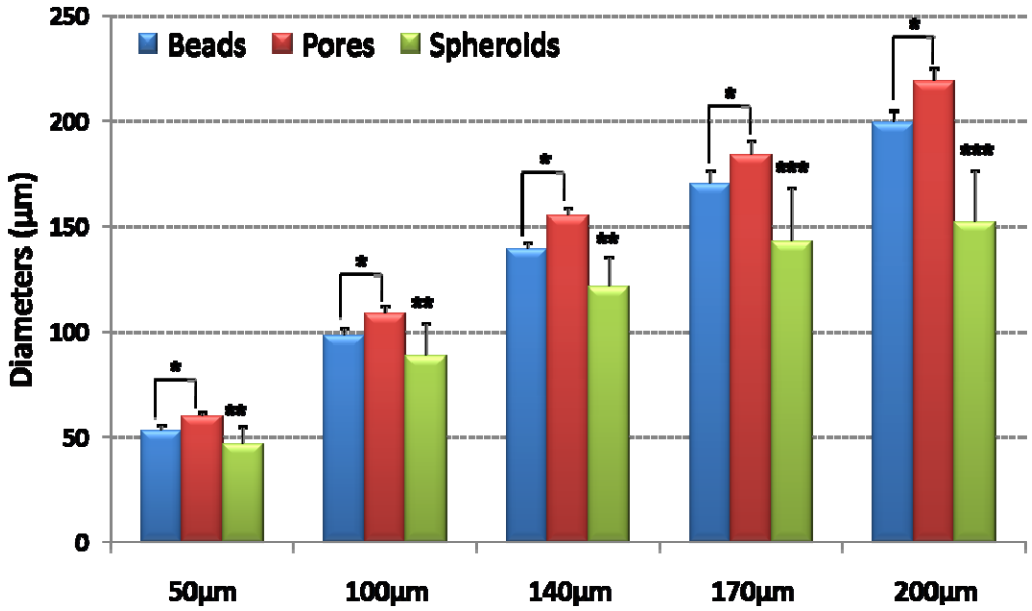

Figure 3.8 HepG2 Spheroid size control corresponding to pore dimensions of ICC scaffolds. The pore size is normally 10% larger than the bead dimension. Each group has significantly different pore sizes (n=50, * $p<0.0005$). Spheroid diameters reach approximately 78% of pore size except in the 200µm group (69.4%). Except in the 170µm and 200µm groups (*** $p>0.01$), each group has a significantly different sizes of spheroids. (** $p<0.0005$) (Five scaffolds were used in each group and 74-86 spheroid sizes were measured.)

3.3.5. Spheroid size dependent liver specific functions

Having the set of scaffolds with different pore diameters as a tool for systematic study, the dependence of albumin secretion rate and induced CYP450 activity were investigated from cell cluster size for three different sizes of spheroid cultures, i.e. 50, 100 and 200µm groups, and compared the results to a typical 2D culture. As shown in

Figure 3.9A, the initial albumin secretion rate in all 3D groups was significantly reduced compared to the 2D case, but it rapidly recovered over the culture period. On the other hand, there was only moderate increase in 2D substrates over the cell culture period. The 50μm group showed the fastest increment and became closer to the 2D culture level only after 2~3 days of culture. The albumin secretion rate in 100 and 200μm groups became comparable to the 2D case after one week of culture, and there was no significant difference between the two groups. Three points should be made from the comparison of albumin secretion rates in the 2D, 50, 100, and 200μm cultures: (i) Contrary to what might be inferred from previous studies[219, 220], all experimental groups revealed the general trend that at least the initial albumin secretion become initially suppressed rather than augmented in 3D cultures. In fact, this is not surprising because most of the cellular energy in Day 1-3 is probably consumed by forming multicellular spheroids and tissue infrastructure inside them, such as bile canaliculi. Gradual enhancement of albumin secretion following spheroid formation infers that cellular protein synthesis capability is recovered once they form stable spheroids; (ii) Smaller spheroids take less time to form, and hence, one can observe substantially steeper growth of albumin secretion (Day 1-3) in the 50μm group compared to the 100 and 200μm groups; (iii) Production of albumin exhibited only moderate, if any, rise in 2D culture. Fast rise and plateau after 3 days was observed in the 50μm group, and a continuous increase over a period of 8 days was seen in the 100 and 200μm groups. This suggests that phenotypic change gradually occurs in spheroid culture, whereas the same cellular phenotype maintains in 2D culture.[221] Similarity of albumin production rate after should not be used as an indication of phenotype identity.

Induced CYP450 activity was measured by an EROD assay after 5 days of culture. (Figure 3.9B) Since a significant amount of transformed substrate remained in cell/scaffold lysate solution of 3D culture, not only sample media, but also hydrogel matrices and spheroids were characterized. Similar to the albumin secretion results, EROD activity in 2D culture was higher than in all 3D cultures, and the 50µm group showed superior CYP450 induction to the 100 and 200µm groups. Considering the data on albumin secretion and mitochondrial activity in spheroids[218], the trends in EROD assays should be interpreted in relation to metabolic activity of cells rather than direct consequence of culture formats. The key parameter here should be the surface area to volume ratio, which increases for smaller spheroids. The percentage of cells inside the spheroid with a characteristically low metabolic rate increases for larger spheroid diameters.

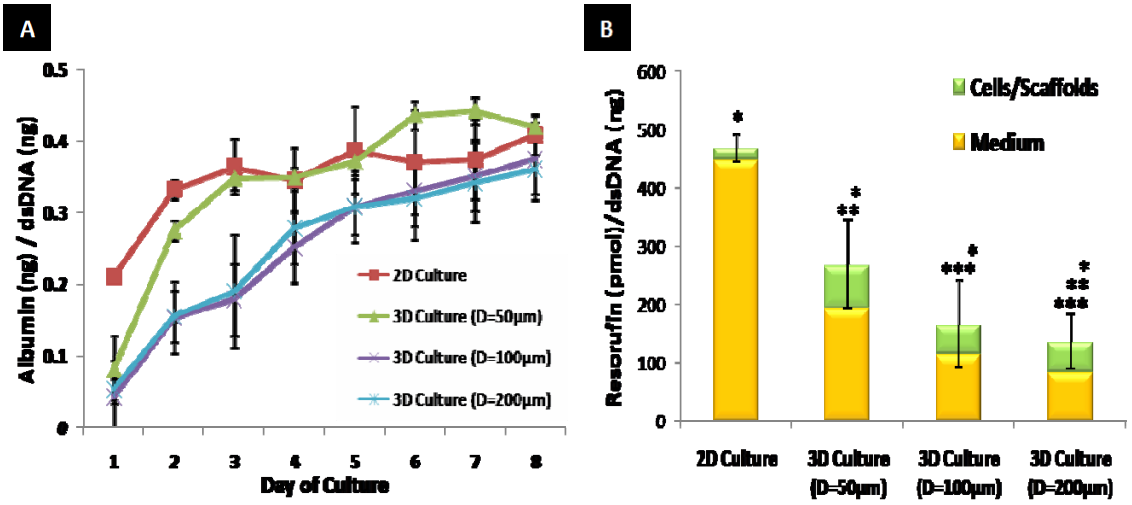

Figure 3.9 Testing liver tissue specific functions from HepG2 spheroid and 2D culture. (A) Normalized albumin secretion rate by total dsDNA content in a 24 hours period. **(B)** Normalized induced CYP450 assay result with total dsDNA content after 5 days of culture. Each bar is composed of EROD activity from the culture medium (yellow) and the solution of homogenized cells/scaffolds (green). The remaining portion of resorufin within the cells in 2D culture was negligible (4%), while a substantial amount of resorufin remained in the cells and the hydrogel matrix in 3D cultures (~30%). (* Comparison between 2D culture and all 3D cultures ($P<0.005$), ** between 50µm and 200µm group ($P<0.05$), *** between 100µm and 200µm group ($P>0.05$), representative data from three independent experiments, N=4~8)

Discussing cell metabolism in spheroids, one also needs to point out that diffusivity of oxygen is quite high with effective diffusion coefficients of 3.4×10^{-10} m^2/s[195]. The diffusion limit of oxygen in tissues is around 150-200μm[222], so cells within spheroids of a diameter up to 300-400μm are not expected to suffer from hypoxia, while the diameters of the spheroids used here are 48-150μm. Hypoxia cannot be the reason for the reduction of metabolic rate. The underlying reasons behind the trend of reduction of cellular activity in 3D arrangements can be several: (i) Extensive cell-cell contacts in clusters can signal the cells to reduce metabolic rate; (ii) The diffusion of albumin, EROD, and other reporting molecules to and from the internal cells has a greater barrier than that in the 2D cell cultures; (iii) Surface cells dominating in small clusters and 2D cultures may be more active because they have better conditions for the delivery of nutrients and removal of metabolites.

Interestingly, there is an evident contradiction between the data reported here and those published previously which typically show greater activity in spheroids than in "flat" cells[223-225]. Analysis of this discrepancy is significant in understanding cell biology and the proper selection of cell culture conditions for different tissue modeling tasks. Two potential factors are suspected. The first one is the absence of shear forces that have been frequently utilized in spheroid culture because the flux conditions stimulate cell aggregation.[206, 207, 224, 225] Presence or absence of shear force in 3D conditions could be the key factors determining metabolic rate of cells. Besides improving diffusion of oxygen and nutrients, mechanical stimulation by shear stress plays an important role in maintaining a proliferative state of hepatic spheroids and enhancing liver specific functionality. For example, Shvartsman et al. demonstrated significantly augmented

CYP450 activity of hepatic spheroids in perfusion culture condition.[225] Also Chang et al. reported that HepG2 spheroids cultured within a rotating wall vessel bioreactor exhibited continuous proliferation and substantially up-regulated metabolic activities.[224]

In addition to shear forces, a topological factor could account for the lower metabolic activity since ICC matrices, unlike 2D and other 3D systems have high volume density of cells and interfaces. On one hand, this brings them closer to real human liver. On the other hand, this can induce strong contact inhibition of cells, which cause a substantial portion of cells to become quiescent in spheroids.[226] Quiescent tumor spheroids can potentially be an excellent model for understanding tumor dormancy, as well as their repopulating and metastatic mechanisms.[227]

3.4. Summary

In summary, uniformly sized pores in ICC hydrogel scaffolds afford a high yield production of controlled size spheroids in standard 96 well-plates. Transparent hydrogel matrix and ship-in-bottle effect also allows for convenient monitoring of cell processes by traditional optical techniques. Different developmental stages of 46.5–151.6μm spheroids from HepG2 hepatocytes with vivid morphological similarities to liver tissue (bile canaliculi) were observed. A high yield of spheroids in well-interconnected pores is beneficial to derive tissue level biological responses without tissue vascularization. Liver specific function was demonstrated to be strongly dependent on the diameter of spheroid.

Since the aggregation of cells into clusters is a universal biological process, these findings and scaffolds can be applied to many other relevant cell types. Along with many

advantages expected of *ex vivo* replicas of human organs, this system also allows one to identify the specific challenges of 3D cell cultures and avoid fundamental experimental mistakes and conclusions. Most importantly the presented system will contribute to the development of various physiological and pathophysiological 3D tissue models which can be served as a valuable tool for understanding tissue level biology and *in vitro* drug testing application.

CHAPTER IV

IN VITRO TOXICITY TESTING OF NANOPARTICLES

4.1. Introduction

In this chapter, the standardized 3D liver tissue spheroid culture model is applied to an *in vitro* toxicity testing platform. Instead of drug molecules, nanoparticles (NPs) were selected as testing compounds because it is getting important to access and predict their toxic effects in the body. Despite providing valuable information, *in vitro* 2D cell culture models do not accurately predict *in vivo* toxicity and other biological effects of NPs due to the absence of key physiological processes[212], such as transport of NPs through cell layers when they are brought in contact with the tissues. Also, essential effects of NPs and other substances are neglected with respect to cellular functions which are strongly dependent on 3D organization. For example, the enhanced specific protein secreting function of granular epithelial cells can only be observed when they form a three dimensionally organized acinus structure.[29] As an additional piece of evidence substantiating the significance of expanding cell toxicity assays from 2D to 3D cultures, one also must mention that it has become increasingly apparent that there is a large discrepancy in toxicity results depending on whether *in vitro* 2D cell culture or animal models were used.[228] For instance, recent studies on toxicity testing of quantom

dots[229], magnetic NPs[230], CNTs[231] and fullerenes[232] using *in vitro* 2D cell culture showed high cytotoxic effects. However, when they were tested in animal models, no adverse effects were observed.[233-236] (Table 4.1)

As shown in Chapter 3, multicellular spheroid culture is expected to be the most effective 3D culture model. Therefore, the toxicity testing based on the spheroid culture would deliver more physiologically relevant toxicological information about NPs that might be quite different from the current cellular level cytotoxicity. Resultantly, it can potentially enhance the predictive power of current *in vitro* toxicity testing for estimating *in vivo* toxicity.

Table4.1 Discrepancy between *in vitro* and *in vivo* NPs toxicity testing

	Cytotoxicity (*In vitro* 2D)	**Animal Testing** (*In vivo*)
CNTs	"Our work clearly indicated that these materials are toxic…" ***Nano Lett. 6, 1121 (2006)***	"No toxic side effect of SWNTs to mice was observed in…" ***PNAS, (2) 105, 1410 (2008)***
Fullerenes	"This work demonstrates both a strategy for enhancing the toxicity of fullerenes…" ***Nano Lett. 4, 1881 (2004)***	"The results demonstrated little or no difference in lung toxicity effects …" ***Nano Let. 7, 2399 (2007)***
Magnetic NPs	"Exposure to increasing concentrations of anionic magnetic NPs results in a dose-dependent diminishing ability of PC12 cells.." ***Biomaterials, 28, 2572 (2007)***	"…magnetic nanoparticles of 50-nm size did not cause apparent toxicity under the experimental conditions of this study..." ***Toxicol Sci, 89, 338 (2006)***
Quantom Dots	"…CdTe QDs induce cell death via mechanisms involving both Cd^{2+} and ROS …" ***Langmuir, 4, 1974 (2007)***	"Few signs of functional toxicity or clinical (urinary or blood) changes were noted…" ***J of Nanosci. & Nanotec. 7, 497 (2007)***

Methods for the toxicity testing of NPs are basically the same as the techniques used in modern drug development; however, the toxic mechanism of NPs can be more diverse than that of drug compounds. NPs can be indiscriminately transported into cells due to their comparable dimension to biological macromolecules.[237] Fiber-shaped NPs

such as nanowires, nanotubes and nanofibers have a high probability for the penetration of cell membrane and tissue layers, as has been reported for asbestos.[238] Decomposed NPs generate free radical species or toxic ions which can injure plasma membrane functions by reducing membrane integrity or impairing ion channel transport.[239] Additionally, there are potentially more unrecognized harmful effects of NPs considering the great diversity of engineered NPs in chemical composition, size, shape, charge, coating, solubility, and so on.[240-242] Equally, there might be some potentially unrecognized beneficial effects related to the same factors. (Figure 4.1) Until now ***all*** of the *in vitro* NP toxicity testing has been performed using 2D cell cultures[243], and it will be very important to demonstrate a suitable 3D cell model for NPs and compare the results with 2D cell cultures.

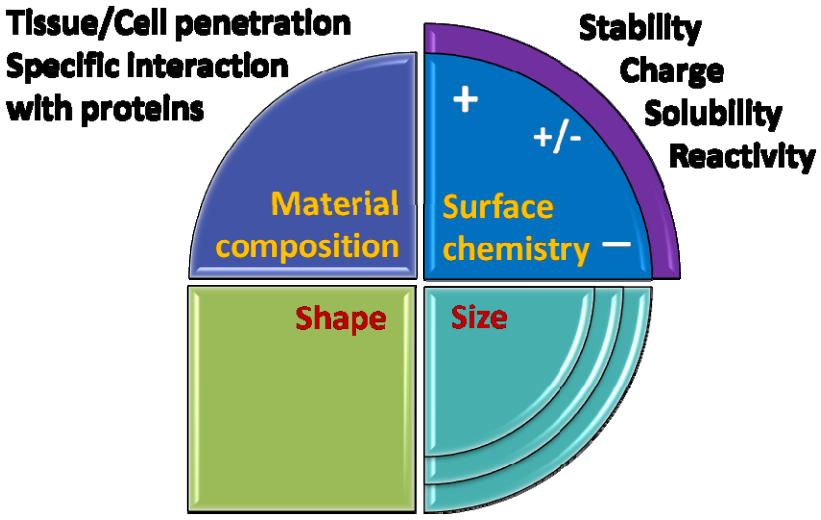

Figure 4.1 Various routes of nanoparticle induced toxicity

The established ICC-spheroid culture system exhibits multiple advantages for NP toxicity testing. For instance, transparent hydrogel matrix allowed easy characterization of optical based assays. In addition, by utilizing standard micro well-plates, it can be

readily accessible to existing hardware such as a microplate reader. Consequently, the spheroid culture system permits the systematic and reproducible characterization of toxic effects of NPs on liver tissue which is one of major tissues for NP accumulation. The toxic effects of CdTe and Au NPs were tested using a number of different approaches, including morphology, membrane integrity, metabolic activity and cell death mechanism; and a comparison was made with conventional 2D culture-based cytotoxicity.

4.2. Materials and Methods

4.2.1. Au and CdTe nanoparticle synthesis

Au nanoparticle synthesis

Au NPs having two different stabilizers were synthesized following the previously reported method.[244] Briefly, a 20ml of aqueous solution containing $2.5x10^{-4}$M $HAuCl_4$ and $2.5x10^{-4}$M trisodium citrate was mixed with 0.6ml of ice-cold 0.1M $NaBH_4$ solution while stirring. In a few minutes, Citrate-Au NPs were prepared with a diameter of 3.5±0.7 nm. A 7.5ml of aqueous solution containing $2.5x10^{-4}$M $HAuCl_4$ and 0.08 M cetyltrumethylammonium bromide (CTAB) was mixed with 0.05ml of 0.1M of ascorbic acid solution. CTAB-Au NPs with a diameter of 5.5±0.6 nm were prepared by adding 2.5ml of Citrate-Au solution while stirring.

CdTe nanoparticle synthesis

L-cysteine stabilized CdTe NPs were prepared according to the literature.[245, 246] Briefly, 2.35mM of $Cd(ClO_4)_2 \cdot H_2O$ and 5.7mM of *L*-cysteine were dissolved in 125ml of deionized water; the pH is rapidly adjusted to 11 using 1M NaOH and placed in a three-necked flask and degassed with N_2. H_2Te gas is introduced to this solution by the

reaction of 0.46mM Al_2Te_3 and 20ml of 0.5M H_2SO_4 in a separate three-necked flask. The solution is nitrogen-purged for an additional 30minutes, at which time the CdTe NP solution is refluxed to achieve the desired NP size. The NPs were observed under atomic force microscopy (AFM) (Digital Instruments NanoScope III) and analyzed using NanoScope ® III software tools. Fluorspectroscopic measurements were performed using a Jobin Yvon Horiba FluoroMax-3.

4.2.2. Spheroid culture and nanoparticle treatment

ICC hydrogel scaffolds were prepared using glass beads (D=156.85±8.4μm). Dried state ICC scaffolds were rehydrated in PBS solution and then sterilized by immersion in 70% ethanol for 15 min under UV light. The sterilized scaffolds were washed with PBS three times and transferred into a non-tissue culture treated 48 well-plate (Corning, NY). Human hepatocellular carcinoma (HepG2) spheroid arrays were prepared following the protocol in Chapter 3. Briefly, a 20μl of cell suspension ($5x10^5$ cells) was dropped on top of an ICC scaffold and then 1ml of culture media was gently added into the well. For 2D culture, $1x10^5$ cells were seeded in each well of a 12 well-plate containing 1ml of culture media. A half volume of media (0.5ml) was changed daily both 2D and 3D cultures for 5 days.

On Day 6 of culture, media was changed with 10μg/ml CdTe and 98.5μg/ml Au NP solutions in William's E medium. A control culture was maintained with only William's E medium. After 12 and 24 hours (also some interval time points) incubation, the NPs exposure and control cultures were characterized.

4.2.3. Morphological characterizations

Optical and Confocal Microscopes

Cell morphology was observed using an inverted microscope with 10X and 20X objectives (Nikon TS100) and a digital camera with imaging software. Cell viability was observed after staining Live/Dead dyes under confocal microscope (Leica SP2). Specifically, NPs exposure and control culture were incubated with 2μM calcein and 4μM ethidium homodimer-1 for 40 minutes at 37°C. Under a laser excitation of 488nm, live cells were imaged as green using a 510-540 nm emission filter, and dead cells stained by ethidium homodimer-1 were imaged as red using a 600-630 nm emission filter.

Scanning Electron Microscope

A SEM was used to characterize cellular morphology. Cells in sample scaffolds and on 2D glass slides were fixed overnight with 2.5% glutaraldehyde solution. The samples were then dehydrated through a series of ethanol solution concentrations of 50, 70, 90, 95 and 100%, and then freeze dried. After 180 sec gold sputtering, the samples were imaged using a FEI Nova Nanolab SEM.

4.2.4. Toxicological assays

LDH Assay

Lactate dehydrogenase leakage from dead cells was analyzed using a LDH assay kit (Promega, WI). Diluted supernatant of 50μL was mixed with 50μL of reagent and incubated for 30 minutes at room temperature. A 50μL of stop solution was then added, and absorbance at 490nm was measured using a microplate reader (BioTek, VT)

MTT Assay

Mitochondria activity was quantified using a MTT assay kit (ATCC, VA). The medium was aspirated and 500µL of fresh serum-free medium was added with 50µL of MTT reagent. After 3 hours incubation, 500µl of detergent solution was added and incubated for 2 hours more. The scaffolds and cell lyses solutions were transferred into 1.5ml centrifuge tubes. Scaffolds were completely destroyed by using forceps and further sonication. After centrifugation at 1,000rpm for 5 minutes, 200µl of supernatant solution was collected, and then the absorbance was measured at 590nm (sample) and 630nm (reference). The difference in activity between normal and NPs exposure cultures was used as a toxicity indicator. All measurements were performed in triplicate, and six independent experiments were carried out.

Apoptosis Assay

Caspase activity was measured using a Caspase 3/7 assay kit (Promega). After treatment of CdTe NPs, the culture media was completely removed for the LDH assay. The scaffolds were transferred into a 1.5ml centrifuge tube and 250µl of 1x cell lyses buffer solution (Promega) was added. The scaffolds were then crushed into small pieces with a micro centrifuge sample pestal and sonicated for 3-5 sec. In 2D cultures, 250µl of 1x cell lyses buffer was added. Then 250µl of Caspase 3/7 assay reagent was added to each sample solution and incubated for 2 hours at room temperature. To maintain the same sample preparation conditions, the cell lysate in 2D cultures were transferred into 1.5ml centrifuge tubes and briefly sonicated to make a homogeneous dispersion. The sample-containing tubes were centrifuged at 1,000rpm for 5 minutes to precipitate scaffolds and cell debris. A 200µl of supernatant solution was collected in a white-wall

luminescence plate. Luminescent intensity was measured using a microplate reader with 10 seconds integration time.

4.3. Results and Discussion

4.3.1. Standardized hepatic spheroid culture model

An absolute spheroid size suitable for toxicity testing and other assays has not been identified. Considering the previously reported data[197, 247], spheroid diameters were aimed to be around 100µm so as not to induce hypoxic culture conditions while recovering tissue level physiological properties. The spheroid diameters are dependent upon pore dimensions, which can be easily regulated by changing the size of the microspheres in the colloidal crystal template. Here glass beads with a diameter of 156 ± 8.4µm were used for preparing colloidal crystals. Final ICC scaffolds have 174.6 ± 10µm diameter pores, approximately 10% larger than the template bead sizes due to swelling of the hydrogel matrix, and 49.6 ± 7µm diameter interconnected channels, approximately 30% of pore diameters. (Figure 4.2)

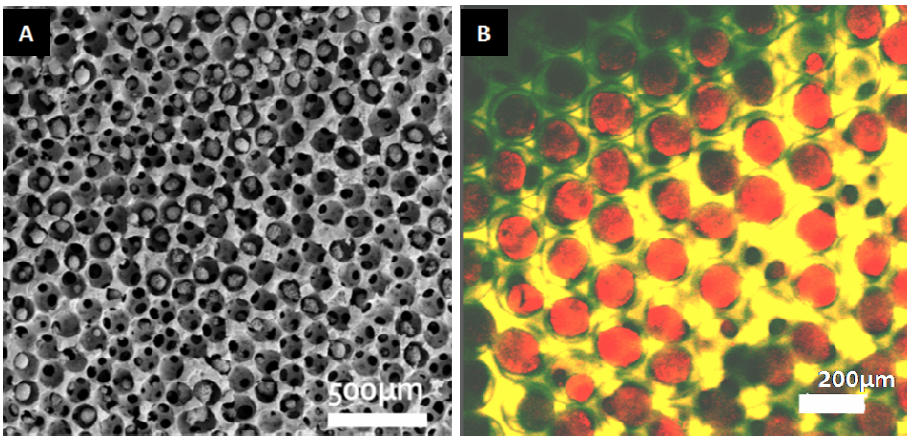

Figure 4.2 HepG2 spheroid (D~100 µm) arrays prepared in ICC hydrogel scaffolds. (A) SEM and **(B)** Confocal images

4.3.2. Morphological evaluation after nanoparticle exposure

The exact mechanism of semiconductor NP (e.g., CdTe and CdSe) induced toxicity is unclear, however, it has been identified that the most important aspect is the stability of NPs both under physiological conditions, i.e. intracellular and *in vivo*, as well as during synthesis and storage since they are susceptible to photolysis and oxidation. Released free cadmium and reactive oxygen species impair cell function and eventually kill the cells.[229, 248] For example, Derfus et al. demonstrated that decreased photostability of CdSe NPs under exposure to ultraviolet light caused liberation of free Cd^{2+}, which in turn enhanced cytotoxicity.[249] Kirchner et al. reported that the core-shell structure of CdSe/ZnS significantly reduced the cytotoxicity of CdSe NPs by protecting the core from oxidation and preventing it from leaching into the surrounding solution.[250] The cytotoxicity of semiconductor NPs also differs depending on their size[233, 248] and stabilizer chemistry/surface modification.[229, 251] On the other hand, gold NPs have excellent stability and major factors inducing toxic effect are shape, size and stabilizer chemistry.[252, 253]

In this study unmodified *L*-cysteine-stabilized CdTe NPs were intentionally used which are unstable and quite toxic in order to highlight the different cellular toxic effects between 2D and 3D spheroid cultures. The CdTe NPs have a photoluminescence peak of 577nm and an average diameter of 2.9±1.0 nm. (Figure 4.3) The CdTe NP concentration was constantly maintained at 10μg/ml while varying the exposure time up to 24 hours.

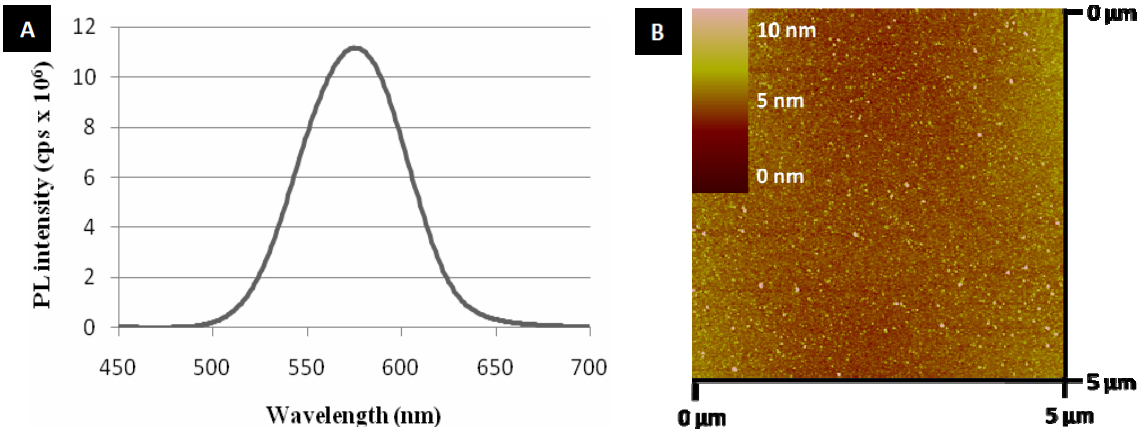

Figure 4.3 *L*-cysteine stabilized CdTe NPs synthesis. (A) Emission PL spectra, peak at 577nm, **(B)** AFM image, 2.9±1.0 nm of average diameter

Citrated-stabilized (D = 3.5 ± 0.7 nm) and CTAB–stabilized (D = 5.5 ± 0.6 nm) spherical Au NPs were also prepared. Their concentration and exposure time were maintained at 98.5µg/ml and 24 hours, respectively. All toxicity testing was performed with freshly synthesized NPs, less than a week after preparation, but increased toxic effect of CdTe NPs over time was observed in the 2D culture due to decomposition (Data not shown). In addition, to establish comparable testing conditions in both 2D and 3D cultures, the same culture volume (1ml) and a similar number of cells were maintained at the point of toxicity testing. Since the cell proliferation rate in spheroid culture is considerably slower than in 2D culture, five times fewer cells were seeded for 2D cultures ($1x10^5$ cells) than 3D cultures ($5x10^5$ cells). After 5 days of culture, the point at which 3D cultures form solid spheroids and NP exposure began, total cell numbers in both cultures were approximately equal. Additionally, toxicity assay results were normalized with total DNA content.

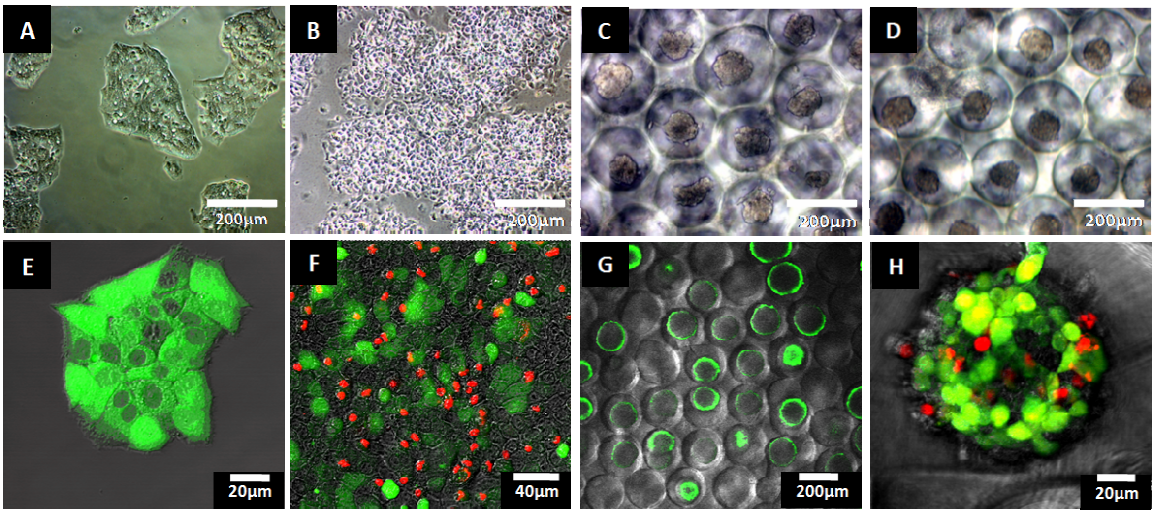

Figure 4.4 Comparison of 2D and 3D culture of HepG2 cells after 12 hours of CdTe NP exposure. (A-D) Optical images of normal **(A)** 2D and **(C)** 3D spheroid cultures. After CdTe NP introduction, **(B)** 2D culture showed a dramatically different morphology, **(D)** while it was hard to distinguish any change in the 3D culture under an optical microscope. **(E-H)** Confocal images of live/dead stained normal **(E)** 2D and **(G)** 3D spheroid cultures; live cells are green and dead cells are red. Most cells in both cultures showed excellent viability. Again after CdTe NP exposure, **(F)** 2D culture revealed that a significant number of cells were dead. **(H)** Although a few cells located on the surface of spheroids were dead, overall the number is much smaller than the 2D culture.

At first, the cellular morphology change was investigated because it is an obvious initial sign of toxic effect. In 2D cell culture, HepG2 cells normally have a flat shape after spreading out on a well-plate while closely attaching to each other. However, their morphology dramatically changed after 12 hours of CdTe exposure. A significant number of shrunk and rounded cells were observed with some partially detached from the well-plate. (Figure 4.4A-B)

In case of Au NPs, as expected, in 2D culture citrate-stabilized Au NPs did not induce toxic effect while CTAB-stabilized Au NPs showed high cytotoxicity. (Figure 4.5) Interestingly toxic effects of CdTe and CTAB-stabilized Au NPs were significantly reduced in 3D spheroid culture. No significant morphological alteration was noticed in spheroid culture except only a slightly rugged spheroid surface. (Figure 4.4C-D)

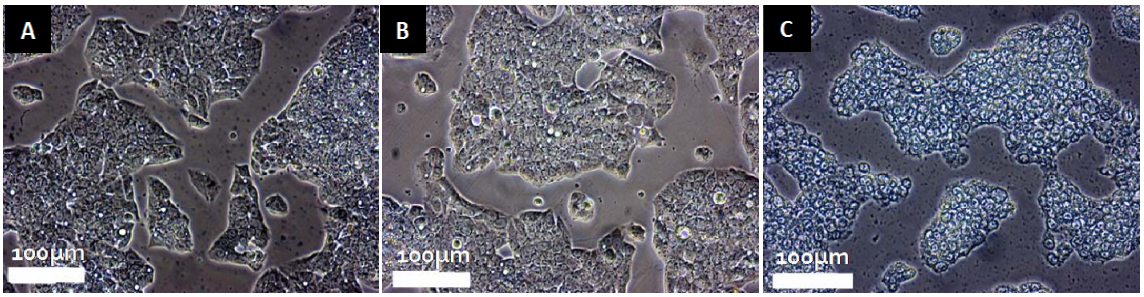

Figure 4.5 Characterization of cellular morphology after 24 hrs Au NP exposure. (A) Control culture, **(B)** Citrate-Au and **(C)** CTAB-Au NPs.

In order to confirm whether the reduced toxic effect is caused by the diffusion limit of toxic molecules within the scaffold or not, a simple diffusion test was performed as dropping a 500µl of rhodamin solution on top of an ICC hydrogel scaffold. The spread of dye molecule was characterized in real time under confocal microscope. Within 5 min strong fluorescent signals were detected from the entire scaffold. (Figure 4.6) This result supports that the diffusion of toxic molecules is not the reason of reduced toxic effects in the 3D spheroid culture.

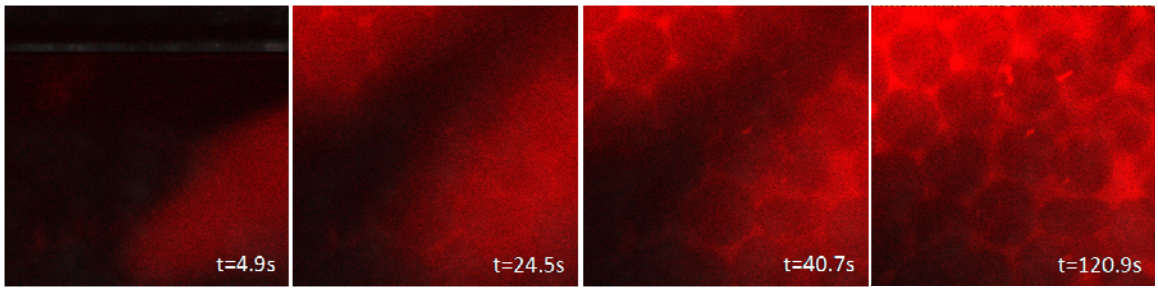

Figure 4.6 Real time characterization of rhodamin diffusion within ICC scaffolds

To distinguish more clearly between live and dead cells, the cells were stained with live-dead assay dyes. In 2D culture, it was apparent that dead cells (red) morphed into a granular shape and fell away from the plate after losing their cell-cell and cell-substrate interactions. (Figure 4.4E-F) Although the spheroid culture did not undergo a

distinct morphological change, a few dead cells were observed on the surface of spheroids with a rugged exterior, as discussed above. There were noticeably fewer dead cells in the spheroid culture than the 2D culture. (Figure 4.4G-H)

Morphological changes were further characterized under a SEM. In normal conditions, individual cells are hard to distinguish in both cultures because they form tight cell-cell junctions covered by a pervasively developed ECM layer. After 12 hours of CdTe NP exposure, dying or dead cells could be distinguished as they were separating from a live cell colony. This phenomenon was more obvious in 2D culture. In spheroid culture, dead cells could be identified as protruding bulbs, but they did not separate from the spheroid. It seemed that cells in a spheroid were tightly packed together and formed intensive junctions with adjoining cells. Thus, dead cells could stay in the spheroid despite losing their cell-cell interactions, and the overall spherical shape could be maintained. (Figure 4.7)

To further examine the toxic effects of CdTe NPs, the exposure time was extended 24 hours. As expected, longer treatment caused severe damage in 2D culture. A significant number of cells were dead and detached from the well-plate. Even cytoskeletons of dead cells were readily identified. (Figure 7A-Right) Similarly, in spheroid culture the surface roughness increased, corresponding to an increase in dead cell bodies. Individual dead cells were easily recognizable but they still remained on the spheroid. In order to observe the inner part of the spheroids, samples fixed in formaldehyde were left for one week to allow partial detachment of the dead cell bodies from the surface of the spheroid. Characterization of the spheroids revealed that the inner cell mass was preserved while the outer layer of cells was severely damaged. (Figure 7B-

Right) CTAB-Au NPs showed similar results to CdTe NPs treated culture. Again no significant morphological change was observed for citrate-Au NPs.

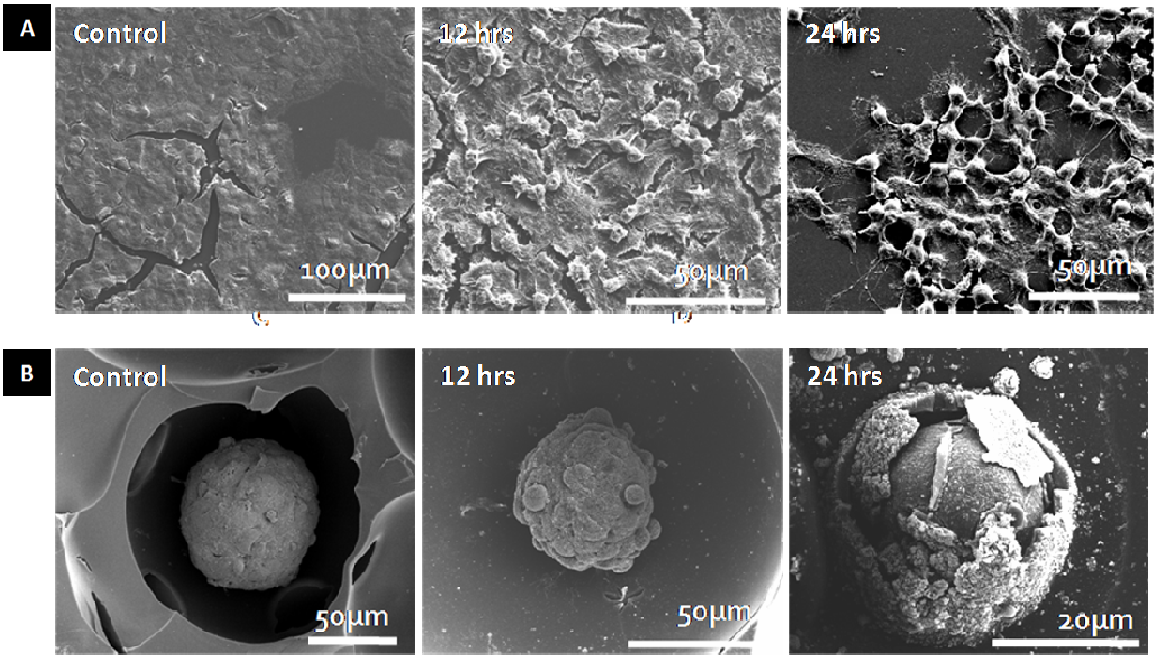

Figure 4.7 SEM images of 2D (A) vs. 3D spheroid (B) cultures before and after CdTe NP exposure. (Left) Typical morphology after 5 days of culture. The surface is very smooth due to tight cell-cell junctions and a well-developed ECM layer, so that it makes hard to distinguish individual cells in both cultures. **(Center)** Representative morphology after 12 hours CdTe NP exposure. Dying cells gradually lose their cell junctions. Shrunken cell bodies detached from the cell colony were easily recognized in 2D culture, while in 3D spheroid culture, dying or dead cells located on the surface were partially dissociated from the spheroid and appeared as protruded blubs. **(Right)** Morphological change after 24 hours CdTe NP exposure. In 2D culture, most cells were dead and considerable number of cells was detached from the substrate. Although cells in spheroid culture were damaged, multilayered structure buffered toxic effects to inner cells. Intact inner cell mass were observed after partially detaching dead cell bodies on the surface of the spheroid by intentionally keeping the formaldehyde fixed culture for one week.

Morphological study results clearly indicate that the degree of toxicity of CdTe and CTAB-Au NPs to the spheroid culture is substantially lower when compared to the 2D culture. The most obvious reason for that is the diffusion of NPs into the spheroid. Densely-packed cells in the spheroid are covered by a well-developed layer of ECM common for all tissues which reduces the penetration of toxicants. Hence, the inner layer of cells received less damage than cells in the outer layer. Also the dead cells on the outer

layer of the spheroid potentially acted as a temporal protective barrier against toxic materials as they increased the thickness of the ECM.

4.3.3. Toxicological assays

In the next step, the toxic effects of NPs were evaluated quantitatively utilizing lactate dehydrogenase (LDH) and methyl tetrazolium (MTT) assays. The LDH assay detects the amount of LDH that leaks out from the plasma membrane of damaged cells. This extracellular protein assay protocol was identical in both 2D and spheroid cultures. The MTT assay measures the amount of enzymatically-reduced MTT in the mitochondria. Thus, cell lyses utilizing a detergent or lyses buffer were required. In the scaffold-based spheroid culture system, an additional spheroid and scaffold destruction step was needed to make a homogeneous cell lysate such as torn down and sonication of scaffolds. To keep the same assay conditions, 2D culture samples were also treated in the same manner. Both cultures were treated with CdTe NPs for 12 hours and gold NPs for 24 hours before running the assays.

As expected from the morphological study, the toxic effects of CdTe NPs were significantly reduced in spheroid cultures. (Figure 4.8) Specifically, the results showed five times lower LDH leakage and two times more reduction of mitochondrial activity than in 2D cultures. The different sensitivity of the assay results was expected due to the nature of each assay and the different cell phenotypes. For example, the LDH assay is more sensitive to the number of cells at the solution interface capable of leaking their cytosolic contents into the media. All of the cells in 2D culture are exposed to the solution, while only a small portion of cells in spheroid culture make direct contact with

the solution interface. The remaining cells are enclosed by the outer layer of cells. For this reason, it caused a larger gap between two cultures. In the MTT assay, however, cells are dissolved before analysis and, therefore, the cell phenotype is more closely related than diffusivity or the number of exposed surface cells. In the case of spheroid culture, one can consistently see a considerably reduced proliferation rate which causes the accumulation of a quiescent cell phenotype, which in turn gradually reduces cell metabolic activity.[177] Since mitochondria produce about 90% of the adenosine triphosphate (ATP) required for cell survival, down-regulated mitochondrial activity in spheroid culture caused significantly reduced MTT activity compared to 2D culture despite the similar number of cells in both cultures.[218] Therefore, the MTT assay results after CdTe NP exposure are required to be calibrated with control samples. The drop in MTT activity was almost two times higher in 2D culture than 3D spheroid culture. (Figure 4.8B)

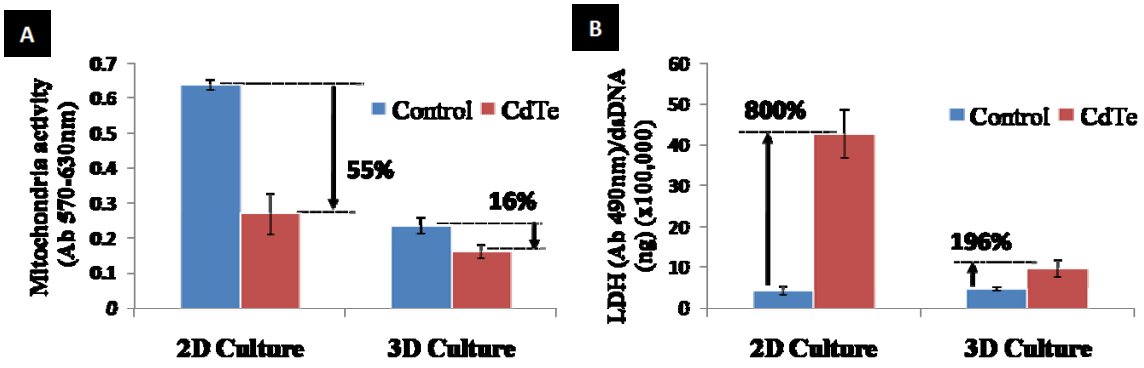

Figure 4.8 Quantitative comparison of toxicology assays between 2D and 3D spheroid culture after 12 hours of CdTe NP exposure. **(A)** Normalized LDH assay results. LDH activity before treatment was similar between the two cultures. However, after CdTe exposure, LDH leakage in 2D culture (1047%) was almost five times higher than spheroid culture (212%). **(B)** MTT assay results. In control samples, MTT activity in the 2D culture was more than 2 times higher than the 3D culture due to down-regulated cellular metabolism. Upon exposure to CdTe NPs, the decrement of mitochondrial activity from the control group in the 2D culture (56%) was approximately two times higher than the spheroid culture (31%).

Similarly a significantly reduced toxic effect of CTAB-Au NPs was observed in spheroid culture. More specifically, LDH leakage and decreased mitochondrial activity was three times lower in spheroid culture than 2D flat culture. Citrate-Au NPs slightly reduced mitochondrial activity (5%), but there was no substantial change of LDH leakage in both types of culture. (Figure 4.9)

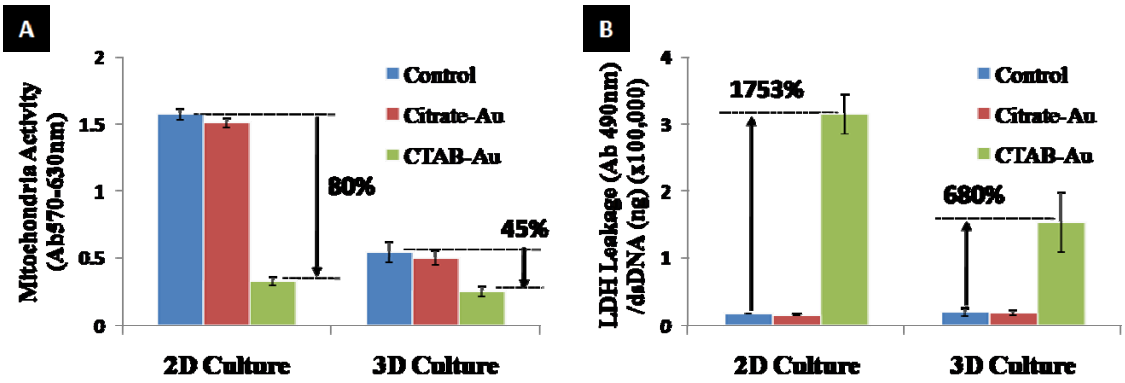

Figure 4.9 Quantitative comparison of toxicology assays between 2D and 3D spheroid culture after 24 hours exposure to Au NPs having two different stabilizers. CTAB-Au NPs caused severe toxicity but Citrate-Au NPs induced negligible toxic effect. CTAB-Au NP toxicity was significantly reduced when it was tested in 3D spheroid culture. **(A)** Normalized LDH assay results demonstrate three times less LDH leakage of CTAB-Au NPs in 3D culture. **(B)** MTT assay result shows that three times less reduction of mitochondrial activity of CTAB-Au NPs in 3D culture.

4.3.4. Cell death mechanisms

The MTT assay results reflect that reduced CdTe NP toxicity in spheroid culture is closely linked to a change of cell phenotype. With this in mind I hypothesized that CdTe NP-induced toxicity would cause different cell death mechanisms, i.e., dying cells in spheroid culture would undergo more apoptosis but less necrosis than in 2D culture. Necrosis is a catastrophic cell death caused by acute cellular injury, resulting in the release of cytosolic proteins into the intercellular space. Apoptosis is a controlled, natural

cell death mechanism. Compared to necrosis, the apoptotic process does not release intracellular constituents into the extracellular milieu but instead presents various signaling molecules such as caspase proteins. However, these signaling molecules are only temporarily presented before the cells undergo secondary necrosis, which is similar to necrotic cell death. Therefore, a time-dependent study is necessary to distinguish apoptosis from necrosis.

In order to test our hypothesis, the intensity of apoptotic (Caspase-3/7 assay) and necrotic (LDH assay) processes after 1, 2, 4, 6, 8, 12 and 24 hours of CdTe NPs exposure were measured. (Figure 4.10) At these time points the culture medium was collected for the LDH assay, while the remaining cells on plates and scaffolds were further processed for the Caspase 3/7 assay. In both cultures the apoptosis and necrosis values had similar trends yet they displayed substantial differences. In 2D cultures, the LDH assay value gradually increased until 8 hours and then suddenly jumped, while in spheroid cultures it was slightly enhanced until 12 hours followed by a moderate increase between 12 and 24 hours. Since a sudden increase of LDH leakage designates the point of prevalent necrosis or secondary necrosis at the end of apoptotic cell death, these data demonstrate that necrotic points of spheroid culture, either by necrosis or apoptosis, is much more retarded than 2D culture.

The caspase assay results more clearly showed phenotypic effects. In 2D culture the caspase activity continuously decreased with different level of retrenchment over time—gradually diminishing for 2 hours before rapidly dropping. Please note that a relatively high concentration of unmodified CdTe NPs was intentionally used. On the other hand, in spheroid culture an initial jump in the caspase activity was first observed,

followed by a gradual decrease. I also observed inherently higher caspase activity in 2D cultures than spheroid cultures similar to MTT results. These data obviously indicate that cells in spheroid culture undergo more apoptotic processes than 2D culture due to the cellular phenotypic change.

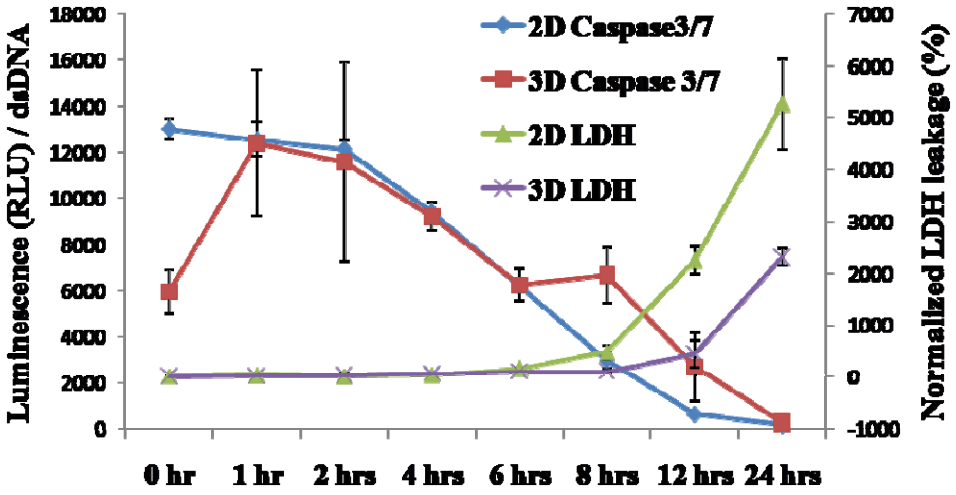

Figure 4.10 Kinetic studies of the cell death mechanism. Representative data of combined LDH and Caspase 3/7 assay results over a span of 24 hours, with measurements at 8 different time points. The results were normalized with dsDNA quantification data. The LDH assay, the absorbance value on the right Y-axis, was used as a necrosis marker. The Caspase 3/7 assay, the luminescence value on the left Y-axis, was used as an apoptosis indicator. (n=3 at each time point, total n=24 in each type of culture).

These results are well correlated with previous animal testing results.[228, 234-236, 254] For example, Zhang et al. reported that intravenous injection of CdTe NPs into rats did not cause any damage to major organs. Although locomotive activity was reduced shortly after dosing, it returned to normal within 24 hours. [233] In fact nanoscale materials undergo various physiological processes in the body, including circulating in the blood stream, accumulating in specific organs, cellular uptake, and

renal excretion.[78, 255-257] It seems that such diverse and complex physiological processes cooperatively act to mitigate the toxic effects of NPs *in vivo*.

Similar to the findings, the reduced toxic effects of drug compounds in multicellular spheroid culture models were previously reported by other investigators.[258] Also there are several reports highlighting the unique opportunities of spheroid culture as an *in vitro* toxicity testing application.[211, 215, 259] Nevertheless, it has not been widely accepted in the actual toxicity screening field because there are still technical barriers preventing current spheroid culture systems from being used in practical and industrial applications, such as standardization, reproducibility, high yields, and simple manipulation for experimental intervention and assay purposes. ICC hydrogel scaffolds significantly improve all these issues. Highly controlled ICC structure and material resulted in excellent control and standardization of prepared liver tissue spheroids. A simple and versatile fabrication method allows the mass production of a diverse range of macro- and micro-scale ICC scaffolds. It can also be readily combined with currently utilized HTS equipment. Additionally, the transparent hydrogel matrix enables the deep confocal 3D imaging of spheroids that is essential for HCA.[214, 260]

In perspective, one can also envision other advantages of spheroid culture system. (i) It enables long-term toxicity testing. Currently, all 2D culture-based toxicity testing is short term (less than a few days) due to continuous cell growth. However, longer toxicity testing is necessary to understand how toxic molecules affect cellular behavior not instantly but gradually, such as chronic exposure to toxic substances. The quiescent phenotype observed in spheroid culture is beneficial to treating cells for a longer period of time. (ii) It can be used as a model system for understanding tissue-level healing

processes after damage by toxic substances. As shown before, the interior spheroid was protected by an outer layer of cells, suggesting a capacity in spheroid culture for physiological repair, which is closer to real tissue biology. (iii) Applying this system to tumor spheroids would be a very appropriate model system for testing the effectiveness of newly-engineered NPs which are related to cancer treatments, such as tumor cell targeting and delivering therapeutics into solid tumors.

4.4. Summary

Established standardized liver tissue spheroid culture model was successfully applied to the *in vitro* toxicity testing of NPs. The results showed great differences in comparison with common 2D cell culture, while more correlating well with the data from animal tests. Two important aspects of the 3D spheroid culture exemplify the differences with 2D cultures and the greater resemblance to *in vivo* tissue-like physiological responses; (i) tissue like mass transport due to dense tissue-like cell clusters and ECM layer present and (ii) cell phenotype changes due to intensified cell-cell interactions. The ICC scaffold-based spheroid culture system clearly indicate the significance of the 3D cell culture model to *in vitro* testing of NPs toxicity and the need of implementing standardized 3D *in vivo* models for NP research.

In the same way, the ICC scaffold-based spheroid culture system would undertake initial toxicity testing of drug candidate compounds as producing more physiologically relevant toxicological information. As a result, it can potentially improve the predictive power of *in vitro* screenings which in turn critically contribute to a reduction in animal testing and a clinical stage failure rate.

CHAPTER V

BIOACTIVE ICC SCAFFOLDS FOR CELLULAR CO-CULTURES

5.1. Introduction

Adequate understanding and proper methods of control of cell signaling are important in emulating hematopoietic stem cell (HSC) niches since the rate and direction of the differentiation of HSCs are strongly affected by their 3D microenvironment and signaling molecules.[261, 262] Recent studies have shown that a 3D culture environment significantly promotes the efficiency of stem cell differentiation[263-265]. Intensive cell-cell and cell-matrix interactions have been distinguished as key factors that determine the fate of individual cells by serving as important communication channels.

As shown in Chapter 2, ICC systems possess high surface area with void fraction of 97% (i.e. combining 74% effective cellular porosity and 23% bulk hydrogel porosity) and a regularly spaced network of pores which provides a mechanically strong, well-connected open porous geometry. These features enhance cell seeding efficiency, transport of nutrients and metabolites, and the rapid and uniform distribution of soluble signaling molecules. In addition the excellent control over porosity combined with a high degree of organization of ICC scaffolds enable much better control of cell-cell and cell-scaffold interactions. Such unique characteristics of ICC scaffolds make them particularly

convenient for the use with HSC cultures, which can help uncover methods for successful tissue engineering of HSC niches such as bone marrow and thymus.

Besides these advantages, the high level of organization and geometrical identity of different cavities make possible effective computer modeling of scaffold properties such as diffusion of nutrients and other signaling molecules, cell-cell and cell-matrix interactions, and other processes, which can substantially reduce experimental load. For instance, in fabricating effective scaffolds for *in vitro* tissue engineering applications, several design variables such as mechanical strength, diffusion and cell adhesion have to be considered. Currently, a significant bottleneck is the lack of adequate oxygen and nutrient transport as well as cell migration to the interior of the scaffold.[266]

The hydrogel matrix rarely supports adherent cells adhesion without surface modification, because acrylamid polymer chains do not have cell adhesion receptors, and the hydrophilic nature of hydrogel inhibits adsorption of cell binding proteins on the gel surface. To render the surface bioactive, a layer-by-layer (LBL) surface modification technique was utilized instead of commonly used covalent coupling of specific peptide sequences such as RGD or an entire ECM protein to the polymer. It has been reported that 2D polyelectrolyte multilayer supported anchorage dependant cell attachment without using adhesive proteins. The driving forces of LBL coating are the electrostatic, Vander-Waals, and hydrogen bonding interactions between oppositely charged polyelectrolytes dispersed in aqueous solution. This unique feature of the LBL technique allows a complex porous 3D geometry, such as the intricate and convoluted ICC surface, to be coated as long as fluid transport in and out of the sample is not severely constrained.

In this chapter, a model system combining two types of cells co-existing in an ICC scaffold will be introduced having in mind the recreation of HSC niches in the bone marrow and thymus. The selection of particular model cell cultures was also aided by the fact that the characteristic geometry of the ICC scaffolds resembles that of bone marrow and thymus niches, i.e. stromal cells cover the surface and well intersticed sinus cavities. The surface of ICC hydrogel scaffolds was coated with LBL assembly of clay nanoplatelets and polydiallyldimethylammonium (PDDA) polymer to support stromal cell adhesion. Rotary cell culture vessels were utilized instead of micro-well plates to make dynamic culture environment. In addition, open porous ICC scaffolds were used rather than pocket ICC scaffolds to more effectively accommodate dynamic flows within the ICC geometry.

Human thymus epithelial cells (Hs202.Th) and human monocytes (HL-60) were used as anchorage dependent feeder cells and suspension cells mimicking progenitors, respectively. Before using HSCs, I tried to use the HL-60 cells because it is easier to deal with and has been provided a unique in vitro model system for studying the cellular and molecular events involved in the proliferation and differentiation of normal and leukemic cells.[267] Microscopic characterization data clearly demonstrated the co-existence of two types of cells in same ICC chambers. Diffusion of nutrient and cell-cell interactions within ICC scaffolds were also evidenced by simplified Brownian Dynamics (BD) and Monte Carlo (MC) simulations taking advantage of its unique 3D morphology.

5.2. Materials and Methods

5.2.1. ICC scaffold preparation

CCs were prepared with PS beads (D=100μm) following the protocol in Chapter 2. Final scaffolds have 6.5mm diameter and 0.5-1mm thickness. All pores are open to the outer fluid which facilitates cell motility and media exchange in a dynamic culture condition.

5.2.2. LBL 3D surface modification

The surface of polyacrylamide hydrogel ICC scaffolds was coated with sequential layers of negatively charged 0.5% (w/w) clay platelets (average dimension of 1nm thickness and 70-150nm in diameter, Southern Clay Products) dispersion and positively charged 0.5% (w/w) PDDA (MW=200,000, Sigma) solution utilizing a LBL surface modification technique. ICC hydrogel scaffolds were immersed first in PDDA solution for 15 minutes and rinsed in deionized water for 30 minutes. Then the scaffolds were immersed in clay solution for 15 minutes and rinsed again with deionized water for 30 minutes. This LBL coating cycle was repeated 5-10 times. The initial and outermost layer was PDDA and clay nanoparticles, respectively. To demonstrate 3D LBL coating on hydrogel ICC scaffolds, negatively charged fluorescein isothiocyanate (FITC) conjugated albumin (Sigma) was utilized instead of clay nanoparticles. An ICC hydrogel scaffold coated with ten bilayers of FITC-albumin and PDDA was imaged under confocal microscope (Leica SP2) with 10X objective lenses. Confocal series images taking 160μm depth were three dimensionally reconstructed using imaging software. In order to visualize polymeric component, fluorescent-PDDA was prepared taking advantage of

electrostatic interactions between FITC (negatively charged) and PDDA (positively charged). Unbound FITC molecules were separated via dialysis process.

5.2.3. Cell cultures

Human thymic epithelial cells Hs202.Th (CRL-7163) and human premyeloblasts HL-60 (CCL-240) were purchased from ATCC (Manassas, VA). Hs202Th cells were grown in Dulbecco's Modified Eagle's Medium (DMEM) supplemented with 10% FBS (GIBCO, CA). HL-60 cells were cultured in Iscove's Modified Dulbecco's Medium (IMDM) containing 20% FBS. The cells were maintained at 37ºC with 5% CO2 and media was changed twice a week until they reached a confluent or desired population on T-75 culture flasks.

5.2.4. Dynamic 3D co-culture

Co-culture was carried out in a 10ml rotary cell culture vessel (RCCS-4D, Synthecon). Scaffolds were sterilized by soaking in 70% EtOH for one hour followed by washing in PBS for 15 minutes twice. $2x10^5$ Hs202.Th cells were placed in a culture vessel, which subsequently was filled with medium. The rotation speed was set at 12 rpm for the first 12 hours and later it was decreased to 8 rpm, the normal speed. The medium was replaced once every three days. On day 6, the HL-60 cells were stained with 5μM chloromethyl derivatives fluorescent dye (CMRA) (Molecular Probes) and the Hs202.Th cells growing on the scaffold were stained with carboxyfluorescein diacetate succinimidyl ester (CFDA-SE) (Molecular Probes). After that, the culture vessel medium was changed to IMDM supplemented with 20% FBS, and $1x10^6$ pre-stained HL-60 cells were seeded. Co-culture was maintained for 5 days.

5.2.5. Modeling approach

The basic modeling problem is the escape of a particle trapped in an enclosed cavity through an aperture on the surface of the cavity.[268-271] This problem can be greatly simplified when the size of the aperture is small enough, because then it can be assumed that before being evacuated, the particle samples the cavity thoroughly. Under these conditions, the escape of the particle is a rare event that is characterized by a single exponential decay.[266, 271] Mathematically, it may be represented as

$$S(t) = \exp(-4bDo/V) \qquad (1)$$

S(t): survival probability of the particle after a time t has elapsed
Do: diffusivity of the particle in free solution
b: radius of the circular aperture
V: volume of the cavity

For spherical cavities arranged on a simple cubic lattice connected to neighboring cavities by pores of radius *b*, the effective diffusivity is given by $D_{eff}/Do=6b/\pi R$ where R is the radius of the spherical cavity[272, 273]. Generalizing their expression for cubic lattices with co-ordination number Z (Z = 6 for a simple cubic lattice), we get

$$D_{eff}/Do = (Z/\pi)\,(b/R) \qquad (2)$$

Eq. (2) implies that escape of a particle from a cavity is proportional to the number of openings Z, i.e. the openings operate independently of each other. However, as the number of openings per cavity increases, there is significant cross-talk between adjacent openings, and the diffusion characteristics may deviate from Eq. (2).[271] This fact also underscores the importance of having the ordered scaffold for which the location of openings is geometrically defined. In case of random distance between openings as in

many chaotically organized scaffolds, the degree of cross-talk between them is uncertain. Here cavities formed from spheres close-packed on a face-centered cubic lattice of ICC were considered, for which Z=12. BD and MC simulations were used to describe the diffusion characteristics of particles in this lattice and compare it with Eq. (2).

To model the cavities we first laid down spheres of radius R_{or} in a close packed hexagonal lattice so that each sphere had 12 other spheres touching it, which produces ICC geometry of the scaffolds. To form the intercavity pore of radius *b* we ‘‘enlarged’’ the original spheres slightly. This expansion caused the spheres to interpenetrate with a lens-shaped region of interpenetration. The edge of the lens defined the perimeter of the intercavity pore. From Figure 5.1A, it may be seen that $R^2 = R_{or}^2 + b^2$, when b/R_{or}~0.1, R/R_{or}~1.005. The volume of the lens, thus formed, can be derived using straightforward geometrical arguments to be

$$V_{lens} = 2\pi R^3 \, (2/3 + 1/3 \, (R_{or}/R)^3 (R_{or}/R)) \qquad (3)$$

The void fraction for a close-packed FCC lattice is $\pi/3\sqrt{2}$. After the expansion of the spheres the void fraction increases to

$$\varphi = \pi / 3\sqrt{2} \, (9 \, (R/R_{or})^2 - 5 \, (R/R_{or})^3 - 3) \qquad (4)$$

Again, for b/R_{or}~0.1, φ increases slightly from 0.7405 characteristic of close-packed spheres, to φ = 0.7515. We then uniformly distributed the nutrients in the matrix of interconnected cavities. In the simulations, we considered only Brownian and excluded volume effects.

For point particles, we did BD simulations using reflecting boundary conditions for collisions with cavity walls. The time-step Δt was chosen so that the characteristic

hopping distance $\sqrt{6D_0\Delta t}$ was 0.05*b*. We found that decreasing Δt such that $\sqrt{6D_0\Delta t}$ = 0.01*b* did not produce statistically important differences. During the course of the simulations we observed a set of trial moves which involved the migration of a nutrient from one cavity to another without passing through the interconnecting pore, but instead, by jumping over the cavity walls. Such moves obviously violated excluded volume conditions and we employed reflecting boundary conditions to rebound the particles back into the original cavity.

For finite-sized particles, we did only dynamic MC simulations, choosing the same hopping distance, Δr=0.05*b*. Any trial move that violated excluded volume constraints with the walls or with any of the other particles was rejected. Also, trial moves which involved migration of nutrients from one cavity of ICC to another by jumping over cavity walls were also rejected. We found that for point particles, both the BD and MC calculations gave essentially indistinguishable results.

The parameters used in the calculations were normalized as follows: radius of the original spheres, R_{or}=1.0, radius of the pore, b=0.1, and free solvent diffusivity D_0=0.0001. We used periodic boundary conditions and varied the size of the simulation box (for different concentration of nutrients) such that the number of nutrients was greater than 1000. We collected position data of all the particles at fixed intervals, and calculated the mean squared displacement (MSD) and diffusivity using standard methods.

5.3. Results and Discussion

5.3.1. Modeling molecular diffusion and cellular interactions

Molecular diffusion in 3D ICC geometry

The solubility of oxygen in water at 25°C is approximately 8mg/l, which corresponds to a concentration of approximately 1mM. Assuming the radius of a cavity in the ICC lattice to be 100μm, which is a median of cell culture scaffold size used previously in the experiments with hepatocytes and bone marrow cells[186, 188, 271], the number of oxygen molecules per cavity is of the order of 10^{12}. Simulating such a large system is an almost impossible task. However, we find that the radius of an oxygen molecule along with its solvation shell is about 0.5nm[274], and that the size of a glucose molecule which is another important nutrient, is also about 1nm.[275] Therefore, the size of these nutrients is about $10^{-4}\,b$, where b is the size of the pore connecting two cavities. It thus seems reasonable to treat these nutrients at point particles. For the ICC scaffold geometries relevant to cell organization and culturing, this mathematical approach will most likely hold in all possible cases. This assumption eases the computational problem dramatically. Point particles have no dimension and hence do not exert any repulsive excluded volume force on each other. Thus, they cannot ‘‘see’’ neighboring molecules and the diffusion characteristics are independent of the concentration of the nutrients in the medium in which they diffuse. This is brought out in Figure 5.1B which compares the ratio of D(t) to D_0 of a point particle at different concentrations. $t^* = R^2/6D_0$ is the time-scale at which a particle understands that it is confined in the cavity. As expected, the diffusivity falls to its effective long term value around $t/t^* \sim 1$, and is independent of the concentration.

The average value of the effective diffusivity is $D_{eff}=0.3D_0$. If we use Eq. (2) to compute the effective diffusivity, we obtain $D_{eff}=0.382D_0$. As the co-ordination number Z increases, the probability that the particle has not completely sampled the cavity before it escapes also increases, as mentioned previously. If we define $t`= 2R^2/D_{eff}$ [272]to be the characteristic time of escape and identify t* with the characteristic time to sample the cavity, then a small value of t*/t` signifies that the particle has sampled the cavity well. Using Eq. (2), we find that even for Z=12, $t^*/t`= 0.5D_{eff}/D_0= 0.191$, which indicates that it might still be reasonable to assume that the cavity is well sampled.

The observed discrepancy between D_{eff} and D^*_{eff} could, therefore, be a consequence of ‘‘cross-talk’’ between the adjacent apertures. Each pore occupies only a small fraction ($\sim 0.25(b/R)^2 \sim 0.0025$) of the surface of the sphere. However, as elaborated in Berg et al. for a somewhat different case, when a number of small apertures are evenly distributed on the surface of a sphere their cooperative behavior can be significant. Crudely, this may be understood as follows: the presence of an aperture depletes the density (or alternatively likelihood of existence) of particles in its neighborhood. This, in turn, curtails the rate at which particles flow through adjacent apertures. Thus, eventually, the net transport of nutrients is less than what it would have been, if the apertures truly operated independently of each other.

Additionally, Figure 5.1B also depicts the diffusion characteristics of point particles at low concentration (C = 1.0 particles/volume), when the size of the aperture is halved to b=0.05. It can be seen that D_{eff} decreases, as expected, to an average value of $0.165D_0$. If the conditions under which Eqs. (1) and (2) were strictly satisfied then D_{eff} would have been proportional to the size of the aperture b. We suspect that the value

observed from simulation $D_{eff}(b=0.05) = 0.165D_0$ is greater than what we would expect naively, i.e. $0.5D_{eff}(b=0.1) = 0.150D_0$ because of decreased cross talk between the pores. If there was no cross talk between the pores then $D^*_{eff}(b=0:05) = 0.191D_0$.

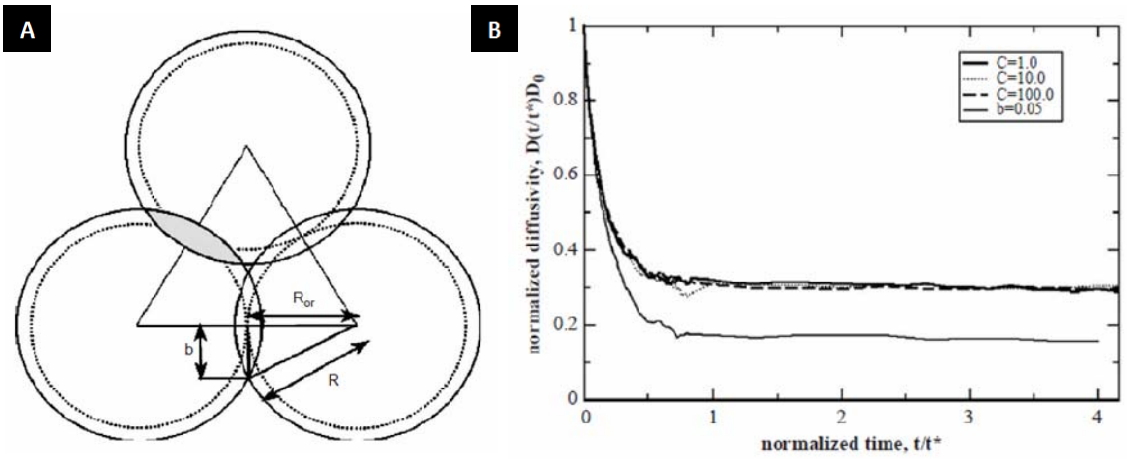

Figure 5.1 Molecular diffusion modeling in ICC geometry (A) The geometrical relation between the original radius of close packed spheres, Ror, the radius of the inter-cavity pore, b and the radius of the swollen spheres, R is given by $R^2 = R_{or}^2 + b^2$: The difference between R_{or} and R has been exaggerated for clarity. The volume of the shaded lens shaped region is given by Eq. (3). **(B)** Effect of concentration (thick, dotted and dashed lines) and size of aperture (thin line) on the effective diffusivity of point particles diffusing in an ordered matrix of spherical cavities. As the size of the aperture is reduced from b=0.1~0.05 (C=10.0), the effective diffusivity, D_{eff} is approximately halved from 0.300 to 0.165.

Cellular interactions within ICC geometry

Floating cells can travel deep into the scaffold through interconnecting channels while they are temporarily entrapped in an ICC chamber due to limited channel numbers and size. To study the interaction of a floating cell with the scaffold quantitatively, we constructed a simplified BD model. The cell was treated as a hard sphere of radius, a_{cell} that is suspended in an ICC geometry, composed of hollow spherical chambers of nominal radius, R, connected by channels of radius, b. To simplify the treatment, we assumed that the fluid inside the scaffold was quiescent and that the motion of the cells

was purely diffusive. Under the assumptions stated above, the motion of the cell results from a balance between the drag force and the random Brownian force,

$$\zeta \, d\mathbf{r}/dt = \boldsymbol{F_B} \qquad (5)$$

Where $\zeta=6\pi\eta a_{cell}$ is the hydrodynamic drag exerted by the solvent of viscosity (η) on a cell of radius (a_{cell}), and **r** is the position vector of the center of mass of the cell. The Brownian force, $\mathbf{F_B}$, satisfies the fluctuation-dissipation theorem[276] which necessitates $\langle \mathbf{F_B} \rangle = \mathbf{0}$, and $\langle \mathbf{F_B F_B} \rangle = 2kBT\zeta\mathbf{I}$. Here, **I** is the unit tensor, $k_B=1.38x10^{-23}$ JK^{-1} is Boltzmann's constant, and T is the absolute temperature.

The diffusivity (D) was obtained from the hydrodynamic drag via the Einstein relation[276], $D=k_BT/\zeta$. In accordance with microscopy measurements, we took R=50μm, b=12.5μm, and a_{cell}=7.5μm. Thus, $\zeta=6\pi(1cP)(7.5\mu m)=1.414x10^{-4}g/s$, and $D=k_BT/\zeta=2.91*10^{-2}\mu m^2/s$. We used the algorithm outlined in Larson[276] to implement the BD simulation, choosing the simulation time step, d*t*, so that $\sqrt{6Ddt} \approx 0.05a_{cell}$. We employed reflecting boundary conditions to model collisions between the cell and the scaffold.

Grigoriev *et al.* considered a dimensionless Brownian particle trapped inside a spherical chamber of volume *V*.[268] They estimated that the time, t^*, that it takes for the particle to escape from a small circular hole of radius b on the surface of the chamber, is given by $t^*=V/4bD$, where *D* is the diffusivity of the particle. We adapted the expression for t^* to obtain a crude estimate for the escape time of a Brownian particle of finite size from an ICC scaffold as,

$$t^*_{ICC} = (\pi/3ZD)\,(R-a_{cell})^3/(b-a_{cell}) \qquad (6)$$

where Z=12 is the co-ordination number of the ICC lattice. From Eg. (6), we obtained $t^*_{ICC} \sim 5.5*10^5/12$ seconds ~ 12 hours. Thus, the ICC geometry provides very suitable geometry for cell interactions due to partial entrapment of the cells in the cavity.

We simulated the dynamics of the cell in the ICC scaffold using BD, and recorded its trajectory from t=0 to t=1000 days. Over this period, the cell visited several chambers. From the simulation, we observed that by the time the cell vacated a chamber by escaping through the interconnecting channel to another chamber, it thoroughly, and uniformly, sampled the whole chamber. In other words, the amount of time the cell spent in any region of the chamber was proportional to the volume of that region. Figure 5.2A shows a cross section of a spherical chamber that has been divided into shells of equal thickness, $\Delta R = a_{cell}$. These shells do not have the same volume. For illustration, if we approximate the volume of a shell by, $\Delta V_{shell} = 4\pi R_i^2 \Delta R$, where R_i is the inner radius of the shell, we can see that the volume of the outer shells is greater than that of the inner shells. As mentioned previously, the center of mass of the cell resides in a shell, in proportion to the volume of that shell. Thus, it spends a significant fraction of time (about 41%, see Figure 5.2B) in the outer-most shell, where the distance between the surface of the cell and the inner surface of the chamber is less than or equal to the radius of the cell. (Figure 5.2C) Thus the ICC geometry fosters contacts between the cell and the matrix surface or between the suspension and adherent cells in a co-culture.

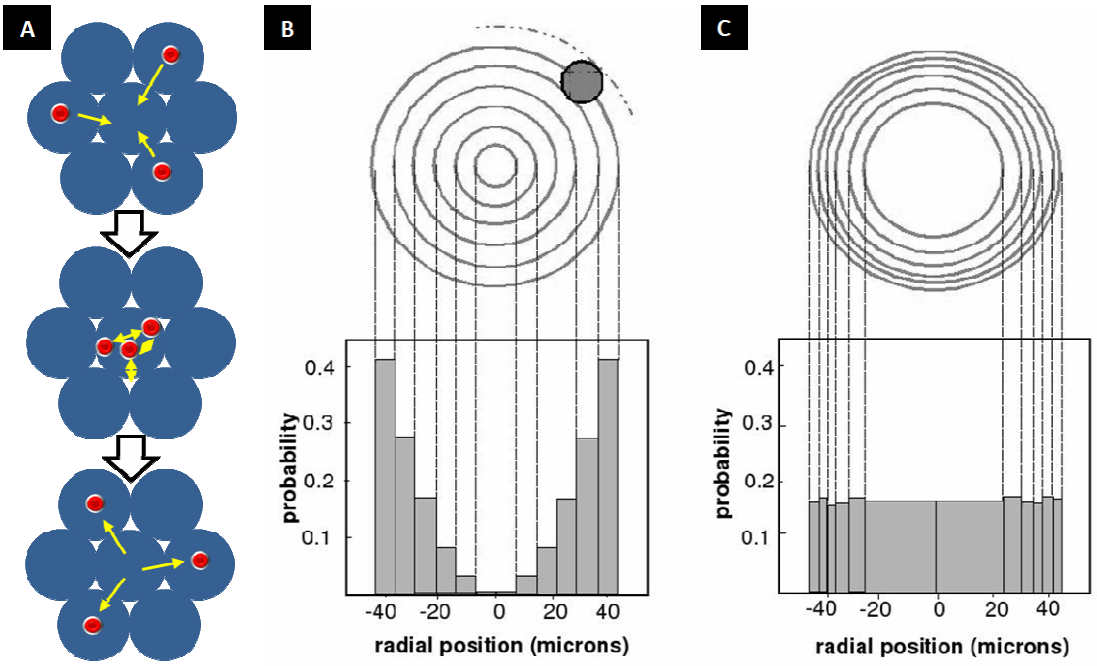

Figure 5.2 Modeling results of cell entrapment and interaction within ICC geometry. (A) Schematics of ICC topology and cell contacts within ICC geometry. Floating HSCs enter into a pore through interconnected channels that have diameters 2-3 times larger than that of a single cell. Temporarily entrapped HSCs undergo intense contacts with ICC pore surface where stroma cells grow. **(B-C)** Modeling data of radial probability distribution of a finite-sized Brownian particle of radius 7.5μm diffusing in a spherical ICC chamber obtained from BD simulations, when the chamber is divided into shells of the same **(B)** thickness, and **(C)** volume. In (B), the dotted arc and the disc represent the inner surface of the chamber, and the cell which is modeled as a hard sphere, respectively. The thickness of each shell is equal to the radius of the cell, a_{cell}. From (C), it can be seen that the cell spends the same amount of time in each of the equi-volume shells, whereas in (B), it spends more time in the exterior shells due to their greater volume.

5.3.2. LBL 3D surface modification

The LBL molecular assembly process is a novel film deposition technique utilizing electrostatic interaction between oppositely charged poly electrolytes[88]. The process consists of sequential dipping of a substrate into solutions of oppositely charged species alternating with water rinsing. In each dipping cycle, a monolayer of the species is adsorbed to the substrate while the rinse step removes their excess. The next dipping gives rise to enhanced adsorption of oppositely charged species, which is also

accompanied by the switch in the surface charge. The film thickness can be adjusted by repeating this cycle as many times as one needs, and the composition of films can be engineered through the sequential deposition of different materials without the need of complex chemistry. Notably, a uniform coating can be achieved in any substrate including a complex 3D porous ICC geometry, as long as fluid transport in and out of the sample is not severely constrained. This is probably the only technique that can create organized layered structures on cell scaffolds with intricate porosity and 3D organization[87]. (Figure 5.1B)

To provide adequate adhesion of stromal cells, the pore surface of ICC hydrogel scaffolds was coated with clay/PDDA multilayer following the LBL technology[277]. PDDA is a positively charged polymer, while clay is negatively charged nano-platelets. (Figure 5.1A) The flat shape of clay NPs effectively covered the hydrogel surface combined with PDDA like brick-and-mortar. As a result, a thin layer of nano-composite was prepared on the surface of the scaffold. The hybrid organic-inorganic composite is mechanically compatible with the hydrogel and does not delaminate. Coated clay NPs also created nanoscale roughness, increased charging on the surface, and created much stiffer film than hydrogel[277]. Increase of Young modulus was shown to be the primary factor determining the adhesion of cells to materials[16, 278]. These synchronous effects promoted cell adhesion. Normally five bilayers of clay/PDDA effectively changed the surface property from cell repulsive to cell adhesive, and successfully support stromal cell adhesion on the hydrogel scaffold. In addition, nano-composites have minimal light scattering because the characteristic diameter of the inorganic component is smaller than

the wavelength of light, which is quite relevant for optical interrogation of biological processes.

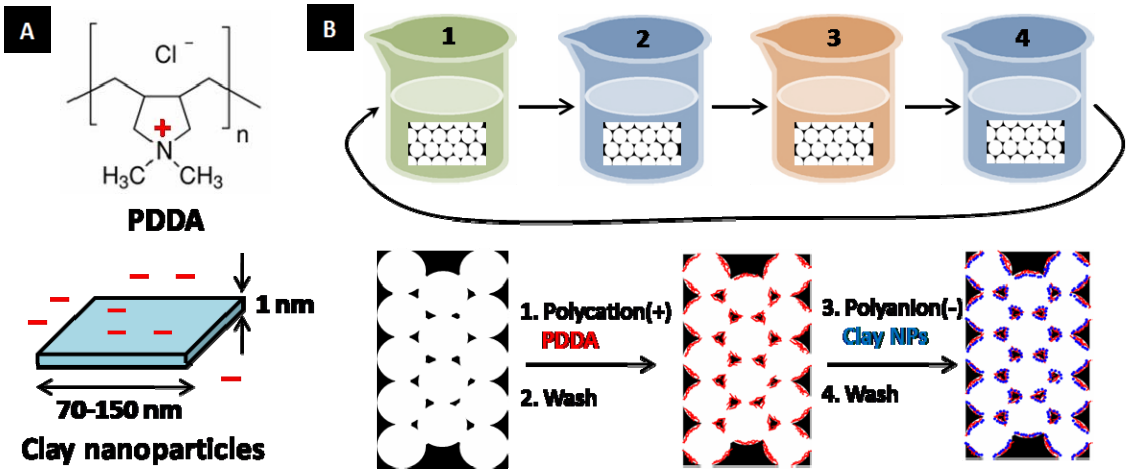

Figure 5.3 Schematic of clay/PDDA LBL surface coating of ICC hydrogel scaffold. (A) Schematic of PDDA and Clay nanoparticles. **(B)** Schematic of LBL surface coating procedure.

At first, the clay/PDDA LBL film formation was characterized on 2D hydrogel surface. Compared to glass slides substrate, hydrogel surface retains quite different physical and chemical properties such as high porosity, low mechanical strength and hydrophilicity, which caused somewhat dissimilar LBL film growth patterns. For instance, the LBL components did not cover the entire hydrogel surface during initial few dipping cycles rather than partially coat. Normally it took 3-5 cycles to completely cover the hydrogel surface as confirmed by gradually disappeared pores. The LBL coating on hydrogel surface was also thicker than a glass slide probably due to its porous hydrophilic structure. However, weak mechanical strength of the hydrogel made hard characterize the growth pattern and thickness of the LBL film. In addition, different cell adhesion and growth patterns were observed. For example, cells were fully spread on a glass substrate while they were less stretched on a Clay/PDDA coated hydrogel surface. (Figure 5.4E-F)

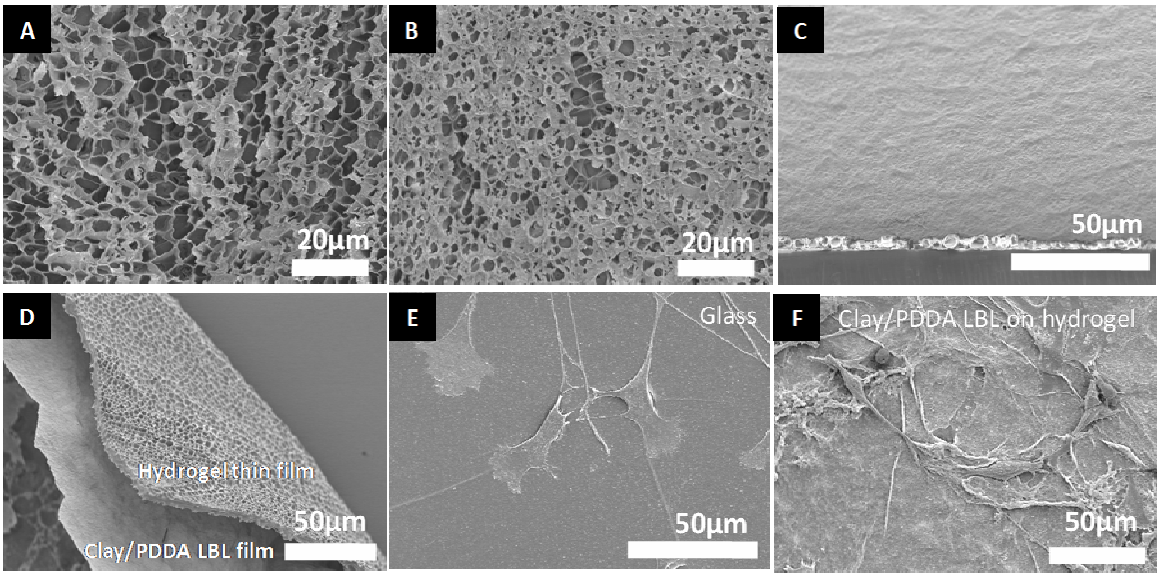

Figure 5.4 Clay/PDDA LBL film formation on 2D hydrogel and cell growth pattern Gradual surface coverage of LBL coating **(A)** 1 bilayers, **(B)** 3 bilayers, **(C)** 5 bilayers, and **(D)** 25 bilayers on a thin 2D hydrogel substrate. Stromal cell adhesion and growth on **(E)** a glass slide and **(F)** 2D hydrogel surface 5 bilayers of clay/PDDA LBL film layered.

Next, the LBL coating was applied to 3D hydrogel scaffolds. Since both clay and PDDA do not have fluorescent, the feasibility of 3D LBL coating was confirmed by employing fluorescent technique. For example, negatively charged FITC-conjugated albumin properly interacted with positively charged PDDA polymer. As a result, nicely formed 3D albumin/PDDA LBL film was observed under confocal microscope. (Figure 5.5B) In order to directly visualize the clay/PDDA multilayer, FITC was electro-statically bound to PDDA before using. Although the clay/PDDA LBL film quality was less uniform compared to the film prepared on a glass slide, it was successfully extended to the surface coating on ICC hydrogel scaffolds that supported stroma cell adhesion and growth. (Figure 5.5C)

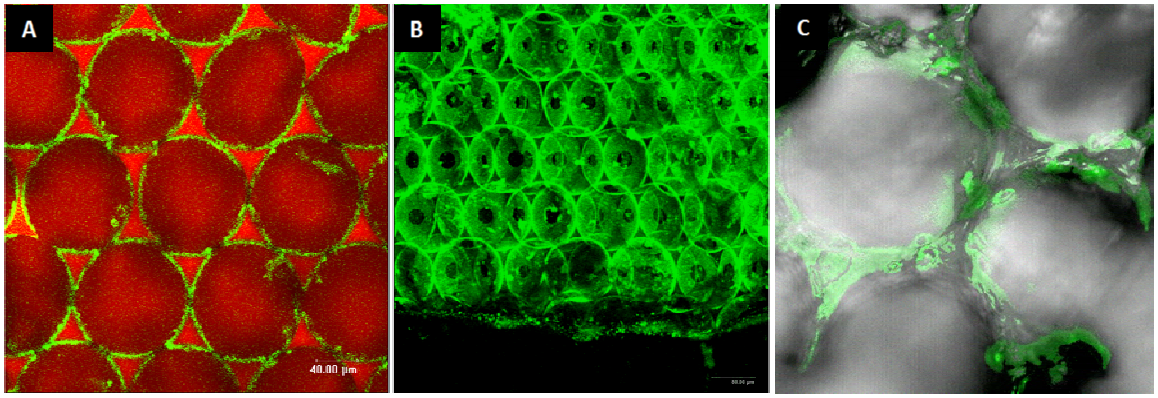

Figure 5.5 Confocal images of LBL film formation and stromal cell adhesion on ICC hydrogel scaffolds (A) Ten bilayers of fluorescent labeled PDDA (green) and clay NPs on ICC hydrogel scaffold soaked in rhodamin solution (red) **(B)** 3D reconstructed confocal image of ICC hydrogel scaffold after five bilayers of FITC-albumin(green)/PDDA LBL coating. **(C)** HS-5 bone marrow stromal cell adhesion on the scaffold after five bilayers of clay/PDDA LBL coating.

5.3.3. Dynamic 3D co-culture

Human thymic epithelial cells and human premeylote monocytes were co-cultured in a rotary cell culture bioreactor. Rotary motion induced convective flow, and the scaffold geometry utilized this flow as a continuous driving force for the cell movement. After five days of co-culture, the hydrogel ICC scaffolds were imaged through a confocal microscope. Different emission ranges of fluorescent dyes were used to stain the thymus cells and monocytes with green and red, respectively. Thymic epithelial cells attached to the cavity were observed as green circles, and floating monocytes were imaged as red spots. (Figure 5.6) Although many monocytes were diffused out of the scaffold during the sample preparation, some of them remained entrapped inside the pores. Confocal cross-sectional images reveal that suspended cells were distributed uniformly throughout the scaffold. (Figure 5.6D)

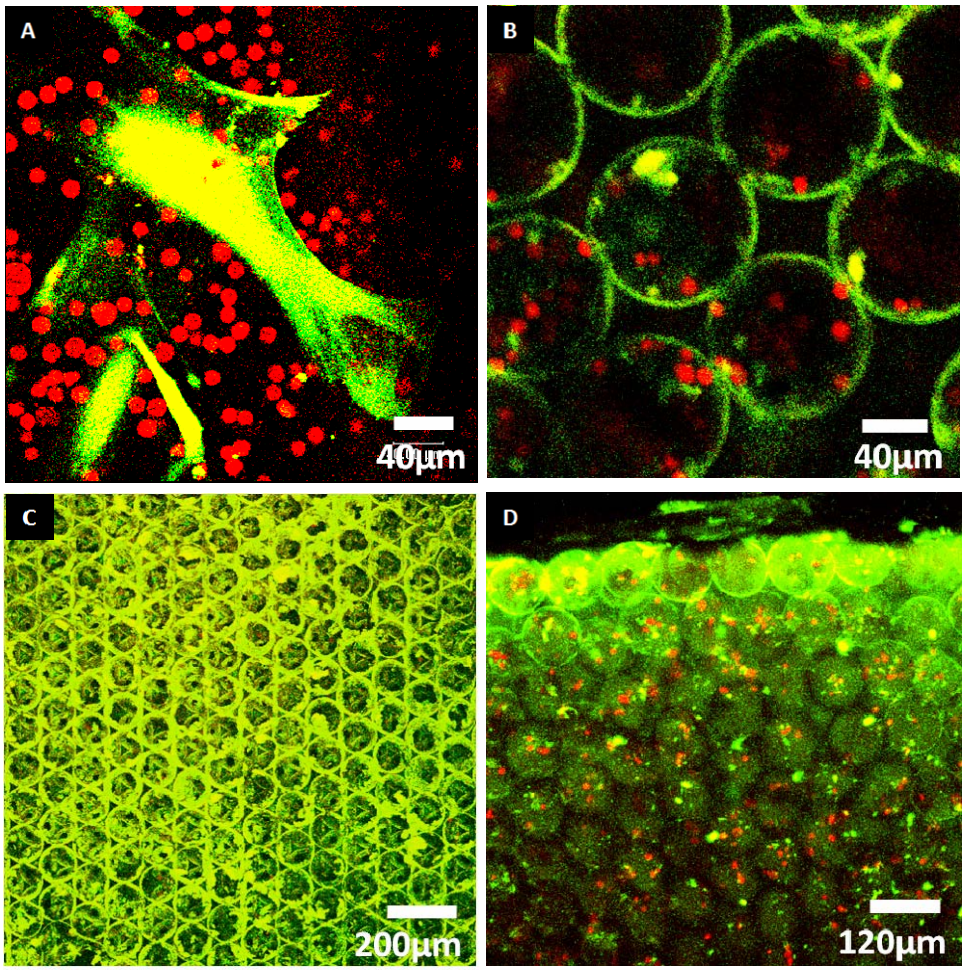

Figure 5.6 Confocal images of 2D and 3D co-culture models Representative image of co-culture **(A)** on a 2D substrate and **(B)** in an ICC scaffold: thymic epithelial cells (green) and monocytes (red). **(C)** Top area image shows the surface of the scaffold was densely covered with thymic epithelial cells. Most of monocytes around the edge of the scaffold were released out. **(D)** A cross-sectional image after cutting the co-cultured ICC scaffold with a razor blade shows decreasing thymic epithelial cell density moving into the inside of the ICC scaffold. Monocytes were distributed the whole ICC scaffold and similar number of cells were entrapped at each pore.

Co-cultured hydrogel ICC scaffolds were dehydrated and observed under SEM. The dehydration process deformed the structure, which is the reason for dimensional differences compared to the confocal images. It was found that the scaffold exterior was covered densely with thymic epithelial cells, and their population reduced the inward movement of other epithelial cells. (Figure 5.7A) Secondly, epithelial cells migrated between pores through interconnected channels, and some colonies expanded over

several pores. (Figure 5.7C) Thirdly, a few suspension cells were entrapped inside when they were observed at the interior of the scaffold in SEM cross-sectional images. (Figure 5.7B) It suggests that monocytes travel deep into the ICC scaffolds while temporarily entrapped in an ICC pore before moving into neighboring pores due to the finite size and number of interconnecting channels.

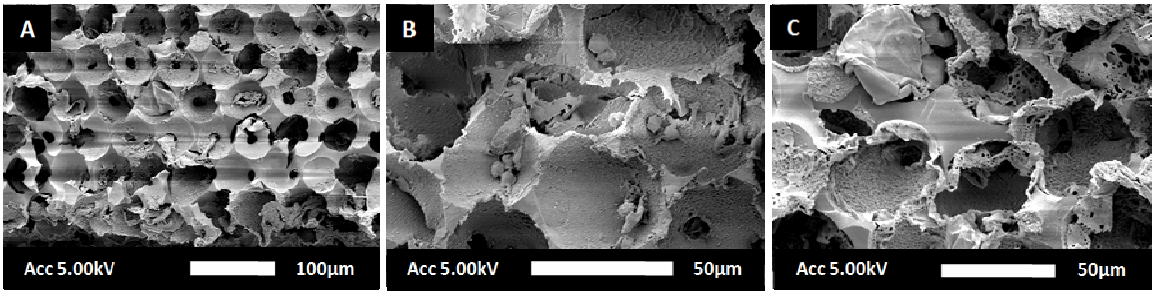

Figure 5.7 SEM images of 3D co-cultured ICC scaffolds (A) Cross-sectional image of the scaffold's interior, **(B)** Entrapped monocytes, and **(C)** Thymic epithelial cells covering pores and channels.

5.4. Summary

A clay/PDDA LBL thin film successfully formed on an ICC scaffold pore surface which in turn significantly improved adhesion and growth of stromal cells. The unique geometry of ICC scaffolds accommodated two different types of cells within a same chamber. Floating cells mimicking HSCs were undergo extensive cell-cell and cell-matrix interactions. Such cellular interactions within the ICC scaffold were demonstrated in both experimental and modeling works. Confocal images clearly showed that two types of cells co-exist in the same pore. Modeling results indicated that entrapped suspension cells spent a significant fraction of time in the vicinity of the ICC chamber wall or the stromal cell layer on the pore surface.

Well controlled multi-scale structures which can build real-size organ systems and generate the essential subcellular morphology, are a key factor for the successful investigation of cell-molecular and cell-cell interactions. It is obvious that the full function of the tissues and organs cannot be recovered without rebuilding the ultra structure of the tissue itself. Proposed ICC scaffolds and surface modification utilizing a LBL technique will be excellent approach for this purpose. ICC scaffold structure generates super- and cellular- scale microenvironment for intense cell contacts with other types of cells or matrix. On this surface, various insoluble signaling molecules such as ECM components, membrane bound receptors and ligands can be incorporated through a LBL method which can produce subcellular, nanoscale resolution environment for cellular receptor-molecular interactions. In particular, this could greatly facilitate the study of B and T cell development from the stem cells which requires understanding and controlling precise 3D molecular interactions.

CHAPTER VI

ENGINEERING PRIMARY LYMPHOID TISSUES

6.1. Introduction

Development of *in vitro* human HSC niches that can recapitulate the bone marrow and thymus function is imperative for understanding the fundamental biology of human hematopoiesis because most information on HSC self-renewal and lineage commitment has been based primarily on murine studies. Although rodent studies have provided important fundamental insights into hematopoietic development, there is much that can be learned regarding human hematopoiesis through the use of *in vitro* human hematopoietic systems that are unavailable in non-human models. For instance, such established functional tissue analogues can greatly serve as a valuable tool to identify specific signaling factors and their precise roles in hematopoiesis by systematically manipulating major experimental parameters. *In vitro* production of human HSCs and lymphocytes are also clinically important for the development of immune therapeutics such as monoclonal antibodies and cancer vaccines. Besides that, artificial analogs of primary lymphoid tissues can considerably accelerate the testing of a variety of types of drugs.

However, construction of *ex vivo* analogs of lymphoid tissues is quite challenging since hematopoiesis is a complicated and tightly regulated process involving multiple

signaling factors.[279] (Figure 6.1A) Still the precise nature of HSC self-renewal and differential niches remains uncertain. Nevertheless, recent research efforts have discovered that supporting stromal cells and 3D ECM microenvironments are important in directing HSC self-renewal and differentiation. Here, stromal cells play a critical role in both presenting membrane bound ligands and secreting soluble signaling proteins[279-288]. 3D ECM microenvironments coordinate cellular interactions between HSCs and stromal cells as well as spatio-temporal delivery of various signaling molecules to the cells[279, 287]. (Figure 6.1B)

Although the native bone marrow environment can be recreated on 2D culture to some extent by the addition of proper growth factors and by the presence of co-cultured stromal cells, it is inefficient for the purpose of replicating hematopoiesis to produce functional leukocytes. Utilizing 3D cell scaffolds that induce more intensive cell-cell contacts between HSCs and stromal cells appears promising to provide the appropriate developmental niches[289-291].

Similarly, three-dimensionally organized thymic stromal cells create a distinctive intrathymic 3D microarchitecture which coordinates the various signaling milieus.[292-294] Thymocytes passing through the interstices of the 3D network of thymic stroma undergo extensive physical contacts with stromal cells that is the main mechanisms to promote T-cell differentiation and maturation. Due to such complexity, until recently the only reliable *in vitro* culture model for the successful T-cell differentiation was the fetal thymus organ culture (FTOC) which is composed of a three-dimensionally reaggregated dissection of fetal thymic tissues.[295-297]

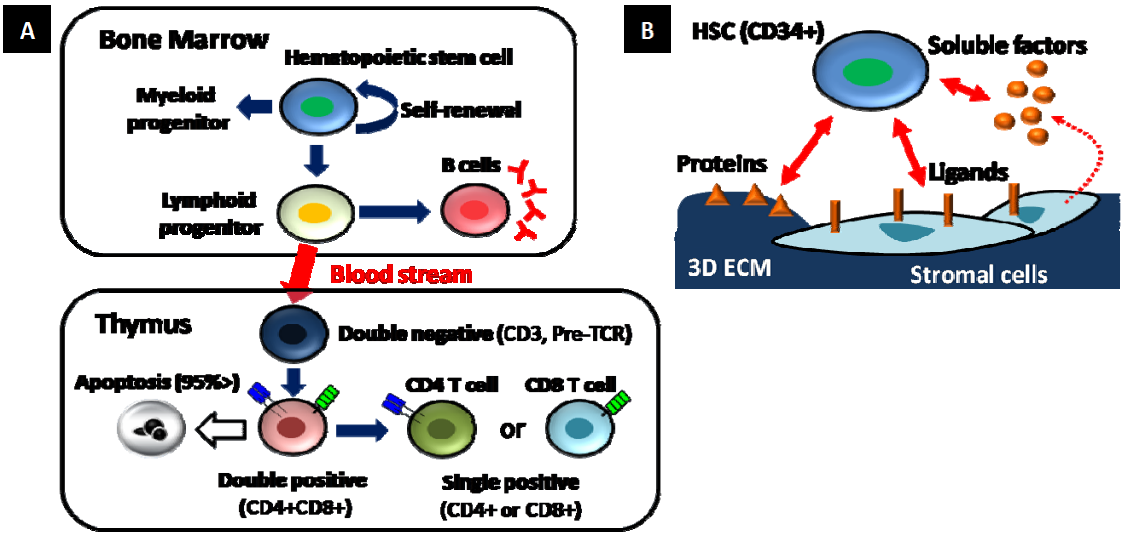

Figure 6.1 Schematics of hematopoiesis and hematopoietic stem cell niches. **(A)** Hematopoiesis focused on B-/T-lymphocytes differentiation in primary lymphoid tissues and **(B)** Components consisting HSC niches.

One of the difficulties in the development of a bone marrow and thymic analog is the availability of a suitable 3D matrix, which must possess sufficiently large surface area for cell attachment, high porosity for cell migration and transport of nutrients, substantial transparency for inspection of constructs with optical techniques, and variability in scaffold structure to control cell-to-cell contacts. Even though various types of 3D matrices have been introduced for this purpose, their approaches remain largely empirical rather than systematic due to limited controllability and reproducibility of microscale structures. For that reason, there has been little attention to the design of pore geometry that can effectively mimic the functional 3D microenvironments.

In this chapter, ICC hydrogel scaffolds combined with a LBL surface engineering technique applied to create artificial human primary lymphoid tissues. ICC scaffold design clearly exhibited marked advantage of 3D organization for hematopoiesis and resulted in acquisition of structural requirements critical for a successful bone marrow and thymus

analog. (Figure 6.2) Regarding bone marrow niche, it was demonstrated that 3D dynamic co-culture model is capable of supporting substantial expansion of CD34+ HSCs and B-lymphocyte differentiation, two main functions of bone marrow. Production of functional B-cells was substantiated by enhanced secretion of immunoglobulin after exposing the culture to lipopolysaccharide (LPS).

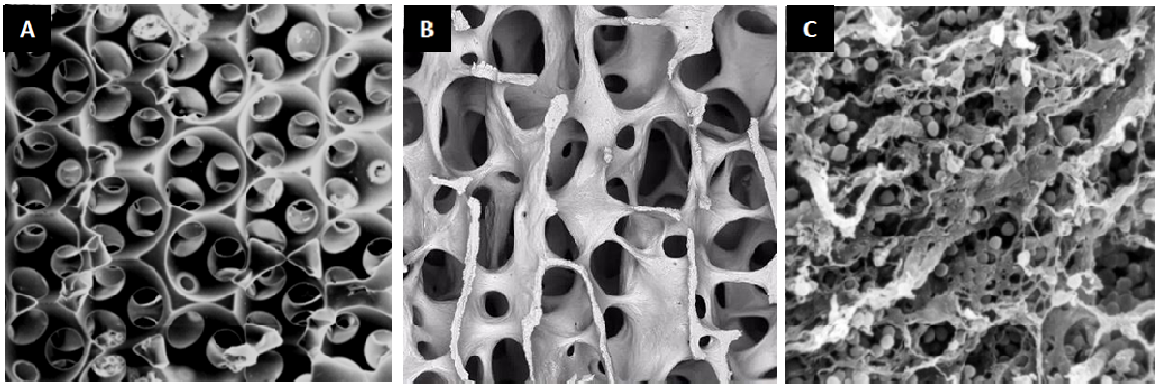

Figure 6.2 Morphological comparison ICC geometry and supporting bone marrow and thymic tissues. (A) ICC geometry, **(B)** Bone marrow, and **(C)** Thymic tissues.

In terms of thymic niche, it focuses on notch signaling, an essential cell-cell signaling pathway promoting T-cell differentiation[298]. Specifically 3D micro-architecture and notch ligand effects were combined utilizing LBL surface coating technique under the hypothesis that 3D ICC scaffolds coated with DL-1 notch ligand would considerably substitute for the structure and function of thymic stromal in addition to essential cytokines. The effectiveness of 3D ICC topology and the bioactivity of LBL-immobilized DL-1 notch ligands in *ex vivo* T-cell development of human HSCs were investigated.

6.2. Materials and Methods

6.2.1. ICC scaffold preparation

CCs were prepared with PS beads (D=100μm) following the previous method. Final scaffolds have 6.5mm diameter and 0.5-1mm thickness. All pores are open to the outer fluid which facilitates cell motility and media exchange in a dynamic culture condition.

6.2.2. Bone marrow niche preparation

Clay-PDDA multilayer preparation

The surface of ICC hydrogel scaffolds was coated with Clay and PDDA following the LBL surface coating procedure in Chapter 5. The LBL coating was started with a PDDA layer and finished with a Clay layer.

Bone marrow stromal cell culture

Human bone marrow stromal cells HS-5 (CRL-11882, ATCC) were cultured with DMEM with 4mM L-glutamine, 4.5g/l glucose, 1.5g/l sodium bicarbonate, 10%(v/v) FBS, and 1%(v/v) penicillin-streptomycin. Human fetal osteoblasts hFOB 1.19 (CRL-11372, ATCC) were maintained with 45% Ham's F12 medium, 45% DMEM, 10% FBS and 1% antibiotic. Once cell growth reached approximately 80% confluence, they were detached from the culture flask using 0.25%(v/v) Trypsin-EDTA solution and 10^5 cells were seeded on top of UV sterilized scaffolds. In order to characterize stromal cell growth in 3D scaffolds, HS-5 cells were stained with 5μM CFSE dye (Invitrogen). The cells growing within ICC scaffolds were imaged under a Leica SP2 confocal microscope with 20x objective.

Human CD34+ HSCs isolation

Peripheral bloods were obtained from Gulf Coast Blood Bank or from donors (18-50 years of age) after informed consent under protocols that were reviewed by the Institutional Review Board of The University of Texas Medical Branch. Cord blood and bone marrow were purchased from Lonza Inc. (Allendale, NJ). The mononuclear leukocyte (MNL) fraction was isolated from these three CD34+ HSC sources using Ficoll density gradient separation medium (Amersham-Biosciences, NJ). CD34+ HSCs were enriched by counter current centrifugal elutriation of MNLs in a Beckmann J6M elutriator (Beckman Instruments, USA) using a Sanderson chamber. A Masterplex peristaltic pump (Cole Parmer Instruments) was used to provide the counter current flow. RPMI 1640 supplemented with 2mM glutamine, 100units penicillin G and 100µg/ml streptomycin and 10% heat inactivated defined fetal calf serum (Hyclone, Logan, UT) was used as elutriation medium. 3~6 x 10^6 cells were loaded at 3000rpm and HSCs were isolated using a step-wise reduction of rotor speed until the appropriate cell diameter population, 6-7 µm, of CD34+ enriched cells was collected.

Immunophenotypic analysis of elutriation with 5-7 µm diameter HSCs at the time of isolation and seeding of the scaffold showed that these cells were lin-1 mature leukocyte marker negative, CD34+ cells were further purified by negative selection of any remaining lin-1 positive or mature cell types using Dynall magnetic beads or by flow cytometric cell sorting using a FACSaria cell sorter.

Human CD34+ HSCs expansion

CD34+ cells were labeled with the CFSE dye as previously described[299]. Prestained 1-4x10^4 CD34+ HSCs in 50µl DMEM containing 5% pluronic F-127 were seeded in ICC scaffolds. A total of 3~5 scaffolds were placed in a standard 2 or 10ml

culture vessels mounted on a rotary bioreactor with a rotational speed at 5rpm. In a subset of experiment, the scaffolds were seeded with stromal cells from human bone marrow aspirates. After 3 days of stromal culture, non-autologous CD34+ HSCs were introduced to the culture vessel. HSC/stromal cell co-cultures were also incubated in plastic Petri dishes in order to compare 2D versus 3D cell cultures.

Inducing B-Cell differentiation

In order to induce B-cell differentiation, CD34+ cells were co-cultured with primary cell lines from bone marrow aspirates which included cells positive for CD105(100%), CD166(100%), CD44(95%), CD14(1%), CD34(1%) and CD45(<1%). Considering these surface markers, they were part of the stromal cell population and at least one cell type of them was actually of osteoblasts lineage as it was positive for osteonectin. These primary stromal cells formed densely populated layers similar to natural bone marrow and replicated the actual bone marrow stroma better than the feeder layer made from a single cell type. Growth factors used to promote hematopoiesis included interleukin (IL)-2 (5ng/ml), IL-7 (20ng/ml), Flt3 ligand (20ng/ml), stem cell factor-1 (SDF-1) (20ng/ml), BMP-4 (4ng/ml) and IL-3 (10ng/ml). Additives used to promote development of a B-lymphocyte lineage included soluble CD40L (5ng/ml), IL-4 (10ng/ml), IL-5 (10ng/ml), IL-6 (10ng/ml), IL-10 (10ng/ml), IL-2 (5ng/ml), IL-7 (20ng/ml), Flt3 ligand (20ng/ml), stem cell derived factor (20ng/ml), IL-3 (10ng/ml) and agonist anti-CD40 mAb (5μg/ml).

To activate B-lymphocytes and induce plasma cell formation, cultures were exposed to 3.5μg/ml LPS. Secreted IgM in supernatant fluids from 2D and 3D cultures was quantitated using a human IgM ELISA assay (Diagnostic Automaton Inc.) as described by

the manufacturer. All samples were run in triplicate and averaged optical densities (OD) at 450nm were compared to a standard curve using optical densities obtained for each of the standards.

6.2.3. Thymic niche preparation

Delta-like-1 notch ligand presenting complex LBL preparation

First, the surface of hydrogel ICC scaffolds was coated with five bi-layers of clay and PDDA following the protocol in Chapter 5. Both starting and finishing layers were PDDA. Engineered DL-1 notch ligands consisted of the extracellular domain of Delta 1 ligand fused to the Fc domain of human IgG was gifted from Prof. Irwin Bernstein‘s lab (University of Washington). Monolayer of DL-1 notch ligand coating was prepared on top of the Clay-PDDA film by immersing the scaffold in a 10μg/ml of DL-1 notch ligand solution for 30 minutes. For imaging purpose, the Fc portion of DL-1 notch ligands was bound with secondary antibodies conjugated to FITC before using.

Cell culture

Fresh unprocessed 25ml of human bone marrow was purchased from Cambrex. Mononuclear cells were isolated by utilizing a density gradient centrifugation in Ficol-Paque solution (GE Healthcare) at 400xG for 30 minutes. Mononuclear cells derived from human umbilical cord blood cells were gifted from Prof. Larry Lasky’s lab (Ohio State University). For CD34+/CD4- HSC culture, CD4+ cells were depleted first from the mononuclear cells and then isolated CD34+ cells utilizing magnetic activated cell sorting kits (MACS) (Milteney Biotech). Approximately 1~1.5x10^6 CD34+/CD4- HSCs were collected. Isolated mononuclear cells and HSCs were cultured in serum-free medium (StemSpan: Stemcell Technologies) supplemented with 20ng/ml of Flt-3 ligand,

Stem Cell Factor, and Thrombopoietic (Stemcell Technologies). Five scaffolds were put in a 10 ml rotary cell culture vessel and approximately $0.2x10^6$ HSCs were seeded in each vessel. The rotary culture was maintained at 15rpm for 4 weeks and culture medium was changed in every 3 days. Experiment repeated three times and similar results were obtained.

Characterization

Cellular morphology and distribution within ICC scaffolds were characterized under SEM (FEI Nova NanoLab). HSCs-ICC scaffolds were fixed with 2.5% glutaraldehyde solution overnight and dehydrated through a series of ethanol solutions. Dehydrated samples were further freeze dried and then coated with gold using a sputter coater. Differential stage of HSCs was determined by surface markers analysis. HSCs growing ICC scaffolds were fixed with 4% formaldehyde and blocked with 10% normal goat serum to prevent non-specific binding of antibodies. Primary antibodies CD34, CD117, CD4, CD7, CD8 and TCRα (Santa Cruz biotechnology) diluted in blocking solution were applied for one hour. After washing, diluted secondary antibodies conjugated to Alexa fluro 488 and 568 dyes (Invitrogen) were introduced for one hour. The antibody stained scaffolds were visualized under confocal microscope (Leica SP2) with 10x and 20x objective.

6.3. Results and Discussion

6.3.1. Bone marrow niche for *ex vivo* HSC expansion

The two basic functions of the bone marrow are self-renewal of an undifferentiated population of HSCs and production of fully functional B-lymphocytes.[300] Artificial bone marrow construction starts with isolating HSCs. However, surface antigens exclusively presented in HSC are not discovered yet, so the combination of multiple surface markers such as CD34, CD38, Lin, CD90, and CD117 have been commonly used to identify and isolated them from mixture of blood cell populations.[301] Among them CD34 is the most commonly accepted surface marker in enriching HSCs, since the clinical importance of CD34 cells has been extensively reported in bone marrow transplantation.[302-304] Obviously a significant portion of CD34+ cells includes HSCs having a long term multi-lineage engraftment capability.

CD34+ HSCs were isolated from human peripheral blood, umbilical cord blood or bone marrow. All cells were positive for CD34 and were lineage-1 (lin-1) negative when seeded onto the scaffolds. A small portion (1-2%) of CD34-expressing cells was positive for CD150, a cell marker also associated with long term multi-cell lineage reconstitution in irradiated mice[286]. Analogous cultures were also made on 2D plates to establish the importance of the 3D geometry in ICC scaffolds.

Throughout this study ICC hydrogel scaffolds having 100μm of pore diameter and 20-30μm of channel sizes were mainly used. These diameters were chosen because they provide efficient contacts between adhesion and dispersion cells, and allows for natural cell migration through the channels between the cavities, which is imperative for replication of hematopoietic tissues. To provide adequate adhesion of bone marrow

support cells, hydrogel matrixes were coated by clay/PDDA multilayer following the LBL technology in Chapter 5. Once stromal layer formed, CD34+ HSCs were introduced and the co-culture maintained in a dynamic culture condition utilizing a rotary cell culture system. (Figure 6.3)

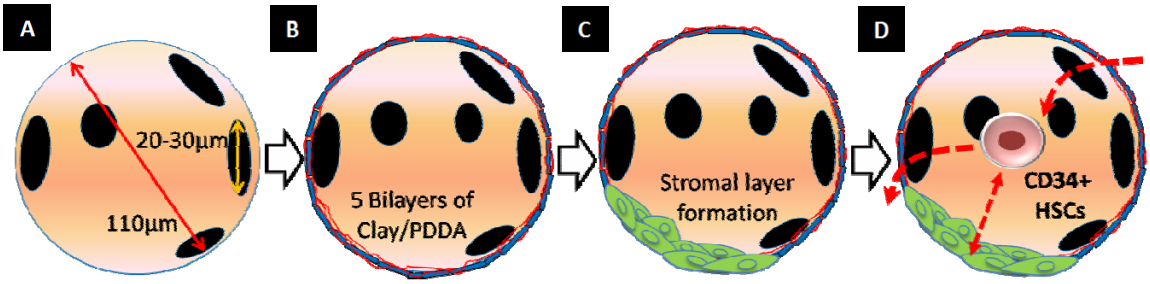

Figure 6.3 Schematic of 3D co-culture model for bone marrow niche. (A) Optimized pore (D=110µm) and channel (D=20-30µm) size for HSC (D=5~10µm) culture **(B)** 5 bilayers of Clay/PDDA LBL film to support stromal cell adhesion **(C)** Stromal cells were seeded and cultured for three days to allow stromal cell layer formation **(D)** Introduce CD34+ cells and co-culture maintains under dynamic condition.

Bone marrow stroma is comprised of a complex reticulum containing hematopoietic precursors, as well as non-hematopoietic cells such as fibroblasts, epithelial cells, nerve cells, reticular cells, adipocytes and osteoid cells[280-283, 288, 305]. It is unknown how many or all of these cell types may be necessary to support the development of fully functional leukocytes. To mimic the bone marrow stromal tissue function, human bone marrow stromal cells were seeded on scaffolds and cultured for three days which allows the formation of a support cell layer on the scaffold surface prior to the addition of CD34+ cells. Figure 6.4 shows typical confocal images of stromal and HSC co-cultured ICC scaffolds.

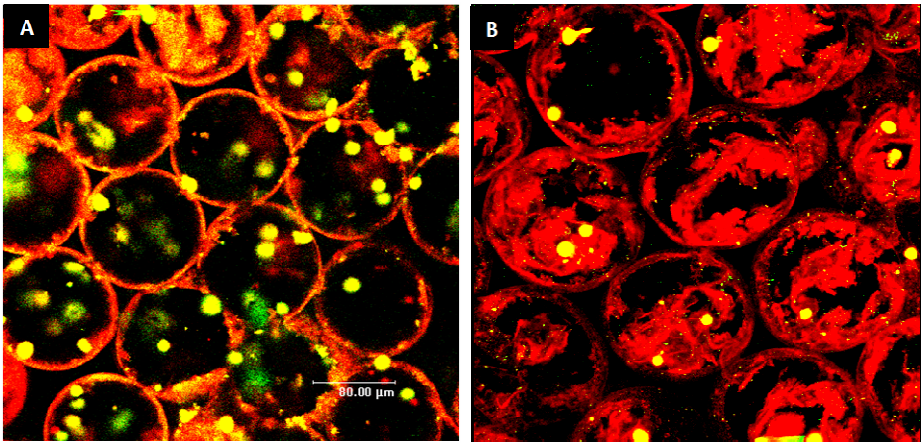

Figure 6.4 3D co-culture of stromal cell and HSCs. Red is bone marrow stromal cells were stained with a red dye and CD34+ HSCs were observed as yellow dots. **(A)** 2D section and **(B)** 3D reconstructed images.

Examination of ICC cultures on day 28 showed the continued presence of CD34+ HSCs. There was also formation of numerous actin-rich cell processes, which were absent in cell cultures on flat substrates. Similarly, maintenance of a population of CD150+ cells was seen in ICC matrices but not in donor matched 2D cultures after 28 days. Data from flow cytometry show that there were significantly higher percentages of CD34+ cells in ICC cultures after 28 days, regardless of the original cell source, when compared to 2D plate cultures. (Figure 6.5B) This proves that an undifferentiated population of CD34+ cells was maintained over time and demonstrates the importance of the chosen 3D ICC organization of the cell cultures for replication of reproductive functionality of bone marrow. Active proliferation of HSC was also seen from observation of mitotic figures and analysis of loss of CFSE fluorescence intensity. (Figure 6.5A) Overall, ICC scaffolds demonstrate substantially more CD34+ proliferation than plate cultures.

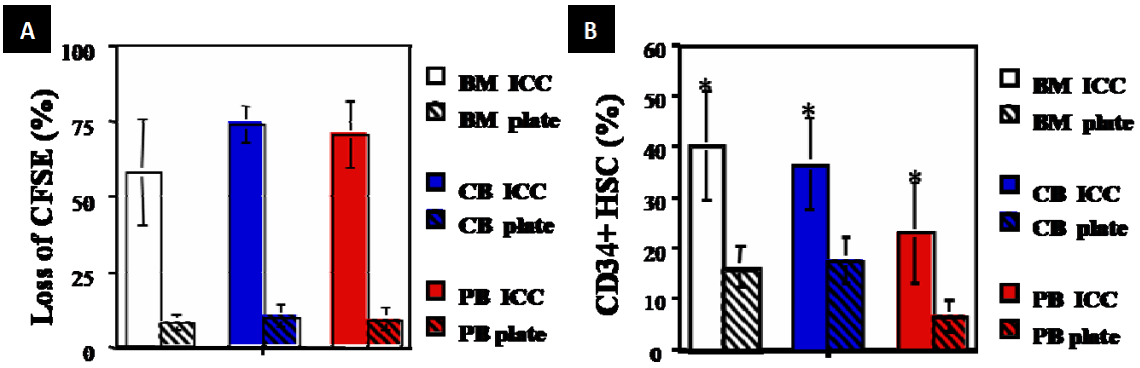

Figure 6.5 Characterization *ex vivo* expansion of HSCs in 2D and 3D co-culture model on day 28 (A) Significantly more CD34+ cells were seen in ICC cultures for (BM) (P=0.01), cord blood (CB) (P=0.004), or peripheral blood (PB) (P=0.03) than for donor matched 2D plate culture. (n=6) **(B)** Comparison of 2D versus 3D cell cultures in ICC scaffolds by HSC proliferation analysis using CFSE loss for CD34+-derived from BM, CB or PB. (n=5)

Although CD34+ cells hold great potential in various biomedical research and clinical practice, their practical usage has been significantly limited primarily due to the low number. Normally CD34+ cells comprise only 5% of total cell population in the bone marrow where is the best-known location for HSCs.[306] For sufficient engraftment and good clinical outcome 2-5 million of CD34+ cells should be transplanted.[306] However, in many cases, obtaining such a large quantity of CD34+ cells from the donor is difficult. For that reason, development of *ex vivo* system that can effective expand CD34+ cells has been desired in order to improve clinical transplantation.

Besides effective bone marrow transplantation, the development of artificial bone marrow analogue that can continuously produce CD34+ cells is also imperative in drug discovery applications. For example, currently immune responses of drug molecules in the human body, particularly HSC activity in the bone marrow, cannot be estimated simply due to the absence of *in vitro* model system which recapitulates bone marrow functionality. Therefore, functional bone marrow analogue can be directly used for

screening immune toxicity of drug candidate compounds in a preclinical stage. In addition, it can potentially serve as a platform for developing leukemia drug that can regulate HSC activity which in turn simulates the production of immune cells.

6.3.2. Bone marrow niche for *ex vivo* B-cell differentiation

Bone marrow is also the site of long term antibody production after viral infection[305] and bone marrow stroma has been shown to play a role in plasma cell life cycle[264]. Similar to the maintenance of HSCs populations, the production of B-cells is an essential component for the development of *ex vivo* bone marrow, immune system studies, development of human monoclonal antibodies, drug evaluation, and disease treatment. B-cell development involves a series of stages where close 3D contact between bone marrow stroma and the developing B-cell is critical and hard to realize in 2D plate cultures.

To assess the ability of the artificial bone marrow constructs to produce functional immune cells, B-lymphocyte production was focused since B-cells normally undergo the process of differentiation (as well as negative and positive selection) in the bone marrow.[282, 283, 307, 308] After three days of culture, ICC/stromal cell constructs containing growth factors to drive the B cell production were seeded with CD34+ HSCs. Cell cultures were examined for stage-specific markers of development and functionality on days 1, 7, 14, 28 and 40. ICC cultures showed nuclear specific expression of recombination activating gene 1 protein (RAG-1) by day 7, cell surface IgM by day 14, and co-expression of IgM with IgD by day 28 confirming differentiation of CD34+ into mature antigen naive B lymphocytes. (Figure 6.6A) In a separate comparative experiment,

more of the differentiating cell population were observed to express CD40 (P=0.0002) and IgM/IgD co-expression (P=0.021) in donor matched ICC cultures than in 2D cultures. (Figure 6.6B)

These results show the expression of phenotypic cell surface markers of B-cells, which is an important step in development bone marrow replicas; however, this fact does not necessarily prove the functionality of the *ex vivo* generated B-lymphocytes. To evaluate the ability of these B-lymphocytes to respond to mitogenic or antigenic stimulation and fully mature into antibody producing cells, B-lymphocytes isolated from 28 day ICC scaffold constructs and donor matched plate cultures were exposed to bacterial LPS, a major structural component of the outer wall of gram-negative bacteria and initiator of immune response to bacterial infection. Secreted IgM was quantified using a human IgM ELISA for all B-cell cultures differentiated from CB-derived, PB-derived and BM-derived CD34+ cells. Significantly higher levels of IgM were produced from B-lymphocytes generated in the ICC scaffold regardless of the initial source of the CD34+ cells. (Figure 6.6C)

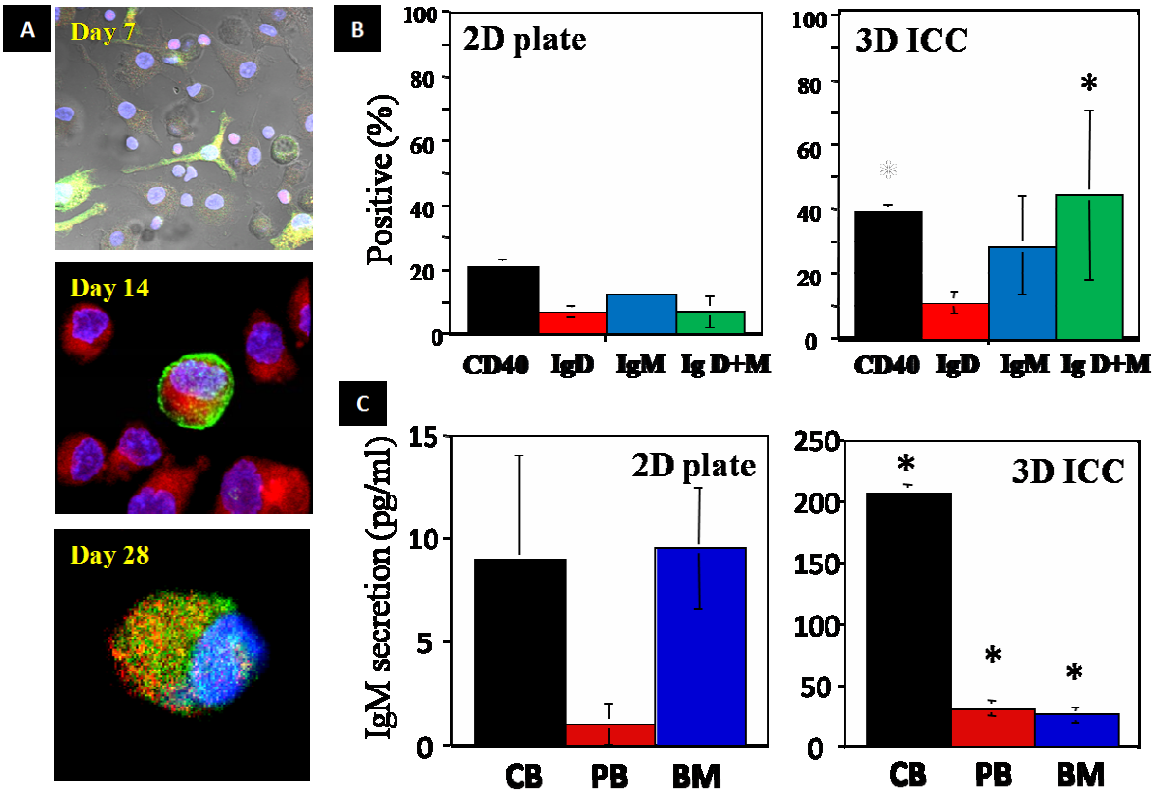

Figure 6.6 Characterization of B-cell differentiation from the 3D co-culture model (A) Confocal microscopy images of 7µm sections of hydrogel scaffolds supporting CD34+ HSCs from cord blood. DAPI nuclear stain is blue for all images. ***(Top)*** Nuclear RAG-1 (red) expression and surface expression of IgM (green), day 7, 200X. ***(Middle)*** Cell surface co-expression of CD19 (red) and IgM (green), day 14, 630X. ***(Bottom)*** Co-expression of cell surface IgM (green) and IgD (red) day 28, 630X. **(B)** The average expression of CD40, IgM, IgD and IgM + IgD co-expression for plate and ICC cultures using CD34+ from cord blood. (n=6) **(C)** Comparison of IgM production for LPS stimulated plate and ICC cultures from CB, PB or BM derived CD34+ HSCs.

6.3.3. Stromal cell free 3D culture system

Recent advances of biomaterial-process engineering enabled the recapitulation of the hematopoietic process to some extent on biomaterial-based *in vitro* culture environments.[309] Simple and directed preparation of artificial microenvironments was exceptionally beneficial to improve experimental controllability and reproducibility. It also allowed the systematic manipulation of experimental parameters which in turn deepen the fundamental understanding of thymic signaling effects. For instance, 3D co-culture models of thymus established on 3D scaffolds significantly promoted T-cell differentiation of HSCs compared to the conventional monolayer cultures.[289, 310] In addition, these studies highlighted the importance of the proper design of a 3D scaffold to obtain the optimum range of pore size and density so as to maximize *ex vivo* HSC development. Nevertheless, 3D co-culture models retain several critical drawbacks: (i) difficulty in control the growth of stromal cells in 3D substrates; (ii) required an extra step to isolate a pure population of HSCs when the culture needs to be characterized; (iii) potential phenotypic change of feeder cells due to enhanced cell-cell and cell-matrix interactions in 3D culture condition.

A different promising approach was stromal cell-free T-cell differentiation which presents multiple advantages such as better control over cell interactions and signaling, and efficient isolation and characterization of HCSs. Currently the most successful system is utilizing engineered delta-like 1 (DL-1) notch ligands in addition to essential cytokines.[311-313] Notch signaling is a major cell-cell signaling pathway determining HSC fate in the bone marrow and thymus.[298] The signaling is activated when a notch receptor on HSCs directly contacts the Delta and Jagged families of notch ligand present

on the stromal cell membrane. (Figure 6.7A) The expression of ligands and receptors is tightly regulated to balance between self-renewal and differentiation of HSCs in the bone marrow, and to promote T-cell lineage commitment and maturation in the thymus.[314, 315] The importance of notch signaling in T-cell development was demonstrated with 2D *ex vivo* co-culture model of HSCs and OP9-DL1 stromal cells expressing the DL-1 notch ligand.[316] For example, the OP9-DL1 cells successfully supported T-cell differentiation of HSCs, whereas regular OP9 cells only induced B-cell differentiation. [317, 318] Although these *in vitro* culture models greatly contributed to the understanding of HSC biology, their purely biological nature presents inherent limitations including technically burdensome preparation, low yields, and highly variable outcomes.

Recently DL-1 notch ligands were successfully synthesized from genetically engineered microbes which made possible thymic stromal cell free T-cell development. For instance, individual DL-1 notch ligands immobilized either by physical absorption on the bottom of a well-plate[311, 312, 319] or by chemical conjugation to micro-carriers[313] successfully supported T-cell development. Moreover, the readily adjustable ligand density of this technique distinguished the different effect of notch signaling intensity to determine the fate of HSC differentiation.[312, 320, 321] Notch ligand presenting acellular microenvironments are attractive approach to create *in vitro* HSC niches in a convenient and consistent manner; however, it has remained in only 2D substrates, probably due to the absence of suitable 3D substrates and coating techniques.

In this section, DL-1 notch ligand effects were extended to the ICC scaffold utilizing a LBL surface engineering technique under the hypothesis that 3D scaffolds

coated with DL-1 notch ligand would considerably substitute for the structure and function of thymic stroma in addition to essential cytokines. (Figure 6.7B)

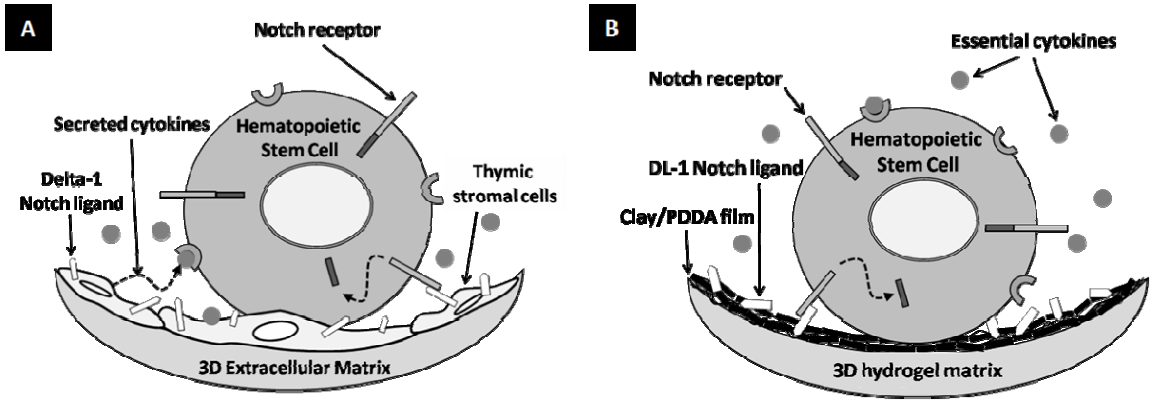

Figure 6.7 Schematic of stromal cell free approach (A) In the thymus, three-dimensionally organized thymic stromal cells present membrane bound notch ligands and secrete soluble cytokines for the T-cell differentiation of HSCs. **(B)** ICC topology provides 3D intrathymic microstructure and the multi-component LBL film (i.e. monolayer of DL-1 notch ligands on top of five bilayers of clay/PDDA film) substitutes thymic stromal cell functions in addition to soluble cytokines.

The same pore and channel dimensions of ICC scaffolds were utilized in this study. The surface of hydrogel scaffolds was coated with five bilayers of Clay/PDDA following the previous method. Then, a monolayer of DL-1 notch ligand was prepared on top of clay/PDDA film instead of seeding stromal cells. The pre-deposited clay/PDDA multilayer provided better environment for the following DL-1 notch ligand immobilization as increasing surface charges of the hydrogel surface. Finally CD34+ cells were introduced and then the culture was maintained in a rotary cell culture vessel up to 4 weeks. (Figure 6.8)

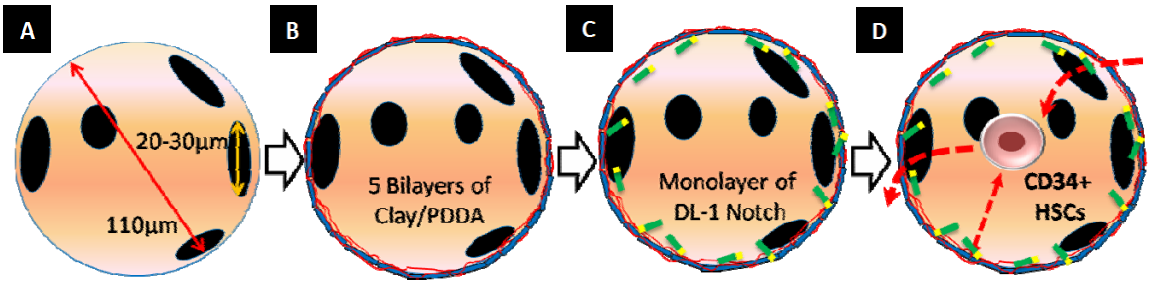

Figure 6.8 Schematic of stromal cell free 3D culture model for thymic niche (A) Optimized pore (D=110µm) and channel (D=20-30µm) size for HSC (D=5~10µm) culture **(B)** Five bilayers of Clay/PDDA LBL film to support stromal cell adhesion **(C)** Monolayer of DL-1 notch ligand coating on top of clay/PDDA layer **(D)** Introduce CD34+ cells and the culture maintains under dynamic condition.

The LBL process created a homogenous 3D artificial thymic layer in a short time compared to the previous 3D co-culture model which normally took several days to reach a confluence on 3D ICC scaffolds. To characterize the quality of 3D LBL coating, the Fc portion of the ligand was tagged with a secondary antibody conjugated to a fluorescent dye before coating and visualized under confocal microscope. As shown in Figure 6.9B, DL-1 notch ligands were well coated on the surface of ICC scaffold but slightly weaker fluorescent intensity was observed inner side pores which would be caused by the relatively less diffusive environment of interior pores.

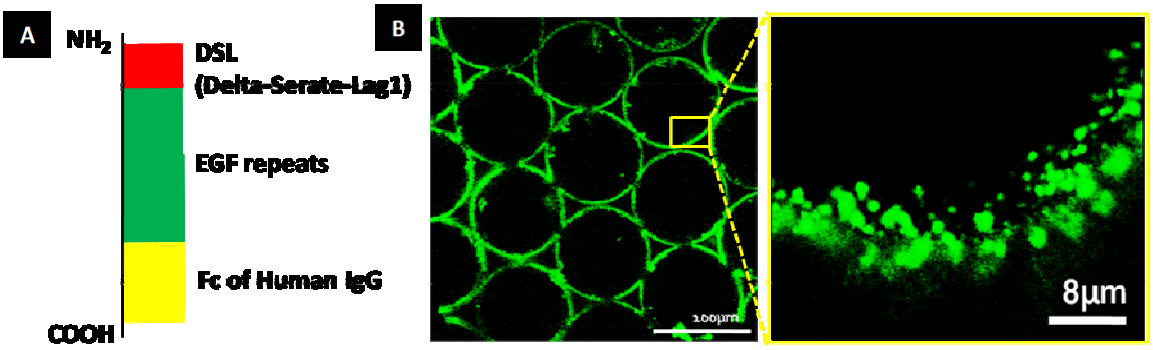

Figure 6.9 Structure of DL-1 notch ligand and LBL immobilization (A) Schematic of engineered DL-1 notch ligand structure. **(B)** Confocal images of DL-1 notch ligand coated ICC hydrogel scaffold. For imaging purpose, DL-1 notch ligands were bound to antibodies conjugated to FITC.

The LBL adsorption technique affords the scaffolds to retain high stability and activity of the notch ligands since the LBL coating is conducted in a mild condition while maintaining pristine protein structures.[322-324] Moreover, the clay/PDDA multilayer promotes immobilized DL-1 notch ligands function in two ways. First, the alternative layer of the inorganic (Clay) and organic (PDDA) composite is mechanically compatible with polyacrylamide hydrogel which supports steadfast immobilization of DL-1 notch ligands. This is an important feature for receptor-ligand based cell signaling because ligands existing in a soluble state, although they can bind to receptors and activate signal transduction, normally undergo rapid internalization into a cell, which in turn considerably reduces the intensity and duration of cell signaling.[325] Other investigators demonstrated that the surface-tethered epidermal growth factor (EGF) more effectively promoted cell spreading and survival than a saturating concentration of soluble EGF due to the longer duration of intense ligand-receptor interactions.[326] Similarly it has been shown that DL-1 notch ligands are required to be immobilized to activate the proper level of notch signaling.[312, 327]

Second, LBL-immobilized ligands can have a moderate level of flexibility because, although individual clay platelets provide local mechanical strength, the overall LBL film provides softness and elasticity found in ECM due to the hydrated polymeric component. It was shown that mechanical properties of a clay/PDDA LBL film are strongly decreased in humid environment.[277] The flexibility of immobilized ligands is essential for the proper development of the ligand docking with the receptor for intracellular signal activation.[328] Hence, the behavior of LBL-coated DL-1 ligands would be quite different when compared to ligands directly adsorbed on a solid surface.

Considering that cellular ligands are actually embedded in a flexible plasma membrane, it is a more realistic and effective approach.

6.3.4. Thymic niche for *ex vivo* T-cell differentiation

First, the ICC topological effect was tested by culturing mononuclear cells derived from bone marrow or umbilical cord blood. As shown in Figure 6.10A, a significant number of cells were observed deep inside of ICC scaffold after 15 days of culture. This demonstrates that the mononuclear cells were deeply transported into the ICC scaffold and the LBL surface modification promoted cell adhesion. Since HSCs are only a small fraction of mononuclear cells (1-2%), most of cells were non-HSCs. However, interestingly I could observe the development of pre-erythrocytes attaching on the pore surface which might be the result of activated notch signaling.[319] In addition, dendritic-like cells scavenging across ICC pores were observed that vividly captured an *in vivo* 3D bone marrow microenvironment. (Figure 6.B)

As a next step CD34+/CD4- HSCs were isolated from mononuclear cells and cultured in the same condition. It is important utilizing CD34+ HSCs to mimic the thymic niches because an initial stage of cellular population entering into the thymus is mostly bone marrow derived HSCs. Moreover, it is necessary to deprive CD4+ cells from the initial cell population to confirm the bioactivity of LBL coated DL-1 notch ligands since notch-1 signaling induces CD4+ T-cell lineage commitment at the late stage of differentiation.[298, 329] In addition, MACS method usually cannot isolate target cells with 100% efficiency. Therefore, CD4+ cells were depleted from mononuclear cells and then CD34+ cells were enriched from there. (Figure 6.11A)

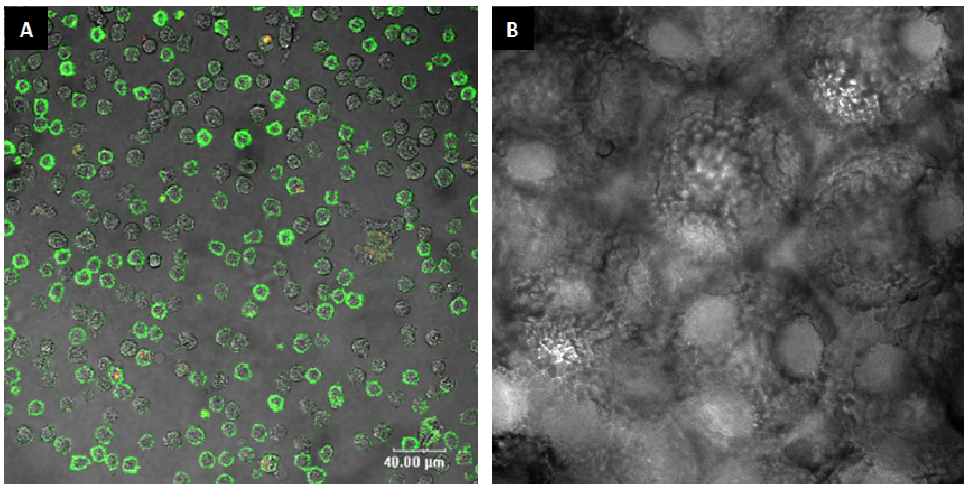

Figure 6.10 Initial cell populations and 15 days culture scaffolds (A) Confocal images after CD4 depletion and CD34 enrichment utilizing a magnetic activated cell sorting method. The initial cell population consists of majority CD34+ and negligible CD4+ cells. (Scale bar is 40µm) **(B)** Typical transmission image of a CD34+/CD4- HSC growing ICC scaffolds after 15 days of culture.

A small diameter of HSCs (< 10µm) readily moved deep into ICC scaffolds and intimately associated with the surface of DL-1 notch ligand coated ICC pores. After 14 days of culture, the pore surface was densely covered with cells. (Figure 6.10C) This result inferred that HSCs proliferated multiple times subsequent to entering into the ICC scaffolds. Notch signaling would be activated on the surface associated HSCs which in turn stimulated T-cell lineage commitment and differentiation. However, it was hard to distinguish differentiated T-lymphocytes from HSCs under SEM due to their similarity in morphology, size and shape. (Figure 6.10D) In the absence of DL-1 notch ligand coating, mononuclear cells readily adhered to the surface of ICC scaffolds which was comparable to the notch ligand coated scaffolds. (Figure 6.10E) However, without clay/PDDA LBL surface coating, hydrogel ICC scaffolds could not support cell adhesion and most of pores appeared empty. (Figure 6.10F) Although a few numbers of cells were entrapped in

the pores during dynamic cell culture, most of them were released out during the sample preparation procedure due to the well-interconnected open porous ICC geometry.

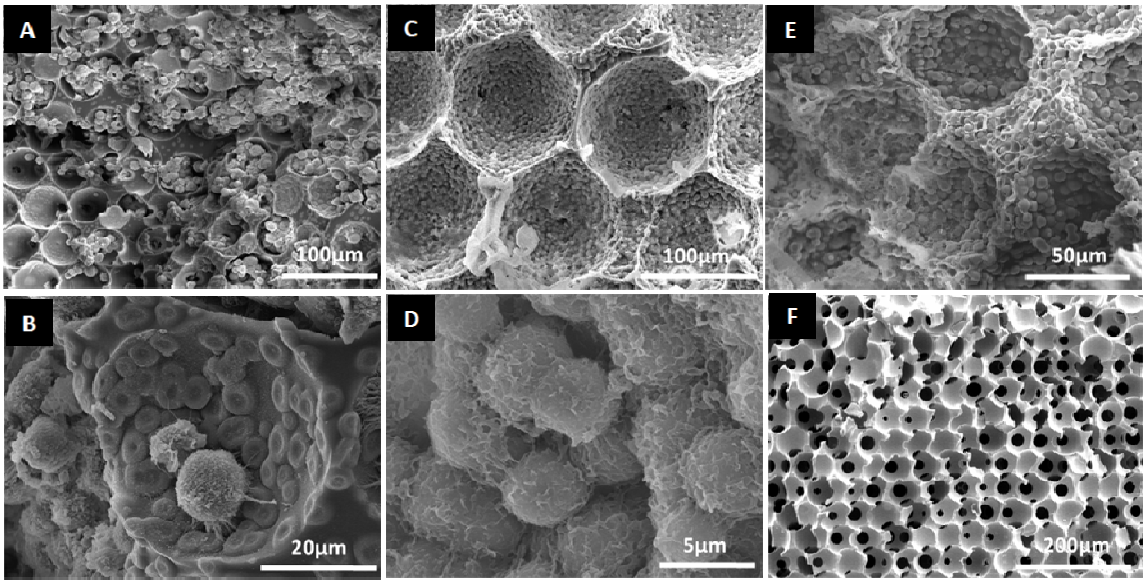

Figure 6.11 SEM images after 15 days of stromal cell free culture. (A-B) Mononuclear cells. **(A)** Various cell types co-existed deep inside of ICC pores. **(B)** Development of pre-erythrocyte associating with the LBL coated surface and migrating dendritic-like cells across pores. It well recapitulated the bone marrow microenvironment. **(C-D)** Isolated CD34+ cells from bone marrow derived mononuclear cells. **(C)** DL-1 notch ligand immobilized pore surface was densely covered with cells. Restricted cellular population mimicked the thymic microenvironment. **(D)** Due to similar morphology and size, it is hard to distinguish developing T-lymphocytes from CD34+ HSCs under SEM. **(E-F)** Control experiments of 15 days cultured CD34+ cells. **(E)** ICC scaffolds could support cell adhesion without DL-1 notch ligand coating. **(F)** However, without clay/PDDA LBL coating (bare hydrogel), ICC scaffolds could not allow any cell adhesion.

In order to confirm T-cell differentiation of HSCs, the progression of differential stage specific surface marker expression was characterized for 4 weeks under confocal microscope. Besides the CD34 molecule, CD117 so called a C-kit receptor is another representative surface marker of primitive HSCs that also maintains the earliest thymocyte progenitors.[26] Examination of ICC cultures on day 15 and 22 showed the continued presence of CD117 which proved that the *ex vivo* 3D culture system successfully supported self-renewal or maintaining undifferentiated population of HSCs.

(Figure 6.12A) In addition, the presence of T-cell receptor (TCR) α and CD3 molecules were observed on day 22 culture. (Figure 6.12B) TCR is a complex of integral membrane proteins consisting of α/β heterodimers associated with CD3 molecules. Pre-TCR expression is one of initial signs in T-cell lineage commitment and development in the Thymus.[296] Therefore, these data substantiate the preserved bioactivity of LBL-coated notch ligands so as to promote pre-T-cell differentiation of HSCs.

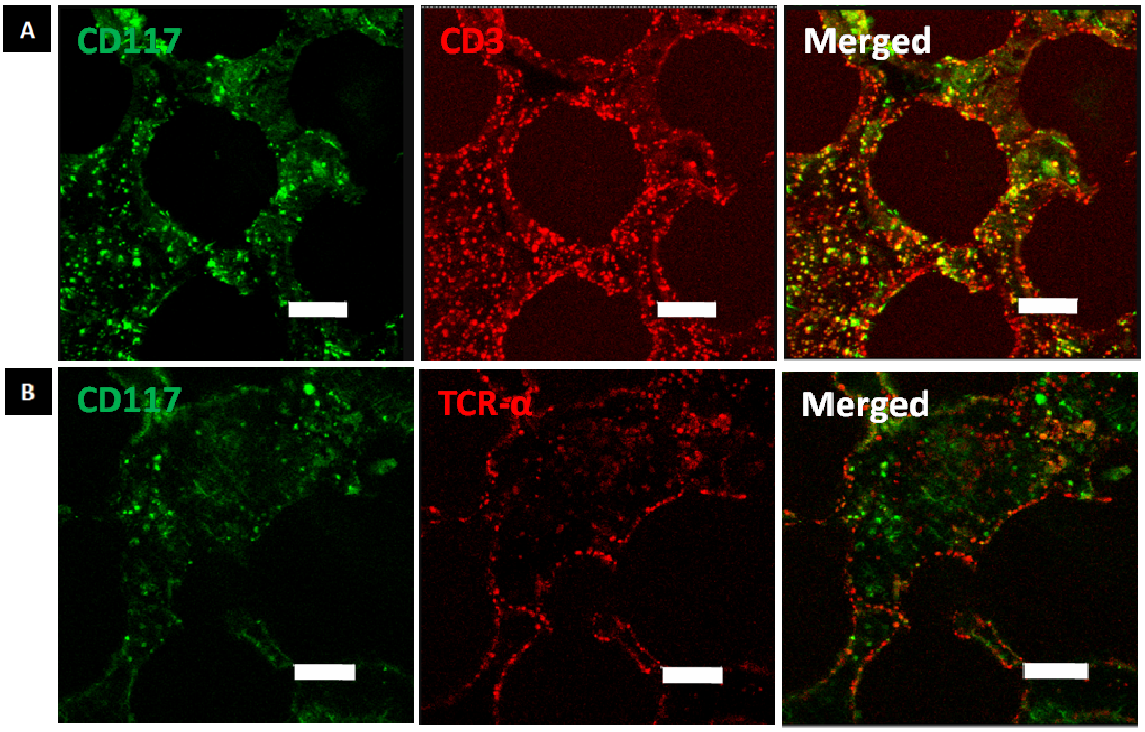

Figure 6.12 Biological effects of LBL immobilized DL-1 notch ligands Representative confocal images of **(A)** CD117 and CD3 after 15 days of culture, and **(B)** CD117 and TCR α after 22 days of culture. (Scale bar is 40μm)

The expression of CD4 and CD8 molecules over the longer period of ICC cultures were further characterized to identify followed double positive and single positive differentiation stages. On 28 days of culture we could observe some CD4 positive but CD8 negative cells. (Figure 6.13A) However, they would not be functional CD4 helper T-cells because in our system the major histocompatibility complex (MHC) molecules;

important factors involved in cell screening processes, i.e. positive and negative selection, were missing. Generally more than 95% of thymocytes undergo apoptosis during the screening processes[26], but we did not observe severe cell apoptosis during the culture. Without DL-1 notch ligand coating, we could not observe either CD4 or CD8 molecules on 28 days of culture. (Figure 6.13B) However, the culture continuously expressed a CD34 surface marker for 14 days which infers that 3D dynamic cell culture stimulates *ex vivo* HSC expansion without notch signaling. Another important thing was that ECM-like molecules progressively developed on the surface of cell/scaffold over the culture period which reduced the quality of surface marker analysis. For that reason, 28 days cultured samples showed relatively weaker fluorescent signals than the samples cultured shorter period of time.

Although the 3D culture model demonstrated promising features to create *in vitro* HSC niches, it was difficult to rapidly isolate large enough number of cells from ICC culture due to strong cellular association with the LBL coated surface and the complex ICC geometry limiting the release of cells. Flow cytometric analysis of individual cells is critical to quantitatively corroborate the study of cell differentiation pathways accompanied with qualitative confocal surface marker characterization. To overcome these drawbacks, the development of effective cell harvesting methods needs to be further investigated.

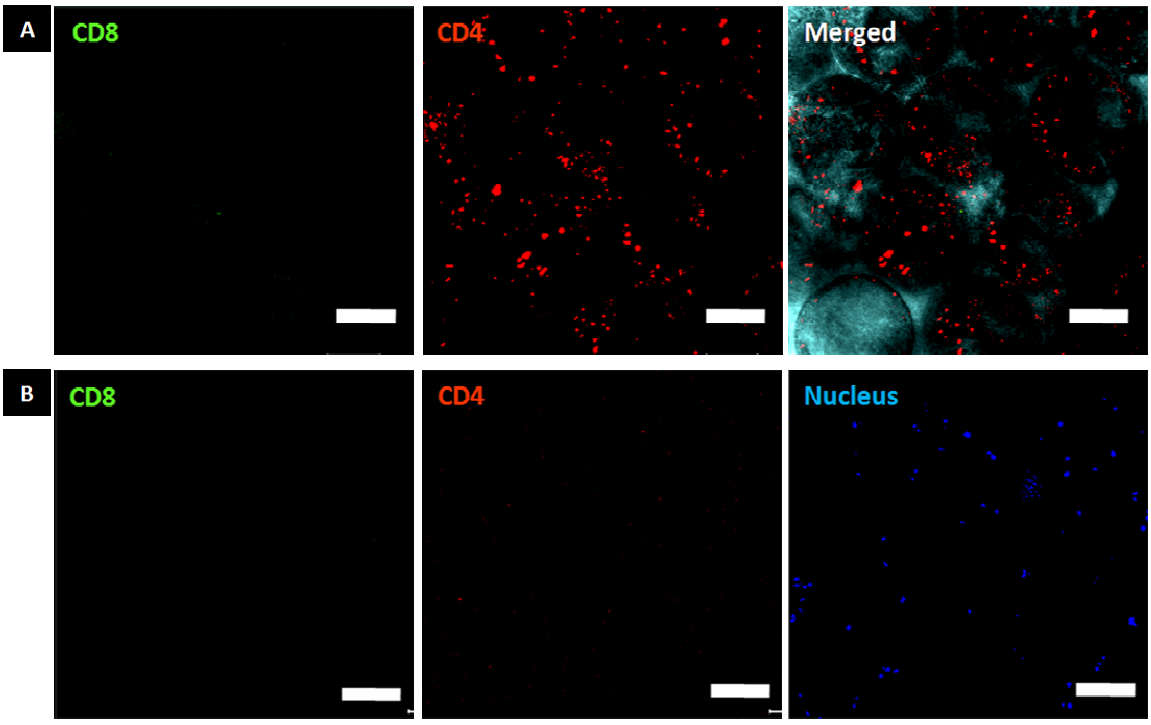

Figure 6.13 CD4 T-cell differentiation after 28 days of culture. **(A)** DL-1 notch ligands coated ICC scaffolds induced CD8-/CD4+ T-cell development. **(B)** Neither CD4 nor CD8 molecule was detected on the ICC scaffold in the absence of DL-1 notch ligand coating. (Scale bar is 80μm)

Potentially the LBL coating system can also be applied to recapitulate the other function of stromal cells, releasing soluble growth factors. Since multiple functional components can be sequentially incorporated into a growing film, a compartmentalized LBL film consisted of soluble signaling molecule embedded bottom layers and ligands presenting top layers can be prepared on the surface of 3D scaffolds. Diffusion of soluble factors can be regulated by hydrolytically degradable polymer components.[89] In addition, recently discovered an exponential LBL system can be used for loading and unloading soluble signaling molecules.[330, 331] As a result, such multicompoent and functional LBL film on 3D scaffolds can deliver both insoluble and soluble signaling molecules to the cells, which in turn significantly improve the creation of artificial 3D HSC niches in a simple and effective way.

6.4. Summary

ICC hydrogel scaffolds combined with a LBL surface modification technique enabled to create functional HSC niches for bone marrow and thymic tissues. The described bone marrow construct replicates two of the key reproductive functions of normal bone marrow. Notch ligand immobilized ICC scaffolds also successfully promotes T-cell development of HSCs in the absence of stromal cells. These data demonstrate that proper organization of cells provided by the ICC scaffold has tremendous importance in *ex vivo* replication of HSC niches. As a valuable tool, the LBL-ICC scaffold system can significantly contribute to the realization of artificial bone marrow and thymus construction one step closer. It can potentially allow not only *ex vivo* production of clinically important stem/immune cells but also preclinical immunotoxicity testing which are not available now.

CHAPTER VII

SUGGESTED FUTURE DIRECTIONS & CONCLUSION

7.1. Suggested future directions

7.1.1. Direction for ICC scaffold fabrication

In this dissertation work, all PS and glass microparticles were purchased from commercial vendors. Although highly ordered uniform size spherical pore arrays is the distinguished feature of ICC scaffolds, the high cost of uniform size beads has been the major bottleneck to realize the mass production of the scaffolds. This issue should be overcome. The solution can be found in emulsion polymerization that has been extensively utilized for the preparation of mono-dispersed polymeric particles utilizing simple micro-fluidic devices.

Recently glass capillary based micro-fluidic device design was introduced which made possible simple preparation of uniform size polymeric microparticles[332]. The most representative system is PCL and PLGA microparticle synthesis utilizing two syringe pumps[333]. As shown in Figure 7.1, the device set-up is very simple and preliminary result was quite promising. However, significant amount of work should be followed to accomplish highly ordered CC and ICC preparation utilizing homemade microparticles.

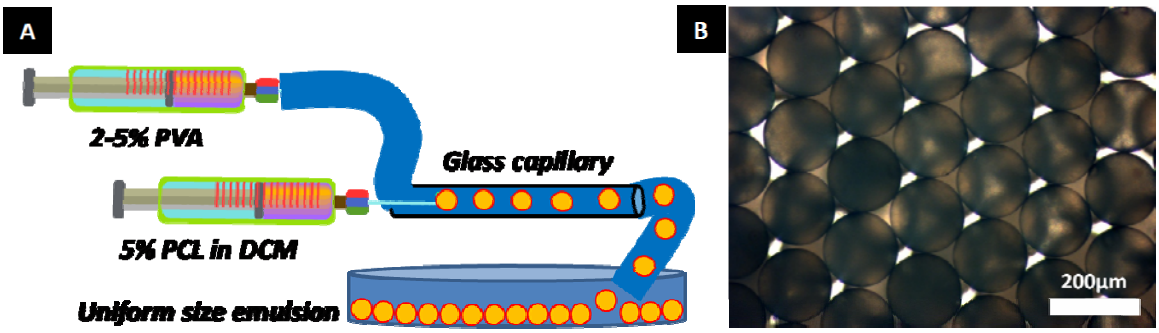

Figure 7.1 PCL microparticle syntheses via emulsion polymerization (A) Schematic of PCL microparticle synthesis via micro-emulsion technique, (B) Solidified PCL microparticles.

7.1.2. Direction for spheroid engineering

The engineering liver tissue spheroid culture system can be applied to other types of cells including primary cells, stem cells and tumor cells. For example, aggregates of embryonic and neural stem cells can form embryonic bodies and neurospheres, respectively[334]. It has been known that the stem cell spheroid size is closely related to the degree of differentiation. ICC scaffolds would be a valuable tool for the systematic investigation of such relationship.

Another interesting direction will be employing biodegradable microparticles including signaling molecules during the stem cell spheroid formation. Microparticles having a similar dimension to cells could be incorporated as a part of cell aggregate and then slowly release signaling proteins corresponding to their degradation within the spheroid. As a result, it can generate more homogenous signaling molecules profile across the spheroid which in turn improves unidirectional stem cell differentiation than normal culture condition, typically having a diffusion gradient of signaling molecules. In addition, these microparticles can be used for sensing local chemical and physical environments in spheroids.

Besides stem cells, tumor spheroids culture model will be another important research topic. Although HepG2 spheroids exhibited liver tissue-like functions to some extent, overall their morphology and functions are closer to tumors because they were originally derived from tumors. Indeed the reduced metabolic activity of HepG2 spheroids in Chapter 3 can be regarded as dormant stage tumor nodules. They can be used as a tumor dormant model for better understanding tumor cells metastasis and repopulation. In addition, the spheroid size controllable feature can be applied to develop a tumor hypoxia model as increasing their size larger than the diffusion limit of oxygen (300 μm>). It can also serve as an early stage tumor nodule model for diagnostic and treatment purposes. Currently small size tumors are difficult to detect while hypoxic environment reduce the effectiveness radiation therapy. Well controlled *in vitro* tumor spheroid model can significantly contribute to overcome these issues.

Lastly tumor spheroids and immune cells co-culture model also will be an interesting research area. A tumor spheroid entrapped in an ICC pore takes up only 50 % of pore volume, whereas the remaining 50 % of pore volume can be used as a pathway for circulating immune cells (i.e. T-/B-lymphocytes, dendritic cells and macrophages) within the scaffold. As a result, immune cells can effectively scavenge and contact with tumor spheroids. Such a unique immunological microenvironment can be used for answering various questions such as suppressed immune response by cancer cells, anticancer mechanism by activated immune cells, etc. Particularly these data will significantly contribute to the cancer vaccine research. (Figure 7.2)

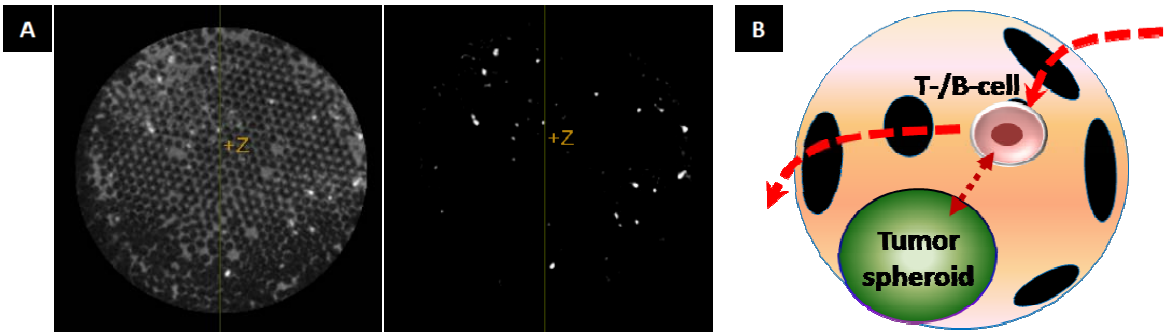

Figure 7.2 *In vitro* tumor spheroid culture models (A) (Left) Tumor spheroids µ-CT imaging after OsO4 (osmium) staining. Densely packed tumor cell aggregates appear brighter than background hydrogel matrix. (Right) An enhanced contrast image clearly shows spheroids. **(B)** Schematic of tumor spheroids and immune cells co-culture model.

7.1.3. Direction for immune system engineering

Although primary lymphoid tissue models were successfully accomplished, significant research efforts should be followed to realize their practical application in the drug testing application. The two most critical issues are (i) how to realize similar dynamic fluids in a micro-well plate to a rotary cell culture system and (ii) how to effectively extract target cells from ICC scaffolds. Potential solutions can be found in engineering functional ICC scaffolds and culture devices. For example, ICC scaffolds including magnetic components such as magnetic NPs, magnetic micro-beads or magnetically susceptible stainless steels can deliver motility of the scaffolds under the magnetic fields. It can generate a continuous dynamic media flow within the ICC scaffolds. For this purpose, specific design of magnetic device should be made simultaneously to apply periodic and homogeneous magnetic fields in each well.

The development of effective cell harvesting system is equally important because here the final products are individual HSCs or immune cells rather than a bulk functional tissue. ICC geometry is exceptionally beneficial for HSC culture: however, their intricate

pore structure limits efficient harvesting target cells from the scaffold. For this purpose, the development of smart hydrogels that can rapidly dissolve or swell under physiologically tolerable chemical or physical environmental changes would be promising approach.

The dissertation primarily focuses on primary lymphoid tissues, i.e. bone marrow and thymus, but the same system can be also applied to create secondary and tertiary lymphoid tissues. Secondary lymphoid tissues including spleen, lymph nodes and mucosal lymphoid tissues are essential for initiating adaptive immune responses[335-337]. Tertiary lymphoid tissues located at sites of chronic inflammation have considerable morphological and functional similarity to secondary lymphoid tissues. Both tissues provide proper 3D microenvironments for the appropriate interactions between antigens, antigen presenting cells and lymphocytes which is the key process immune cell activation. The unique feature of ICC geometry for inducing intimate cell-cell contacts between floating and adherent cells can significantly contribute to the secondary and tertiary lymphoid tissue engineering. (Figure 7.3)

Lastly all research efforts have been focused on creating *in vitro* function lymphoid tissues. However, faithfully established tissue models can be used for investigating the mechanisms of how tissues lose their function. Such *ex vivo* human lymphoid tissue models would greatly accelerate understanding and curing diseases related to the human immune system.

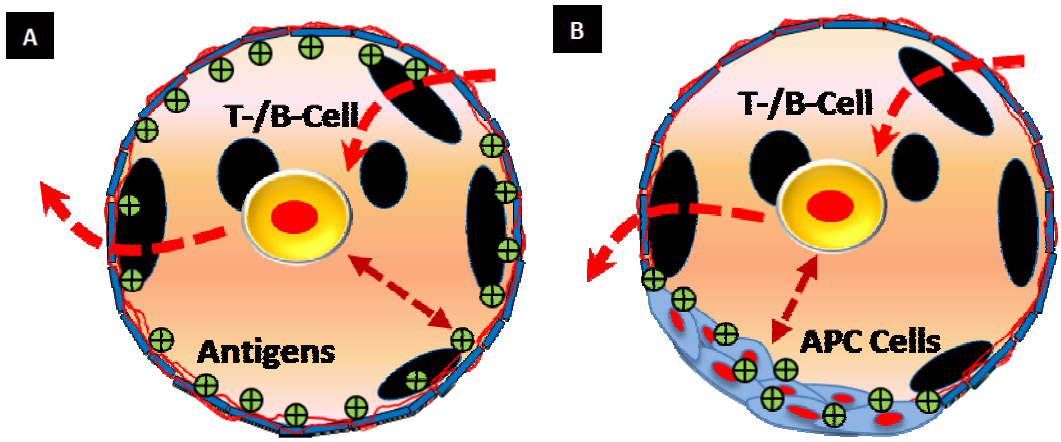

Figure 7.3 Schematic of secondary and tertiary lymphoid tissue engineering (A) LBL immobilized antigens on ICC pore surface to activate immune cells **(B)** Co-culture of antigen presenting cells and naïve T-/B-lymphocytes

7.2. Concluding remarks

My doctoral work mainly focuses on two directions: (i) developing robust techniques for the ICC scaffold fabrication and (ii) demonstrating exclusively distinguished biological significance of the ICC scaffold. The most important achievement in the first part was the improvement of the method for obtaining highly ordered CCs in microscale that enabled ICC scaffolds research more conveniently and effectively. In the second part, I evaluate that my most significant devotion was developing a new opportunity of ICC scaffolds as a distinctive platform for spheroid culture. This work was successfully expanded to the standardized liver tissue spheroid culture model and further utilized as an *in vitro* toxicity testing platform.

I would like to make four important aspects of this dissertation. First, the thesis is looking for a new opportunity of tissue engineering escaping from the classical tissue engineering theme. Tissue engineering for *in vitro* applications is a quite new idea and it is becoming more concrete and feasible accompanied with recent advances in stem cell

research, biotechnologies and scaffold fabrication techniques. My work demonstrated promising potential of this research direction and discussed many critical considerations particularly for the scaffold design.

Second, the primary lymphoid tissue engineering is relatively new. Typical tissue engineering models include skin, bone, cartilage, liver, heart, muscle, blood vessels, and so on. Here we aimed to recreate more complex and functional 3D HSC niches for bone marrow and thymus. Although significant research efforts should be followed, our results clearly demonstrated the pivotal role of scaffold-engineering techniques in functional reconstitution of stem cell niches. I expect these work would bring broad and significant attention from the stem cell research society.

Third, it adequately balances the modeling and experimental works. Highly regulated ICC structures made possible computer modeling approach, which delivered guidelines for the scaffold design and proved biological significance of the scaffold combined with experimental data.

Lastly, I would like to stress that this dissertation research not only remains in publications but also significantly contributes to commercialization of the ICC scaffold that I believe one of major missions of biomedical engineers. My doctoral work provided backbone techniques for launching a company specialized in ICC scaffold manufacturing i.e. 3D Biomatrix (www.3d-biomatrix.com). I hope the ICC scaffold can significantly contribute to the improvement of human health.

APPENDIX

A. Publications related to each chapter

CHAPTER 1. INTRODUCTION

Jungwoo Lee, Meghan J. Cuddihy, Nicholas A. Kotov "3D Cell Culture Matrices: State of The Art" *Tissue Engineering Part B: Review* (2008), 14(1), 61-86 (Most read article until now)

CHAPTER 2. INVERTED COLLOIDAL CRYSTAL HYDROGEL SCAFFOLDS

Jungwoo Lee, Sachin Shanbhag, Nicholas Kotov "Inverted Colloidal Crystals (ICC) Scaffolds as Three Dimensional Microenvironments for cellular co-cultures" *Journal of Material Chemistry* (2006), 16(35), 3558-3564 (Front Cover Article)

CHAPTER 3. ENGINEERING HUMAN LIVER TISSUE SPHEROIDS

Jungwoo Lee, Meghan J. Cuddihy, George Cater, Nicholas A. Kotov "Engineering liver tissue spheroids using inverted colloidal crystal (ICC) scaffolds" *Biomaterials, (2009) ASAP*

CHAPTER 4. IN VITRO TOXICITY TESTING OF NANOPARTICLES

Jungwoo Lee, Daniel G. Lilly, Christoper R. Doty, Paul Podsiadlo, Nicholas A. Kotov "In vitro toxicity testing of nanoparticles in three dimensional cell culture" *Small* (2009), 5(10) 1213-1221 (Research Highlights in Nature Nanotechnology)

CHAPTER 5. BIOACTIVE ICC SCAFFOLDS FOR CELLULAR CO-CULTURES

Jungwoo Lee, Sachin Shanbhag, Nicholas Kotov "Inverted Colloidal Crystals (ICC) Scaffolds as Three Dimensional Microenvironments for cellular co-cultures" *Journal of Material Chemistry* (2006), 16(35), 3558-3564 (Front Cover Article)

Sachin Shanbhag, **Jungwoo Lee**, Nicholas Kotov "Diffusion in Three Dimensionally Ordered Scaffolds with Inverted Colloidal Crystal Geometry" *Biomaterials* (2005), 26(27), 5581-5585

CHAPTER 6. ENGINEERIN PRIMARY LYMPHOID TISSUES

Jungwoo Lee, Nicholas A. Kotov "Notch ligand presenting acellular 3D microenvironments for ex vivo human hematopoietic stem cell culture made by layer-by-layer assembly" *Small* (2009), 5(9), 1008-1013 (Front Cover Article)

Joan E. Nichols, Joaquin Cortiella, **Jungwoo Lee**, Jean A. Niles, Meghan Cuddihy, Shaopeng Wang, Sonia Bynam, Andrea Cantu, Ron Mlcak, Esther Valdivia, Ryan Yancy, Jozeph Bielitzki, Matthew L. McClure, Nicholas A. Kotov "*In vitro* analog of human bone marrow from 3D scaffolds with biomimetic inverted colloidal crystal geometry" *Biomaterials (2008)* 30, 1071-1079 (Highlighted in U of M News)

REFERENCES

1. DiMasi AJ, Ronald HW, Grabowski GH. The price of innovation: New estimates of drug development costs. J Heal Econ 2003;22(2):151-186.
2. Uetz P, Giot L, Cagney G, Mansfield TA, Judson RS, Knight JR, et al. A comprehensive analysis of protein-protein interactions in Saccharomyces cerevisiae. Nature 2000;403(6770):623-627.
3. Starkuviene V, Pepperkok R. The potential of high-content high-throughput microscopy in drug discovery. British J Pharmacol 2007;152(1):62-71.
4. Butcher EC, Berg EL, Kunkel EJ. Systems biology in drug discovery. Nat Biotech 2004;22(10):1253-1259.
5. Berndt RE, Gottschalk HBA, Strobeck WM. Opportunities for improving the drug development process: Results from a survey of industry and the FDA: NBER; 2005.
6. Ashburn TT, Thor KB. Drug repositioning: identifying and developing new uses for existing drugs. Nat Rev Drug Discov 2004;3(8):673-683.
7. Berndt ER, Gottschalk AHB, Philipson TJ, Strobeck MW. Industry funding of the FDA: effects of PDUFA on approval times and withdrawal rates. Nat Rev Drug Discov 2005;4(7):545-554.
8. Wehling M. Assessing the translatability of drug projects: what needs to be scored to predict success? Nat Rev Drug Discov 2009
9. Lodish H, Berk A, Zipursky L, Matsudaira P, Baltimore D, Darnell J. Molecular Cell Biology: Chapter22 Integrating cells into tissue. 4th ed: W.H. Freeman and Company, 2002.
10. Gartner PL, Hiatt LJ. Color text book of histology. 2nd ed: Saunder, 2001.
11. Fuchs E, Tumbar T, Guasch G. Socializing with the neighbors: Stem cells and their niche. Cell 2004;116(6):769-778.
12. Abbott A. Cell culture: Biology's new dimension. Nature 2003;424(6951):870-872.
13. Cukierman E, Pankov R, Stevens DR, Yamada KM. Taking cell-matrix adhesions to the third dimension. Science 2001;294(5547):1708-1712.
14. Zhang S. Beyond the petri dish. Nat Biotech 2004;22(2):151-152.
15. McNeish J. Embryonic stem cells in drug discovery. Nat Rev Drug Discov 2004;3(1):70-80.
16. Engler AJ, Sen S, Sweeney HL, Discher DE. Matrix elasticity directs stem cell lineage specification. Cell 2006;126(4):677-689.
17. Pham QP, Sharma U, Mikos AG. Electrospinning of polymeric nanofibers for tissue engineering applications: A review. Tissue Eng 2006;12(5):1197-1211.
18. Mikos AG, Thorsen AJ, Czerwonka LA, Bao Y, Langer R, Winslow DN, et al. Preparation and characterization of poly(-lactic acid) foams. Polymer 1994;35(5):1068-1077.
19. Hollister SJ. Porous scaffold design for tissue engineering. Nat Mater 2006;5(7):590-590.
20. Shin H, Jo S, Mikos AG. Biomimetic materials for tissue engineering. Biomaterials 2003;24(24):4353-4364.
21. Stupp Sl, Donners JM, Li LS, Mata A. Expanding frontiers in biomaterials. MRS Bulletin 2005;30:864-873.
22. Martina MH, Dietmar W Biodegradable polymers applied in tissue engineering research: a review. Polymer Int 2007;56(2):145-157.
23. Hench LL, Polak JM. Third-generation biomedical materials. Science 2002;295(5557):1014-1017.

24. Langer R, Tirrell DA. Designing materials for biology and medicine. Nature 2004;428(6982):487-492.
25. Salvay DM, Shea LD. Inductive tissue engineering with protein and DNA-releasing scaffolds. Molecular BioSystems 2006;2(1):36-48.
26. Janeway CA, Travers P, Walport M, Shlomchik M. Immuno biology. 6th ed. New York: Garland Science Publishing, 2003.
27. Simmons CA, Alsberg E, Hsiong S, Kim WJ, Mooney DJ. Dual growth factor delivery and controlled scaffold degradation enhance in vivo bone formation by transplanted bone marrow stromal cells. Bone 2004;35(2):562-569.
28. Elkayam T, Amitay-Shaprut S, Dvir-Ginzberg M, Harel T, Cohen S. Enhancing the drug metabolism activities of C3A-a human hepatocyte cell line-by tissue engineering within alginate scaffolds. Tissue Eng 2006;12(5):1357-1368.
29. Bissell MJ, Rizki A, Mian IS. Tissue architecture: The ultimate regulator of breast epithelial function. Curr Opin Cell Biol 2003;15(6):753-762.
30. Lukashev ME, Werb Z. ECM signaling: orchestrating cell behavior and misbehaviour. Trends Cell Biol 1998;8(11):437-441.
31. Even-Ram S, Yamada KM. Cell migration in 3D matrix. Curr Opin Cell Biol 2005;17(5):524-532.
32. Muschler GF, Nakamoto C, Griffith LG. Engineering principles of clinical cell-based tissue engineering. J Bone Joint Surg Am 2004;86(7):1541-1558.
33. Hollister SJ, Levy RA, Chu T-M, Halloran JW, Feinberg SE. An image-based approach for designing and manufacturing craniofacial scaffolds. Int J Oral Maxillofacial Surg 2000;29(1):67-71.
34. Atala A, Bauer SB, Soker S, Yoo JJ, Retik AB. Tissue-engineered autologous bladders for patients needing cystoplasty. The Lancet 2006;367(9518):1241-1246.
35. Warnke PH, Springer ING, Wiltfang J, Acil Y, Eufinger H, Wehmoller M, et al. Growth and transplantation of a custom vascularized bone graft in a man. 2004;364(9436):766.
36. Cesarano J, Dellinger JG, Saavedra MP, Gill DD, Jamison RD, Grosser BA, et al. Customization of load-bearing hydroxyapatite lattice scaffolds. Int J Appl Ceramic Technol 2005;2:212-220.
37. Palsson B, Hubbell JA, Plonsey R, Bronzino JD. Tissue engineering: Chapter11 Engineering biomaterials for tissue engineering (The 10-100 micron size scale). 1st ed: CRC Press, 2003.
38. Gomez N, Lu Y, Chen S, Schmidt CE. Immobilized nerve growth factor and microtopography have distinct effects on polarization versus axon elongation in hippocampal cells in culture. Biomaterials 2007;28(2):271-284.
39. Zhu X, Mills KL, Peters PR, Bahng JH, Liu EH, Shim J, et al. Fabrication of reconfigurable protein matrices by cracking. Nat Mater 2005;4(5):403-406.
40. Williams JM, Adewunmi A, Schek RM, Flanagan CL, Krebsbach PH, Feinberg SE, et al. Bone tissue engineering using polycaprolactone scaffolds fabricated via selective laser sintering. Biomaterials 2005;26(23):4817-4827.
41. Stevens MM, George JH. Exploring and engineering the cell surface interface. Science 2005;310(5751):1135-1138.
42. Hartgerink JD, Beniash E, Stupp SI. Self-assembly and mineralization of peptide-amphiphile nanofibers. Science 2001;294(5547):1684-1688.
43. Vauthey S, Santoso S, Gong H, Watson N, Zhang S. Molecular self-assembly of surfactant-like peptides to form nanotubes and nanovesicles. Proc Natl Acad Sci USA 2002;99(8):5355-5360.
44. Sachlos E, Gotora D, Czernuszka JT. Collagen scaffolds reinforced with biomimetic composite nano-sized carbonate-substituted hydroxyapatite crystals and shaped by rapid prototyping to contain internal microchannels. Tissue Eng 2006;12(9):2479-2487.

45. Wei G, Ma PX. Structure and properties of nano-hydroxyapatite/polymer composite scaffolds for bone tissue engineering. Biomaterials 2004;25(19):4749-4757.
46. Li W-J, Tuli R, Huang X, Laquerriere P, Tuan RS. Multilineage differentiation of human mesenchymal stem cells in a three-dimensional nanofibrous scaffold. Biomaterials 2005;26(25):5158-5166.
47. Kay S, Thapa A, Haberstroh KM, Webster TJ. Nanostructured polymer/nanophase ceramic composites enhance osteoblast and chondrocyte adhesion. Tissue Eng 2002;8(5):753-761.
48. Barry J A, Howard D, Shakesheff KM, Howdle SM, Alexander MR. Using a core-sheath distribution of surface chemistry through 3D tissue engineering scaffolds to control cell ingress. Adv Mater 2006;18(11):1406-1410.
49. Li M, Mondrinos MJ, Chen X, Gandhi MR, Ko FK, Lelkes PI. Co-electrospun poly(lactide-*co*-glycolide), gelatin, and elastin blends for tissue engineering scaffolds. J Biomed Mater Res A 2006;79A(4):963-973.
50. Wei G, Ma PX. Macroporous and nanofibrous polymer scaffolds and polymer/bone-like apatite composite scaffolds generated by sugar spheres. J Biomed Mater Res A 2006;78A(2):306-315.
51. Park GE, Pattison MA, Park K, Webster TJ. Accelerated chondrocyte functions on NaOH-treated PLGA scaffolds. Biomaterials 2005;26(16):3075-3082.
52. Ratner BD, Hoffman AS, Schoen FJ, Lemons JE. Biomaterials Science: An Introduction to Materials in Medicine. 2nd ed: Elsevier Academic Press, 2004
53. Lee KY, Mooney DJ. Hydrogels for tissue engineering. Chem Rev 2001;101(7):1869-1880.
54. Ma PX, Elisseeff J. Scaffolding in tissue engineering: CRC Press, 2006.
55. Zhang S. Hydrogels: Wet or let die. Nat Mater 2004;3(1):7-8.
56. Drury JL, Mooney DJ. Hydrogels for tissue engineering: scaffold design variables and applications. Biomaterials 2003;24(24):4337-4351.
57. Lee J, Shanbhag S, Kotov NA. Inverted colloidal crystals as three-dimensional microenvironments for cellular co-cultures. J Mater Chem 2006;16(35):3558-3564.
58. Kim D, Park S, Lee JH, Jeong YY, Jon S. Antibiofouling polymer-coated gold nanoparticles as a contrast agent for in vivo X-ray computed tomography imaging. J Am Chem Soc 2007;129(24):7661-7665.
59. Hyafil F, Cornily J-C, Feig JE, Gordon R, Vucic E, Amirbekian V, et al. Noninvasive detection of macrophages using a nanoparticulate contrast agent for computed tomography. Nat Med 2007;13(5):636-641.
60. Hainfeld JF, Slatkin DN, Focella TM, Smilowitz HM. Gold nanoparticles: a new X-ray contrast agent. British J Radiol 2006;79:248-253.
61. Rabin O, Manuel Perez J, Grimm J, Wojtkiewicz G, Weissleder R. An X-ray computed tomography imaging agent based on long-circulating bismuth sulphide nanoparticles. Nat Mater 2006;5(2):118-122.
62. Li S. Hydrolytic degradation characteristics of aliphatic polyesters derived from lactic and glycolic acids. J Biomed Mater Res 1999;48(3):342.
63. Yannas IV, Burke JF, Huang C, Gordon PL. Correlation of in vivo collagen degradation rate with in vitro measurements. J Biomed Mater Res1975;9(6):623.
64. Dong C-M, Guo Y-Z, Qiu K-Y, Gu Z-W, Feng X-D. In vitro degradation and controlled release behavior of d,l-PLGA50 and PCL-b-d,l-PLGA50 copolymer microspheres. J Control Rel 2005;107(1):53-64.
65. van Amerongen MJ, Harmsen MC, Petersen AH, Kors G, van Luyn MJA. The enzymatic degradation of scaffolds and their replacement by vascularized extracellular matrix in the murine myocardium. Biomaterials 2006;27(10):2247-2257.

66. Adachi T, Osako Y, Tanaka M, Hojo M, Hollister SJ. Framework for optimal design of porous scaffold microstructure by computational simulation of bone regeneration. Biomaterials 2006;27(21):3964-3972.
67. Discher DE, Janmey P, Wang Y-l. Tissue cells feel and respond to the stiffness of their substrate. Science 2005;310(5751):1139-1143.
68. Kong HJ, Polte TR, Alsberg E, Mooney DJ. FRET measurements of cell-traction forces and nano-scale clustering of adhesion ligands varied by substrate stiffness. Proc Natl Acad Sci USA 2005;102(12):4300-4305.
69. Feng Q, Chai C, Jiang X-S, Leong WK, Mao H-Q. Expansion of engrafting human hematopoietic stem/progenitor cells in three-dimensional scaffolds with surface-immobilized fibronectin. J Biomed Mater Res A 2006;78A(4):781-791.
70. Chastain SR, Kundu AK, Dhar S, Calvert JW, Putnam AJ. Adhesion of mesenchymal stem cells to polymer scaffolds occurs via distinct ECM ligands and controls their osteogenic differentiation. J Biomed Mater Res A 2006;78A(1):73-85.
71. Patel PN, Gobin AS, West JL, Patrick CW. Poly(ethylene glycol) hydrogel system supports preadipocyte viability, adhesion, and proliferation. Tissue Eng 2005;11(9-10):1498-1505.
72. Brinkman WT, Nagapudi K, Thomas BS, Chaikof EL. Photo-cross-linking of type I collagen gels in the presence of smooth muscle cells: mechanical properties, cell viability, and function. Biomacromol 2003;4(4):890-895.
73. Prestwich GD, Marecak DM, Marecek JF, Vercruysse KP, Ziebell MR. Controlled chemical modification of hyaluronic acid: synthesis, applications, and biodegradation of hydrazide derivatives. J Control Rel 1998;53(1-3):93-103.
74. Saltzman WM, Olbricht WL. Building drug delivery into tissue engineering. Nat Rev Drug Dis 2002;1(3):177-186.
75. Richardson TP, Peters MC, Ennett AB, Mooney DJ. Polymeric system for dual growth factor delivery. Nat Biotech 2001;19(11):1029-1034.
76. Edwards PC, Ruggiero S, Fantasia J, Burakoff R, Moorji SM, Paric E, et al. Sonic hedgehog gene-enhanced tissue engineering for bone regeneration. Gene Ther 2004;12(1):75-86.
77. Shi X, Sitharaman B, Pham QP, Liang F, Wu K, Edward Billups W, et al. Fabrication of porous ultra-short single-walled carbon nanotube nanocomposite scaffolds for bone tissue engineering. Biomaterials 2007;28(28):4078-4090.
78. Singh R, Pantarotto D, Lacerda L, Pastorin G, Klumpp C, Prato M, et al. Tissue biodistribution and blood clearance rates of intravenously administered carbon nanotube radiotracers. Proc Natl Acad Sci USA 2006;103(9):3357-3362.
79. Lovat V, Pantarotto D, Lagostena L, Cacciari B, Grandolfo M, Righi M, et al. Carbon nanotube substrates boost neuronal electrical signaling. Nano Lett 2005;5(6):1107-1110.
80. Gheith MK, Pappas TC, Liopo AV, Sinani VA, Shim BS, Motamedi M, et al. Stimulation of neural cells by lateral currents in conductive layer-by-layer films of single-walled carbon nanotubes. Adv Mater 2006;18(22):2975-2979.
81. Jan E, Kotov NA. Successful differentiation of mouse neural stem cells on layer-by-layer assembled single-walled carbon nanotube composite. Nano Lett 2007;7(5):1123-1128.
82. Wilson CJ, Clegg RE, Leavesley DI, Pearcy MJ. Mediation of biomaterial-cell interactions by adsorbed proteins: A review. Tissue Eng 2005;11(1-2):1-18.
83. Allen LT, Tosetto M, Miller IS, O'Connor DP, Penney SC, Lynch I, et al. Surface-induced changes in protein adsorption and implications for cellular phenotypic responses to surface interaction. Biomaterials 2006;27(16):3096-3108.
84. Chen YM, Shiraishi N, Satokawa H, Kakugo A, Narita T, Gong JP, et al. Cultivation of endothelial cells on adhesive protein-free synthetic polymer gels. Biomaterials 2005;26(22):4588-4596.

85. Schneider GB, English A, Abraham M, Zaharias R, Stanford C, Keller J. The effect of hydrogel charge density on cell attachment. Biomaterials 2004;25(15):3023-3028.
86. Keselowsky BG, Collard DM, Garcia AJ. Integrin binding specificity regulates biomaterial surface chemistry effects on cell differentiation. Proc Natl Acad Sci USA 2005;102(17):5953-5957.
87. Tang Z, Wang Y, Podsiadlo P, Kotov NA. Biomedical applications of layer-by-layer assembly: from miomimetics to tissue engineering. Adv Mater 2006;18(24):3203-3224.
88. Decher G. Fuzzy nanoassemblies: Toward layered polymeric multicomposites. Science 1997;277(5330):1232-1237.
89. Wood KC, Chuang HF, Batten RD, Lynn DM, Hammond PT. Controlling interlayer diffusion to achieve sustained, multiagent delivery from layer-by-layer thin films. Proc Natl Acad Sci USA 2006;103(27):10207-10212.
90. Dierich A, Le Guen E, Messaddeq N, Stoltz JF, Netter P, Schaaf P, et al. Bone formation mediated by synergy-acting growth factors embedded in a polyelectrolyte multilayer film. Adv Mater 2007;19(5):693-697.
91. Chen H-Y, Elkasabi Y, Lahann J. Surface modification of confined microgeometries via vapor-deposited polymer coatings. J Am Chem Soc 2006;128(1):374-380.
92. Datta N, P. Pham Q, Sharma U, Sikavitsas VI, Jansen JA, Mikos AG. In vitro generated extracellular matrix and fluid shear stress synergistically enhance 3D osteoblastic differentiation. Pro Natl Acad Sci USA 2006;103(8):2488-2493.
93. Weaver VM, Petersen OW, Wang F, Larabell CA, Briand P, Damsky C, et al. Reversion of the malignant phenotype of human breast cells in three-dimensional culture and *in vivo* by integrin blocking antibodies. J Cell Biol 1997;137(1):231-245.
94. Lutolf MP, Weber FE, Schmoekel HG, Schense JC, Kohler T, Muller R, et al. Repair of bone defects using synthetic mimetics of collagenous extracellular matrices. Nat Biotech 2003;21(5):513-518.
95. Moutos FT, Freed LE, Guilak F. A biomimetic three-dimensional woven composite scaffold for functional tissue engineering of cartilage. Nat Mater 2007;6(2):162-167.
96. Hohlfeld J, de Buys Roessingh A, Hirt-Burri N, Chaubert P, Gerber S, Scaletta C, et al. Tissue engineered fetal skin constructs for paediatric burns. The Lancet 2005;366(9488):840-842.
97. Seo S-J, Kim I-Y, Choi Y-J, Akaike T, Cho C-S. Enhanced liver functions of hepatocytes cocultured with NIH 3T3 in the alginate/galactosylated chitosan scaffold. Biomaterials 2006;27(8):1487-1495.
98. Niklason LE, Gao J, Abbott WM, Hirschi KK, Houser S, Marini R, et al. Functional arteries grown *in vitro*. Science 1999;284(5413):489-493.
99. Levenberg S, Rouwkema J, Macdonald M, Garfein ES, Kohane DS, Darland DC, et al. Engineering vascularized skeletal muscle tissue. Nat Biotech 2005;23(7):879-884.
100. Wang G-J, Hsu Y-F, Hsu S-H, Horng R. JSR photolithography based microvessel scaffold fabrication and cell seeding. Biomed Microdev 2006;8:17-23.
101. Khademhosseini A, Ferreira L, Blumling Iii J, Yeh J, Karp JM, Fukuda J, et al. Co-culture of human embryonic stem cells with murine embryonic fibroblasts on microwell-patterned substrates. Biomaterials 2006;27(36):5968-5977.
102. Li L, Fourkas JT. Multiphoton polymerization. Mater Today 2007;10(6):30-37.
103. Uludag H, De Vos P, Tresco PA. Technology of mammalian cell encapsulation. Adv Drug Del Rev 2000;42(1-2):29-64.
104. Bunger CM, Tiefenbach B, Jahnke A, Gerlach C, Freier T, Schmitz KP, et al. Deletion of the tissue response against alginate-pll capsules by temporary release of co-encapsulated steroids. Biomaterials 2005;26(15):2353-2360.
105. Zhang S. Fabrication of novel biomaterials through molecular self-assembly. Nat Biotech 2003;21(10):1171-1178.

106. Kleinman HK, Martin GR. Matrigel: Basement membrane matrix with biological activity. Semin Cancer Biol 2005;15(5):378-386.
107. Blomback B, Bark N. Fibrinopeptides and fibrin gel structure. Biophys Chem 2004;112(2-3):147-151.
108. Augst AD, Kong HJ, Mooney DJ. Alginate hydrogels as biomaterials. Macromol Biosci 2006;6(8):623-633.
109. Kisiday J, Jin M, Kurz B, Hung H, Semino C, Zhang S, et al. Self-assembling peptide hydrogel fosters chondrocyte extracellular matrix production and cell division: Implications for cartilage tissue repair. Proc Natl Acad Sci USA 2002;99(15):9996-10001.
110. Elisseeff J, Anseth K, Sims D, McIntosh W, Randolph M, Langer R. Transdermal photopolymerization for minimally invasive implantation. Pro Natl Acad Sci USA 1999;96(6):3104-3107.
111. Ellis-Behnke RG, Liang Y-X, You S-W, Tay DKC, Zhang S, So K-F, et al. Nano neuro knitting: Peptide nanofiber scaffold for brain repair and axon regeneration with functional return of vision. Pro Natl Acad Sci USA 2006;103(13):5054-5059.
112. Silva GA, Czeisler C, Niece KL, Beniash E, Harrington DA, Kessler JA, et al. Selective differentiation of neural progenitor cells by high-epitope density nanofibers. Science 2004;303(5662):1352-1355.
113. Li Y, Tseng YD, Kwon SY, d'Espaux L, Bunch JS, McEuen PL, et al. Controlled assembly of dendrimer-like DNA. Nat Mater 2004;3(1):38-42.
114. Um SH, Lee JB, Park N, Kwon SY, Umbach CC, Luo D. Enzyme-catalysed assembly of DNA hydrogel. Nat Mater 2006;5(10):797-801.
115. Hohnadel DC, Cooper C. The effect of structural alterations on the reactivity of the nucleotide substrate of rabbit muscle pyruvate kinase. FEBS Lett 1973;30(1):18-20.
116. Lutolf MP, Lauer-Fields JL, Schmoekel HG, Metters AT, Weber FE, Fields GB, et al. Synthetic matrix metalloproteinase-sensitive hydrogels for the conduction of tissue regeneration: Engineering cell-invasion characteristics. Proc Natl Acad Sci USA 2003;100(9):5413-5418.
117. Lutolf MP, Raeber GP, Zisch AH, Tirelli N, Hubbell JA. Cell-responsive synthetic hydrogels. Adv Mater 2003;15(11):888-892.
118. Guler MO, Soukasene S, Hulvat JF, Stupp SI. Presentation and recognition of biotin on nanofibers formed by branched peptide amphiphiles. Nano Lett 2005;5(2):249-252.
119. Albrecht DR, Underhill GH, Wassermann TB, Sah RL, Bhatia SN. Probing the role of multicellular organization in three-dimensional microenvironments. Nat Meth 2006;3(5):369-375.
120. Kuo CK, Ma PX. Ionically crosslinked alginate hydrogels as scaffolds for tissue engineering: Part 1. Structure, gelation rate and mechanical properties. Biomaterials 2001;22(6):511-521.
121. Wang D-a, Williams CG, Li Q, Sharma B, Elisseeff JH. Synthesis and characterization of a novel degradable phosphate-containing hydrogel. Biomaterials 2003;24(22):3969-3980.
122. Sharma B, Williams CG, Kim TK, Sun D, Malik A, Khan M, et al. Designing zonal organization into tissue-engineered cartilage. Tissue Engineering 2007;13(2):405-414.
123. Stupp SI. Biomaterials for regenerative medicine. MRS Bulletin 2005;30:546-553.
124. LaBean T. Hydrogels: DNA bulks up. Nat Mater 2006;5(10):767-768.
125. Almany L, Seliktar D. Biosynthetic hydrogel scaffolds made from fibrinogen and polyethylene glycol for 3D cell cultures. Biomaterials 2005;26(15):2467-2477.
126. Lanza PR, Langer R, Vacanti J. Principels of tissue enginnering 2nd ed: Academic Press, 2000.
127. Whang K, Thomas CH, Healy KE, Nuber G. A novel method to fabricate bioabsorbable scaffolds. Polymer 1995;36(4):837-842.

128. Mooney DJ, Baldwin DF, Suh NP, Vacanti JP, Langer R. Novel approach to fabricate porous sponges of poly(-lactic-co-glycolic acid) without the use of organic solvents. Biomaterials 1996;17(14):1417-1422.
129. Murphy WL, Dennis RG, Kileny JL, Mooney DJ. Salt fusion: An approach to improve pore interconnectivity within tissue engineering scaffolds. Tissue Eng 2002;8(1):43-52.
130. Ma PX, Choi J-W. Biodegradable polymer scaffolds with well-defined interconnected spherical pore network. Tissue Eng 2001;7(1):23-33.
131. Hou Q, Grijpma DW, Feijen J. Preparation of interconnected highly porous polymeric structures by a replication and freeze-drying process. J Biomed Mater Res B: Appl Biomater 2003;67B(2):732-740.
132. Harris LD, Kim B-S, Mooney DJ. Open pore biodegradable matrices formed with gas foaming. J Biomed Mater Res 1998;42(3):396-402.
133. Chew SY, Wen J, Yim EKF, Leong KW. Sustained release of proteins from electrospun biodegradable fibers. Biomacromol 2005;6(4):2017-2024.
134. Li D, Ouyang G, McCann JT, Xia Y. Collecting electrospun nanofibers with patterned electrodes. Nano Lett 2005;5(5):913-916.
135. Zhang P-C, Zhang Y, Ouyang H, Lim CT, Ramakrishna S, Huang Z-M. Electrospinning of gelatin fibers and gelatin/PCL composite fibrous scaffolds. J Biomed Mater Res 2005;72B(1):156-165.
136. Pham QP, Sharma U, Mikos AG. Electrospun poly(e-caprolactone) microfiber and multilayer nanofiber/microfiber scaffolds: Characterization of scaffolds and measurement of cellular Infiltration. Biomacromol 2006;7(10):2796-2805.
137. Lu L, Mikos AG. The importance of new processing techniques in tissue engineering. MRS Bulletin 1996;21.
138. Shea LD, Smiley E, Bonadio J, Mooney DJ. DNA delivery from polymer matrices for tissue engineering. Nat Biotech 1999;17(6):551-554.
139. Teng YD, Lavik EB, Qu X, Park KI, Ourednik J, Zurakowski D, et al. Functional recovery following traumatic spinal cord injury mediated by a unique polymer scaffold seeded with neural stem cells. Proc Natl Acad Sci USA 2002;99(5):3024-3029.
140. Ma XP, Zhang R. Synthetic nano-scale fibrous extracellular matrix. J Biomed Mater Res 1999;46(1):60-72.
141. Chen VJ, Ma PX. Nano-fibrous poly(lactic acid) scaffolds with interconnected spherical macropores. Biomaterials 2004;25(11):2065-2073.
142. Kim S-S, Sun Park M, Jeon O, Yong Choi C, Kim B-S. Poly(lactide-co-glycolide)/hydroxyapatite composite scaffolds for bone tissue engineering. Biomaterials 2006;27(8):1399-1409.
143. Luu YK, Kim K, Hsiao BS, Chu B, Hadjiargyrou M. Development of a nanostructured DNA delivery scaffold via electrospinning of PLGA and PLA-PEG block copolymers. J Control Rel 2003;89(2):341-353.
144. McCann JT, Chen JIL, Li D, Ye Z-G, Xia Y. Electrospinning of polycrystalline barium titanate nanofibers with controllable morphology and alignment. Chem Phys Lett 2006;424(1-3):162-166.
145. Lee SB, Kim YH, Chong MS, Hong SH, Lee YM. Study of gelatin-containing artificial skin V: fabrication of gelatin scaffolds using a salt-leaching method. Biomaterials 2005;26(14):1961-1968.
146. Bhattarai N, Li Z, Edmondson D, Zhang M. Alginate-based nanofibrous scaffolds: Structural, mechanical, and biological Properties. Adv Mater 2006;18(11):1463-1467.
147. Pattison MA, Wurster S, Webster TJ, Haberstroh KM. Three-dimensional, nano-structured PLGA scaffolds for bladder tissue replacement applications. Biomaterials 2005;26(15):2491-2500.

148. Hutmacher DW, Sittinger M, Risbud MV. Scaffold-based tissue engineering: rationale for computer-aided design and solid free-form fabrication systems. Trends Biotechnol 2004;22(7):354-362.
149. Levy RA, Chu TM, Halloran JW, Feinberg SE, Hollister S. CT-generated porous hydroxyapatite orbital floor prosthesis as a prototype bioimplant. AJNR Am J Neuroradiol 1997;18(8):1522-1525.
150. Partee B, Hollister SJ, Das S. Selective laser sintering of polycaprolactone bone tissue engineering. MRS; 2005. p. AA9.9.1-AA9.9.7.
151. Lin CY, Kikuchi N, Hollister SJ. A novel method for biomaterial scaffold internal architecture design to match bone elastic properties with desired porosity. J Biomech 2004;37(5):623-636.
152. Dellinger JG, Cesarano JI, Jamison RD. Robotic deposition of model hydroxyapatite scaffolds with multiple architectures and multiscale porosity for bone tissue engineering. J Biomed Mater Res A 2007;82A(2):383-394.
153. Sherwood JK, Riley SL, Palazzolo R, Brown SC, Monkhouse DC, Coates M, et al. A three-dimensional osteochondral composite scaffold for articular cartilage repair. Biomaterials 2002;23(24):4739-4751.
154. Seet KK, Mizeikis V, Juodkazis S, Misawa H. Three-dimensional horizontal circular spiral photonic crystals with stop gaps below 1 mu. Appl Phys Lett 2006;88(22):221101-221103.
155. Hahn MS, Miller JS, West JL. Three-dimensional biochemical and biomechanical patterning of hydrogels for guiding cell behavior. Adv Mater 2006;18(20):2679-2684.
156. Yeong W-Y, Chua C-K, Leong K-F, Chandrasekaran M. Rapid prototyping in tissue engineering: Challenges and potential. Trends Biotechnol 2004;22(12):643-652.
157. Leong KF, Cheah CM, Chua CK. Solid freeform fabrication of three-dimensional scaffolds for engineering replacement tissues and organs. Biomaterials 2003;24(13):2363-2378.
158. Russias J, Saiz E, Nalla R, Tomsia A. Microspheres as building blocks for hydroxyapatite/polylactide biodegradable composites. J Mater Sci 2006;41(16):5127-5133.
159. Mondrinos MJ, Dembzynski R, Lu L, Byrapogu VKC, Wootton DM, Lelkes PI, et al. Porogen-based solid freeform fabrication of polycaprolactone-calcium phosphate scaffolds for tissue engineering. Biomaterials 2006;27(25):4399-4408.
160. Wahl D, Sachlos E, Liu C, Czernuszka J. Controlling the processing of collagen-hydroxyapatite scaffolds for bone tissue engineering. J Mater Sci: Mater Med 2007;18(2):201-209.
161. Cao T, Ho K-H, Teoh S-H. Scaffold design and *in vitro* study of osteochondral coculture in a three-dimensional porous polycaprolactone scaffold fabricated by fused deposition modeling. Tissue Eng 2003;9(supplement 1):103-112.
162. Cooke MN, Fisher JP, Dean D, Rimnac C, Mikos AG. Use of stereolithography to manufacture critical-sized 3D biodegradable scaffolds for bone ingrowth. J Biomed Mater Res 2003;64B(2):65-69.
163. Rimell JT, Marquis PM. Selective laser sintering of ultra high molecular weight polyethylene for clinical applications. J Biomed Mater Res 2000;53(4):414-420.
164. Taboas JM, Maddox RD, Krebsbach PH, Hollister SJ. Indirect solid free form fabrication of local and global porous, biomimetic and composite 3D polymer-ceramic scaffolds. Biomaterials 2003;24(1):181-194.
165. Chen VJ, Smith LA, Ma PX. Bone regeneration on computer-designed nano-fibrous scaffolds. Biomaterials 2006;27(21):3973-3979.
166. Cohen DL, Malone E, Lipson H, Bonassar LJ. Direct freeform fabrication of seeded hydrogels in arbitrary geometries. Tissue Eng 2006;12(5):1325-1335.

167. Wang X, Yan Y, Pan Y, Xiong Z, Liu H, Cheng J, et al. Generation of three-dimensional hepatocyte/gelatin structures with rapid prototyping system. Tissue Eng 2006;12(1):83-90.
168. Xu T, Jin J, Gregory C, Hickman JJ, Boland T. Inkjet printing of viable mammalian cells. Biomaterials 2005;26(1):93-99.
169. Tsang VL, Chen AA, Cho LM, Jadin KD, Sah RL, DeLong S, et al. Fabrication of 3D hepatic tissues by additive photopatterning of cellular hydrogels. FASEB J 2007;21(3):790-801.
170. Prasad T, Rengarajan R, Mittleman DM, Colvin VL. Advanced photonic crystal architectures from colloidal self-assembly techniques. Optical Mater 2005;27(7):1250-1254.
171. Wang D, Salgueiriño-Maceira V, Liz-Marzán LM, Caruso F. Gold-silica inverse opals by colloidal crystal templating. Adv Mater 2002;14(12):908-912.
172. Wang Y, Caruso F. Macroporous zeolitic membrane bioreactors. Adv Funct Mater 2004;14(10):1012-1018.
173. Reese CE, Mikhonin AV, Kamenjicki M, Tikhonov A, Asher SA. Nanogel nanosecond photonic crystal optical switching. J Am Chem Soc 2004;126(5):1493-1496.
174. Tétreault N, Míguez H, Ozin GA. Silicon inverse opal - A platform for photonic bandgap research. Adv Mater 2004;16(16):1471-1476.
175. Yan-Yan S, Dai Z, Wei G, Xing-Hua X. Nonenzymatic glucose detection by using a three-dimensionally ordered, macroporous platinum template. Chem- A European J 2005;11(7):2177-2182.
176. Schroden RC, Blanford CF, Melde BJ, Johnson BJS, Stein A. Direct synthesis of ordered macroporous silica materials functionalized with polyoxometalate clusters. Chem Mater 2001;13(3):1074-1081.
177. Sutherland RM. Cell and environment interactions in tumor microregions: the multicell spheroid model. Science 1988;240(4849):177-184.
178. Morrison SJ, Spradling AC. Stem cells and niches: Mechanisms that promote stem cell maintenance throughout life. Cell 2008;132(4):598-611.
179. Vlasov YA, Bo X-Z, Sturm JC, Norris DJ. On-chip natural assembly of silicon photonic bandgap crystals. Nature 2001;414(6861):289-293.
180. Rogach AL, Kotov NA, Koktysh DS, Ostrander JW, Ragoisha GA. Electrophoretic deposition of latex-based 3D colloidal photonic crystals: A technique for rapid production of high-quality opals. Chem Mater 2000;12(9):2721-2726.
181. Hoogenboom JP, Retif C, de Bres E, van de Boer M, van Langen-Suurling AK, Romijn J, et al. Template-induced growth of close-packed and non-close-packed colloidal crystals during solvent evaporation. Nano Lett 2004;4(2):205-208.
182. Im SH, Kim MH, Park OO. Thickness control of colloidal crystals with a substrate dipped at a tilted angle into a colloidal suspension. Chem Mater 2003;15(9):1797-1802.
183. Vickreva O, Kalinina O, Kumacheva E. Colloid crystal growth under oscillatory shear. Adv Mater 2000;12(2):110-112.
184. Sasaki M, Hane K. Ultrasonically facilitated two-dimensional crystallization of colloid particles. J Appl Phys 1996;80(9):5427-5431.
185. Jiang P, McFarland MJ. Large-scale fabrication of wafer-size colloidal crystals, macroporous polymers and nanocomposites by spin-coating. J Am Chem Soc 2004;126(42):13778-13786.
186. Zhang Y, Wang S, Eghtedari M, Motamedi M, Kotov NA. Inverted colloidal crystal hydrogel matrices as three-dimensional cell scaffolds. Adv Fun Mat 2005;15(5):725-731.
187. Luo Y, Shoichet MS. A photolabile hydrogel for guided three-dimensional cell growth and migration. Nat Mater 2004;3(4):249-253.

188. Kotov NA, Liu Y, Wang S, Cumming C, Eghtedari M, Vargas G, et al. Inverted colloidal crystals as three-dimensional cell scaffolds. Langmuir 2004;20(19):7887-7892.
189. Zinger O, Zhao G, Schwartz Z, Simpson J, Wieland M, Landolt D, et al. Differential regulation of osteoblasts by substrate microstructural features. Biomaterials 2005;26(14):1837-1847.
190. Park CH, Abramson ZR, Taba M, Jin Q, Chang J, Kreider JM, et al. Three-dimensional micro-computed tomographic imaging of alveolar bone in experimental bone loss or repair. J Periodontol 2007;78(2):273-281.
191. Stachowiak AN, Bershteyn A, Tzatzalos E, Irvine DJ. Bioactive hydrogels with an ordered cellular structure combine interconnected macroporosity and robust mechanical properties. Adv Mater 2005;17(4):399-403.
192. Sontjens SHM, Nettles DL, Carnahan MA, Setton LA, Grinstaff MW. Biodendrimer-based hydrogel scaffolds for cartilage tissue repair. Biomacromol 2006;7(1):310-316.
193. Panu K, Jarno R, Rami KK, Petro J, Juha T, Jukka SJ. Collagen network primarily controls Poisson's ratio of bovine articular cartilage in compression. J Orthopaedic Res 2006;24(4):690-699.
194. O'Brien LE, Zegers MMP, Mostov KE. Building epithelial architecture: insights from three-dimensional culture models. Nat Rev Mol Cell Biol 2002;3(7):531-537.
195. Curcio E, Salerno S, Barbieri G, De Bartolo L, Drioli E, Bader A. Mass transfer and metabolic reactions in hepatocyte spheroids cultured in rotating wall gas-permeable membrane system. Biomaterials 2007;28(36):5487-5497.
196. Minchinton AI, Tannock IF. Drug penetration in solid tumours. Nat Rev Cancer 2006;6(8):583-592.
197. Glicklis R, Merchuk JC, Cohen S. Modeling mass transfer in hepatocyte spheroids via cell viability, spheroid size, and hepatocellular functions. Biotechnol Bioeng 2004;86(6):672-680.
198. Jiang Y, Pjesivac-Grbovic J, Cantrell C, Freyer JP. A multiscale model for avascular tumor growth. Biophysical 2005;89(6):3884-3894.
199. Kelm JM, Timmins NE, Brown CJ, Fussenegger M, Nielsen LK. Method for generation of homogeneous multicellular tumor spheroids applicable to a wide variety of cell types. Biotechnol Bioeng 2003;83(2):173-180.
200. Song H, David O, Clejan S, Giordano CL, Pappas-Lebeau H, Xu L, et al. Spatial composition of prostate cancer spheroids in mixed and static cultures. Tissue Eng 2004;10(7-8):1266-1276.
201. Wu FJ, Friend JR, Hsiao CC, Zilliox MJ, Ko W-J, Cerra FB, et al. Efficient assembly of rat hepatocyte spheroids for tissue engineering applications. Biotechnol Bioeng 1996;50(4):404-415.
202. Koide N, Sakaguchi K, Koide Y, Asano K, Kawaguchi M, Matsushima H, et al. Formation of multicellular spheroids composed of adult rat hepatocytes in dishes with positively charged surfaces and under other nonadherent environments. Exp Cell Res 1990;186(2):227-235.
203. Yang J, Goto M, Ise H, Cho C-S, Akaike T. Galactosylated alginate as a scaffold for hepatocytes entrapment. Biomaterials 2002;23(2):471-479.
204. Underhill GH, Chen AA, Albrecht DR, Bhatia SN. Assessment of hepatocellular function within PEG hydrogels. Biomaterials 2007;28(2):256-270.
205. Jian L, Larisa AK, Gareth OE, Jinsheng X, Mingwen M, Wendy MP, et al. Functional three-dimensional HepG2 aggregate cultures generated from an ultrasound trap: Comparison with HepG2 spheroids. J Cellular Biochem 2007;102(5):1180-1189.
206. Wu L, Di Carlo D, Lee L. Microfluidic self-assembly of tumor spheroids for anticancer drug discovery. Biomed Microdev 2008;10(2):197-202.

207. Fukuda J, Nakazawa K. Orderly arrangement of hepatocyte spheroids on a microfabricated chip. Tissue Eng 2005;11(7-8):1254-1262.
208. Napolitano AP, Chai P, Dean DM, Morgan JR. Dynamics of the self-assembly of complex cellular aggregates on micromolded nonadhesive hydrogels. Tissue Eng 2007;13(8):2087-2094.
209. Ruei-Zhen Lin H-YC. Recent advances in three-dimensional multicellular spheroid culture for biomedical research. Biotechnol J 2008;3(9-10):1172-1184.
210. Carpenedo RL, Sargent CY, McDevitt TC. Rotary suspension culture enhances the efficiency, yield, and homogeneity of embryoid body differentiation. Stem Cells 2007;25(9):2224-2234.
211. Kunz-Schughart LA, Freyer JP, Hofstaedter F, Ebner R. The use of 3-D cultures for high-throughput screening: the multicellular spheroid model. J Biomol Screening 2004 June 1, 2004;9(4):273-285.
212. Griffith LG, Swartz MA. Capturing complex 3D tissue physiology in vitro. Nat Rev Mol Cell Biol 2006;7(3):211-224.
213. Pampaloni F, Reynaud EG, Stelzer EHK. The third dimension bridges the gap between cell culture and live tissue. Nat Rev Mol Cell Biol 2007;8(10):839-845.
214. O'Brien P, Irwin W, Diaz D, Howard-Cofield E, Krejsa C, Slaughter M, et al. High concordance of drug-induced human hepatotoxicity with in vitro cytotoxicity measured in a novel cell-based model using high content screening. Archives Toxicol 2006;80(9):580-604.
215. Gebhardt R, Hengstler JG, Muumler D, Glockner R, Buenning P, Laube B, et al. New hepatocyte in vitro systems for drug metabolism: metabolic capacity and recommendations for application in basic research and drug development, standard operation procedures. Drug Metabol Rev 2003;35(2):145 - 213.
216. Vaithilingam IS, Stroude EC, McDonald W, Maestro RF. General protease and collagenase (IV) activity in C6 astrocytoma cells, C6 spheroids and implanted C6 spheroids. J Neuro-Oncol 1991;10(3):203-212.
217. Xu J, Ma M, Purcell WM. Characterisation of some cytotoxic endpoints using rat liver and HepG2 spheroids as in vitro models and their application in hepatotoxicity studies. II. Spheroid cell spreading inhibition as a new cytotoxic marker. Toxicol Applied Pharmacol 2003;189(2):112-119.
218. James PF. Decreased mitochondrial function in quiescent cells isolated from multicellular tumor spheroids. J Cell Physiol 1998;176(1):138-149.
219. Abu-Absi SF, Friend JR, Hansen LK, Hu W-S. Structural polarity and functional bile canaliculi in rat hepatocyte spheroids. Exp Cell Res 2002;274(1):56-67.
220. Du Y, Han R, Ng S, Ni J, Sun W, Wohland T, et al. Identification and characterization of a novel prespheroid 3-dimensional hepatocyte monolayer on galactosylated substratum. Tissue Eng 2007;13(7):1455-1468.
221. Fischbach C, Kong HJ, Hsiong SX, Evangelista MB, Yuen W, Mooney DJ. Cancer cell angiogenic capability is regulated by 3D culture and integrin engagement. Proc Natl Acad Sci USA 2009;106(2):399-404.
222. Harris AL. Hypoxia - a key regulatory factor in tumour growth. Nat Rev Cancer 2002;2(1):38-47.
223. Khalil M, Shariat-Panahi A, Tootle R, Ryder T, McCloskey P, Roberts E, et al. Human hepatocyte cell lines proliferating as cohesive spheroid colonies in alginate markedly upregulate both synthetic and detoxificatory liver function. J Hepatol 2001;34(1):68-77.
224. Chang TT, Hughes-Fulford M. Monolayer and spheroid cuture of human liver hepatocellular carcinoma cell line cells demonstrate distinct global gene expression patterns and functional phenotypes. Tissue Eng A 2009;15(3):559-567.

225. Shvartsman I, Dvir T, Harel-Adar T, Cohen S. Perfusion cell seeding and cultivation induce the assembly of thick and functional hepatocellular tissue-like construct. Tissue Eng A 2009;15(4):751-760.
226. Coller HA, Sang L, Roberts JM. A new description of cellular quiescence. PLoS Biol 2006;4(3):e83.
227. Aguirre-Ghiso JA. Models, mechanisms and clinical evidence for cancer dormancy. Nat Rev Cancer 2007;7(11):834-846.
228. Sayes CM, Reed KL, Warheit DB. Assessing toxicity of fine and nanoparticles: Comparing in vitro measurements to in vivo pulmonary toxicity profiles. Toxicol Sci 2007;97(1):163-180.
229. Cho SJ, Maysinger D, Jain M, Roder B, Hackbarth S, Winnik FM. Long-term exposure to CdTe quantum dots causes functional impairments in live cells. Langmuir 2007;23(4):1974-1980.
230. Pisanic Ii TR, Blackwell JD, Shubayev VI, Fiñones RR, Jin S. Nanotoxicity of iron oxide nanoparticle internalization in growing neurons. Biomaterials 2007;28(16):2572-2581.
231. Magrez A, Kasas S, Salicio V, Pasquier N, Seo JW, Celio M, et al. Cellular toxicity of carbon-based nanomaterials. Nano Lett 2006;6(6):1121-1125.
232. Sayes CM, Fortner JD, Guo W, Lyon D, Boyd AM, Ausman KD, et al. The differential cytotoxicity of water-soluble fullerenes. Nano Lett 2004;4(10):1881-1887.
233. Zhang Y, Chen W, Zhang J, Liu J, Chen G, Pope C. In vitro and in vivo toxicity of CdTe nanoparticles. J Nanosci Nanotechnol 2007;7:497-503.
234. Sayes CM, Marchione AA, Reed KL, Warheit DB. Comparative pulmonary toxicity assessments of C60 water suspensions in rats: few differences in fullerene toxicity in vivo in contrast to in vitro profiles. Nano Lett 2007;7(8):2399-2406.
235. Liu Z, Davis C, Cai W, He L, Chen X, Dai H. Circulation and long-term fate of functionalized, biocompatible single-walled carbon nanotubes in mice probed by Raman spectroscopy. Pro Natl Acad Sci USA 2008;105(5):1410-1415.
236. Kim JS, Yoon T-J, Yu KN, Kim BG, Park SJ, Kim HW, et al. Toxicity and tissue distribution of magnetic nanoparticles in mice. Toxicol Sci 2006;89(1):338-347.
237. Oberdorster G, Oberdorster E, Oberdorster J. Nanotoxicology: An emerging discipline evolving from studies of ultrafine particles. Env Health Pers 2005;113(7):823-839.
238. Poland CA, Duffin R, Kinloch I, Maynard A, Wallace WAH, Seaton A, et al. Carbon nanotubes introduced into the abdominal cavity of mice show asbestos-like pathogenicity in a pilot study. Nat Nano 2008;3(7):423-428.
239. Hardman R. A toxicologic review of quantum dots: toxicity depends on physicochemical and environmental factors Env Health Persp 2006;114(2):165-172.
240. Colvin VL. The potential environmental impact of engineered nanomaterials. Nat Biotech 2003;21(10):1166-1170.
241. Stern ST, McNeil SE. Nanotechnology safety concerns revisited. Toxicol Sci 2008;101(1):4-21.
242. Nel A, Xia T, Madler L, Li N. Toxic potential of materials at the nanolevel. Science 2006;311(5761):622-627.
243. Lewinski N, Colvin V, Drezek R. Cytotoxicity of nanoparticles. Small 2008;4(1):26-49.
244. Jana NR, Gearheart L, Murphy CJ. Seeding growth for size control of 5-40 nm diameter gold nanoparticles. Langmuir 2001;17(22):6782-6786.
245. Talapin DV, Rogach AL, Shevchenko EV, Kornowski A, Haase M, Weller H. Dynamic distribution of growth rates within the ensembles of colloidal II-VI and III-V semiconductor nanocrystals as a factor governing their photoluminescence efficiency. J Am Chem Soc 2002;124(20):5782-5790.

246. Gaponik N, Talapin DV, Rogach AL, Hoppe K, Shevchenko EV, Kornowski A, et al. Thiol-capping of CdTe nanocrystals: An alternative to organometallic synthetic routes. J Phys Chem B 2002;106(29):7177-7185.
247. Helmlinger G, Yuan F, Dellian M, Jain RK. Interstitial pH and pO2 gradients in solid tumors in vivo: High-resolution measurements reveal a lack of correlation. Nat Med 1997;3(2):177-182.
248. Lovric J, Cho SJ, Winnik FM, Maysinger D. Unmodified cadmium telluride quantum dots induce reactive oxygen species formation leading to multiple organelle damage and cell death. Chem Biol 2005;12(11):1227-1234.
249. Derfus AM, Chan WCW, Bhatia SN. Probing the cytotoxicity of semiconductor quantum dots. Nano Lett 2004;4(1):11-18.
250. Kirchner C, Liedl T, Kudera S, Pellegrino T, MunozJavier A, Gaub HE, et al. Cytotoxicity of colloidal CdSe and CdSe/ZnS nanoparticles. Nano Lett 2005;5(2):331-338.
251. Hoshino A, Fujioka K, Oku T, Suga M, Sasaki YF, Ohta T, et al. Physicochemical properties and cellular toxicity of nanocrystal quantum dots depend on their surface modification. Nano Lett 2004;4(11):2163-2169.
252. Murphy CJ, Gole AM, Stone JW, Sisco PN, Alkilany AM, Goldsmith EC, et al. Gold Nanoparticles in biology: Beyond toxicity to cellular imaging. Accounts Chem Res 2008;41(12):1721-1730.
253. Yu P, Sabine N, Annika L, Monika F, Fei W, Ulrich S, et al. Size-dependent cytotoxicity of gold nanoparticles. Small 2007;3(11):1941-1949.
254. Schipper ML, Nakayama-Ratchford N, Davis CR, Kam NWS, Chu P, Liu Z, et al. A pilot toxicology study of single-walled carbon nanotubes in a small sample of mice. Nat Nano 2008;3(4):216-221.
255. Fischer HC, Liu L, Pang KS, Chan WC. Pharmacokinetics of nanoscale quantum dots: in vivo distribution, sequestration, and clearance in the rat. Adv Func Mate 2006;16(10):1299-1305.
256. Jain TK, Reddy MK, Morales MA, Leslie-Pelecky DL, Labhasetwar V. Biodistribution, clearance, and biocompatibility of iron oxide magnetic nanoparticles in rats. Mol Pharma 2008;5(2):316-327.
257. Choi HS, Liu W, Misra P, Tanaka E, Zimmer JP, Itty Ipe B, et al. Renal clearance of quantum dots. Nat Biotech 2007;25(10):1165-1170.
258. Walker TM, Rhodes PC, Westmoreland C. The differential cytotoxicity of methotrexate in rat hepatocyte monolayer and spheroid cultures. Toxicol in Vitro 2000;14(5):475-485.
259. Friedrich J, Seidel C, Ebner R, Kunz-Schughart LA. Spheroid-based drug screen: considerations and practical approach. Nat Protocols 2009;4(3):309-324.
260. Jan E, Byrne SJ, Cuddihy M, Davies AM, Volkov Y, Gun ko YK, et al. High-content screening as a universal tool for fingerprinting of cytotoxicity of nanoparticles. ACS Nano 2008; 2(5): 928-938.
261. Suda T, Arai F, Hirao A. Hematopoietic stem cells and their niche. Trends Immunol 2005;26(8):426-433.
262. Dellatore SM, Garcia AS, Miller WM. Mimicking stem cell niches to increase stem cell expansion. Curr Opin Biotechnol 2008;19(5):534-540.
263. Bousso P, Bhakta NR, Lewis RS, Robey E. Dynamics of thymocyte-stromal cell interactions visualized by two-photon microscopy. Science 2002;296(5574):1876-1880.
264. Calvi LM, Adams GB, Weibrecht KW, Weber JM, Olson DP, Knight MC, et al. Osteoblastic cells regulate the haematopoietic stem cell niche. Nature 2003;425(6960):841-846.
265. Lemischka IR, Moore KA. Stem cells: Interactive niches. Nature 2003;425(6960):778-779.

266. Edward AB, Melissa AD, Solomon RP, Elliot ML, Cato TL. Tissue engineered bone: Measurement of nutrient transport in three-dimensional matrices. J Biomed Mater Res A 2003;67A(1):357-367.
267. Collins SJ. The HL-60 promyelocytic leukemia cell line: proliferation, differentiation, and cellular oncogene expression. Blood 1987;70(5):1233-1244.
268. Grigoriev IV, Makhnovskii YA, Berezhkovskii AM, Zitserman VY. Kinetics of escape through a small hole. J Chem Phy 2002;116(22):9574-9577.
269. Hill TL. Effect of rotation on the diffusion-controlled rate of ligand-protein association. P Natl Acad Sci USA 1975;72(12):4918-4922.
270. Zhou H-X, Zwanzig R. A rate process with an entropy barrier. J Chem Phys 1991;94(9):6147-6152.
271. Berg HC, Purcell EM. Physics of chemoreception. Biophys J 1977;20(2):6147-6152.
272. Berezhkovskii AM, Zitserman VY, Shvartsman SY. Diffusivity in periodic arrays of spherical cavities. J Chem Phys 2003;118(15):7146-7147.
273. Berezhkovskii AM, Zitserman VY, Shvartsman SY. Effective diffusivity in periodic porous materials. J Chem Phys 2003;119(14):6991-6993.
274. Brian JS, Nathan EH. Atomic radii: Incorporation of solvation effects. J Comput Chem 1998;19(13):1482-1493.
275. Daubert TE, Danner RP. Physical and thermodynamic properties of pure chemicals. London: Taylor & Francis, 2002.
276. Larson GR. The structrue and rheology of complex fluids: Oxford University Press, 1999.
277. Tang Z, Kotov NA, Magonov S, Ozturk B. Nanostructured artificial nacre. Nat Mater 2003;2(6):413-418.
278. Thompson MT, Berg MC, Tobias IS, Rubner MF, Van Vliet KJ. Tuning compliance of nanoscale polyelectrolyte multilayers to modulate cell adhesion. Biomaterials 2005;26(34):6836-6845.
279. Wilson A, Trumpp A. Bone-marrow haematopoietic-stem-cell niches. Nat Rev Immunol 2006;6(2):93-106.
280. Kobari L, Pflumio F, Giarratana MC, Li X, Titeux M, Izac B, et al. In vitro and in vivo evidence for the long-term multilineage (myeloid, B, NK, and T) reconstitution capacity of ex vivo expanded human CD34+ cord blood cells. Exp Hematol 2000;28:1470-1480.
281. Barker J, Verfaillie C. A novel in vitro model of early human adult B lymphopoiesis that allows proliferation of pro-B cells and differentiation to mature B lymphocytes. Leukemia 2000;14:1614-1620.
282. Chen J, Brandt JS, Ellison FM, Calado RT, Young NS. Defective stromal cell function in a mouse model of infusion-induced bone marrow failure. Exp Hematol 2005;33(8):901-908.
283. Punzel M, Moore K, Lemischka I, Verfaillie C. The type of stromal feeder used in limiting dilution assays influences frequency and maintenance assessment of human long-term culture initiating cells. Leukemia 1999;13:92-97.
284. Hsiong SX, Mooney DJ. Regeneration of vascularized bone. Periodontology 2006;41(1):109-122.
285. Lutolf MP, Hubbell JA. Synthetic biomaterials as instructive extracellular microenvironments for morphogenesis in tissue engineering. Nat Biotech 2005;23(1):47-55.
286. Kiel MJ, Yilmaz ÖH, Iwashita T, Yilmaz OH, Terhorst C, Morrison SJ. SLAM family receptors distinguish hematopoietic stem and progenitor cells and reveal endothelial niches for stem cells. Cell 2005;121(7):1109-1121.
287. Kiel MJ, Morrison SJ. Uncertainty in the niches that maintain haematopoietic stem cells. Nat Rev Immunol 2008;8(4):290-301.

288. Islam A, Catovsky D, Goldman JM, Galton DAG. Histomorphological study of cellular interactions between stromal and haemopoietic stem cells in normal and leukaemic bone marrow. Histopathology 1984;8(2):293-313.
289. Poznansky MC, Evans RH, Foxall RB, Olszak IT, Piascik AH, Hartman KE, et al. Efficient generation of human T cells from a tissue-engineered thymic organoid. Nat Biotech 2000;18(7):729-734.
290. Ma K, Chan CK, Liao S, Hwang WYK, Feng Q, Ramakrishna S. Electrospun nanofiber scaffolds for rapid and rich capture of bone marrow-derived hematopoietic stem cells. Biomaterials 2008;29(13):2096-2103.
291. Liu H, Roy K. Biomimetic three-dimensional cultures significantly increase hematopoietic differentiation efficacy of embryonic stem cells. Tissue Eng 2005;11(1-2):319-330.
292. Bhandoola A, von Boehmer H, Petrie HT, Zúñiga-Pflücker JC. Commitment and developmental potential of extrathymic and intrathymic T cell precursors: plenty to choose from. Immunity 2007;26(6):678-689.
293. Petrie HT. Cell migration and the control of post-natal T-cell lymphopoiesis in the thymus. Nat Rev Immunol 2003;3(11):859-866.
294. van Ewijk W, Wang B, Hollander G, Kawamoto H, Spanopoulou E, Itoi M, et al. Thymic microenvironments, 3-D versus 2-D? Seminars in Immunol 1999;11(1):57-64.
295. Ciofani M, Zuniga-Pflucker JC. The thymus as an inductive site for T lymphopoiesis. Ann Rev Cell Develop Biol 2007;23(1):463-493.
296. Petrie HT, Zuniga-Pflucker JC. Zoned out: Functional mapping of stromal signaling microenvironments in the thymus. Ann Rev Immunol 2007;25(1):649-679.
297. Jenkinson EJ, Anderson G, Owen JJ. Studies on T cell maturation on defined thymic stromal cell populations in vitro. J Exp Med 1992;176(3):845-853.
298. Brenner M. To be or notch to be. Nat Med 2000;6(11):1210-1211.
299. Lyons AB, Parish CR. Determination of lymphocyte division by flow cytometry. J Immunol Meth 1994;171(1):131-137.
300. Janeway Jr. CA, Travers P, Walport M, Shlomchik MJ. Immuno Biology: Chapter 7 The development and survival of lymphocytes. 6th ed. New York: Garland Science Publishing, 2005.
301. Domen J, Wagers A, Weissman LI. Regenerative Medicine. Bone marrow (hematopoietic) stem cells: NIH Stem Cell Information, 2001.
302. Gao Z, Fackler MJ, Leung W, Lumkul R, Ramirez M, Theobald N, et al. Human CD34+ cell preparations contain over 100-fold greater NOD/SCID mouse engrafting capacity than do CD34- cell preparations. Exp Hematol 2001;29(7):910-921.
303. Willis F, Woll P, Theti D, Jamali H, Bacon P, Baker N, et al. Pegfilgrastim for peripheral CD34+ mobilization in patients with solid tumors. Bone Marrow Transplant 2009;43:927-934.
304. Krause DS, Theise ND, Collector MI, Henegariu O, Hwang S, Gardner R, et al. Multi-organ, multi-lineage engraftment by a single bone marrow-derived stem cell. Cell 2001;105(3):369-377.
305. Wols HAM, Underhill GH, Kansas GS, Witte PL. The role of bone marrow-derived stromal cells in the maintenance of plasma cell longevity. J Immunol 2002;169(8):4213-4221.
306. Sorrentino BP. Clinical strategies for expansion of haematopoietic stem cells. Nat Rev Immunol 2004;4(11):878-888.
307. Civin CI, Trischmann T, Kadan NS, Davis J, Noga S, Cohen K, et al. Highly purified CD34-positive cells reconstitute hematopoiesis. J Clin Oncol 1996;14(8):2224-2233.

308. Murti KG, Brown PS, Kumagai M-a, Campana D. Molecular Interactions between human B-cell progenitors and the bone marrow microenvironment. Exp Cell Res 1996;226(1):47-58.
309. Panoskaltsis N, Mantalaris A, Wu JHD. Engineering a mimicry of bone marrow tissue ex vivo. J Biosci Bioeng 2005;100(1):28-35.
310. Marshall D, Bagley J, Le P, Hogquist K, Cyr S, von Schild E, et al. T cell generation including positive and negative selection ex vivo in a three-dimensional matrix. J Hemato & Stem Cell Res 2003;12(5):565-574.
311. Varnum-Finney B, Xu L, Brashem-Stein C, Nourigat C, Flowers D, Bakkour S, et al. Pluripotent, cytokine-dependent, hematopoietic stem cells are immortalized by constitutive Notch1 signaling. Nat Med 2000;6(11):1278-1281.
312. Varnum-Finney B, Wu L, Yu M, Brashem-Stein C, Staats S, Flowers D, et al. Immobilization of Notch ligand, Delta-1, is required for induction of notch signaling. J Cell Sci 2000;113(23):4313-4318.
313. Taqvi S, Roy K. Influence of scaffold physical properties and stromal cell coculture on hematopoietic differentiation of mouse embryonic stem cells. Biomaterials 2006;27(36):6024-6031.
314. Robey E. Regulation of T cell fate by notch. Ann Rev Immunol 1999;17(1):283-295.
315. Duncan AW, Rattis FM, DiMascio LN, Congdon KL, Pazianos G, Zhao C, et al. Integration of Notch and Wnt signaling in hematopoietic stem cell maintenance. Nat Immunol 2005;6(3):314-322.
316. Zuniga-Pflucker JC. T-cell development made simple. Nat Rev Immunol 2004;4(1):67-72.
317. Schmitt TM, Zúñiga-Pflücker JC. Induction of T cell development from hematopoietic progenitor cells by Delta-like-1 in vitro. Immunity 2002;17(6):749-756.
318. La Motte-Mohs RN, Herer E, Zuniga-Pflucker JC. Induction of T-cell development from human cord blood hematopoietic stem cells by Delta-like 1 in vitro. Blood 2005; 105(4):1431-1439.
319. Varnum-Finney B, Brashem-Stein C, Bernstein ID. Combined effects of Notch signaling and cytokines induce a multiple log increase in precursors with lymphoid and myeloid reconstituting ability. Blood 2003;101(5):1784-1789.
320. Dallas MH, Varnum-Finney B, Delaney C, Kato K, Bernstein ID. Density of the Notch ligand Delta1 determines generation of B and T cell precursors from hematopoietic stem cells. J Exp Med 2005;201(9):1361-1366.
321. Dallas MH, Varnum-Finney B, Martin PJ, Bernstein ID. Enhanced T-cell reconstitution by hematopoietic progenitors expanded ex vivo using the Notch ligand Delta1. Blood 2007;109(8):3579-3587.
322. Onda M, Ariga K, Kunitake T. Activity and stability of glucose oxidase in molecular films assembled alternately with polyions. J Biosci Bioeng 1999;87:69-75.
323. Amal N, Sabine K-B, Hajare M, Bing H, Youssef H, Pierre S, et al. Cell apoptosis control using BMP4 and noggin embedded in a polyelectrolyte multilayer film. Small 2007;3(9):1577-1583.
324. Caruso F, Niikura K, Furlong DN, Okahata Y. 2. Assembly of alternating polyelectrolyte and protein multilayer films for immunosensing. Langmuir 1997;13(13):3427-3433.
325. Lidke DS, Nagy P, Heintzmann R, Arndt-Jovin DJ, Post JN, Grecco HE, et al. Quantum dot ligands provide new insights into erbB/HER receptor-mediated signal transduction. Nat Biotech 2004;22(2):198-203.
326. Fan VH, Au A, Tamama K, Littrell R, Richardson LB, Wright JW, et al. Tethered epidermal growth factor provides a survival advantage to mesenchymal stem cells. Stem Cells 2007;25(5):1241-1251.

327. Han W, Ye Q, Moore MAS. A soluble form of human delta-like-1 inhibits differentiation of hematopoietic progenitor cells. Blood 2000;95(5):1616-1625.
328. Cavasotto CN, Abagyan RA. Protein flexibility in ligand docking and virtual screening to protein kinases. J Mol Biol 2004;337(1):209-225.
329. Kimble J, Simpson P. The Lin-12/Notch signaling pathway and its regulation. Ann Rev Cell Devel Biol 1997;13(1):333-361.
330. Podsiadlo P, Michel M, Lee J, Verploegen E, Wong Shi Kam N, Ball V, et al. Exponential growth of LBL films with incorporated inorganic sheets. Nano Lett 2008;8(6):1762-1770.
331. Srivastava S, Ball V, Podsiadlo P, Lee J, Ho P, Kotov NA. Reversible loading and unloading of nanoparticles in "Exponentially" growing polyelectrolyte LBL films. J Am Chem Soc 2008;130(12):3748-3749.
332. Utada AS, Lorenceau E, Link DR, Kaplan PD, Stone HA, Weitz DA. Monodisperse double emulsions generated from a microcapillary device. Science 2005;308(5721):537-541.
333. Choi S-W, Cheong IW, Kim J-H, Xia Y. Preparation of uniform microspheres using a simple fluidic device and their crystallization into close-packed lattices. Small 2009;5(4):454-459.
334. Andrés MB-L, Richard LC, Todd CM. Engineering the embryoid body microenvironment to direct embryonic stem cell differentiation. Biotechnol Prog 2009;25(1):43-51.
335. Irvine DJ, Stachowiak AN, Hori Y. Lymphoid tissue engineering: Invoking lymphoid tissue neogenesis in immunotherapy and models of immunity. Semina Immunol 2008;20(2):137-146.
336. Ali OA, Huebsch N, Cao L, Dranoff G, Mooney DJ. Infection-mimicking materials to program dendritic cells in situ. Nat Mater 2009;8(2):151-158.
337. Steenblock ER, Wrzesinski SH, Flavell RA, Fahmy TM. Antigen presentation on artificial acellular substrates: modular systems for flexible, adaptable immunotherapy. Exp Opin Biol Ther 2009;9(4):451-464.